

ABSTRACT

Title of Document: THERMAL AND MANUFACTURING
DESIGN OF POLYMER COMPOSITE HEAT
EXCHANGERS

Juan Gabriel Cevallos, Doctor of Philosophy,
2014.

Directed By: Professor Avram Bar-Cohen
Department of Mechanical Engineering

Polymer heat exchangers, using thermally-enhanced composites, constitute a “disruptive” thermal technology that can lead to significant freshwater and energy savings. The widespread use of seawater as a coolant can be made possible by the favorable qualities of thermally-enhanced polymer composites: good corrosion resistance, higher thermal conductivities, higher strengths, low embodied energy and good manufacturability. Polymer composites can bridge the gap between unfilled polymers and corrosion-resistant metals, and can be applied to a variety of heat exchanger applications. However, thermally enhanced polymer composites behave differently from more conventional polymers during the molding process. The desired thin walled large structures are expected to pose challenges during the molding process. This dissertation presents a design methodology that integrates thermo-fluid considerations and manufacturing issues into a single design tool for thermally enhanced polymer heat exchangers. The methodology shows that the choice of

optimum designs is restricted by moldability considerations. Additionally, additive manufacturing has the potential to be a transformative manufacturing process, in which complex geometries are built layer-by-layer, which could allow for production and assembly of heat exchangers in a single step. In this dissertation, an air-to-water polymer heat exchanger was made by fused deposition modeling and tested for the first time.

This dissertation also introduces a novel heat exchanger geometry that can favorably exploit the intrinsic thermal anisotropy of filled polymers. A laboratory-scale air-to-water polymer composite heat exchanger was made by injection molding. Its performance was verified empirically, and modeled with numerical and analytical tools.

THERMAL AND MANUFACTURING DESIGN OF POLYMER COMPOSITE
HEAT EXCHANGERS

By

Juan Gabriel Cevallos

Dissertation submitted to the Faculty of the Graduate School of the
University of Maryland, College Park, in partial fulfillment
of the requirements for the degree of
Doctor of Philosophy
2014

Advisory Committee:
Professor Avram Bar-Cohen, Chair/Advisor
Professor S.K. Gupta, Co-advisor
Professor David Bigio
Professor Hugh Bruck
Professor Peter Kofinas, Dean's Representative

© Copyright by
Juan Gabriel Cevallos
2014

Dedication

A mis padres, que me lo han dado todo.

Acknowledgements

There are many people that I must acknowledge in this work. I would like to acknowledge my committee members: Prof. Bar-Cohen, Prof. Gupta, Prof. Bigio, Prof. Bruck, and Prof. Kofinas. Since my proposal, their advice and insights have guided me and kept my efforts focused. In particular I would like to thank Prof. Bar-Cohen, who in all my years in Maryland has been a great teacher, advisor, and mentor. His talks, directions, support, and occasional but much needed “slaps on the wrist” have been indispensable to making my graduate school years fruitful.

The work in this dissertation was performed as part of The Energy Education and Research Collaboration (EERC) between the University of Maryland and The Petroleum Institute. I would like to thank the Abu Dhabi National Oil Company (ADNOC) and its international partners for their generous financial support.

I also need to thank my friend Carl, and lab mates Slava, Horacio, Caleb, Alex, Jess, and Peng. Their help and distractions made it worthwhile to spend many long hours in the lab. In particular, Emil, Frank, and Mike helped me tremendously in my research work.

I must also acknowledge a few people in the ME Department to whom I am especially grateful. In particular, Amarildo DaMata and Felicia Stephenson, your help, advice, and patience were never unnoticed.

Also, I must thank Mr. Wilton Connor, whose generous financial support in my early college years opened the doors to everything I have accomplished at the University of Maryland.

Finally, I must acknowledge my family. Their support has driven me to reach nearly all goals I set to attain during my university days.

Table of Contents

Dedication.....	ii
Acknowledgements.....	iii
Table of Contents.....	v
List of Tables.....	viii
List of Figures.....	ix
1 Introduction.....	1
1.1 Current Status of Polymer Heat Exchangers.....	1
1.2 Basic Thermal Performance Considerations in Polymer Heat Exchangers..	3
1.3 History of Polymer Heat Exchangers.....	6
1.3.1 20th Century Developments.....	6
1.3.2 21st Century Developments.....	10
1.3.3 Current Commercial Applications.....	15
1.4 Motivation for use of polymers in seawater HX.....	18
1.4.1 Trends in Electricity Generation.....	19
1.4.2 Trends in Water Use.....	20
1.4.3 Electricity Generation and Water Use Nexus.....	22
1.4.4 Cooling System Effects on Power Plant.....	23
1.4.5 Role of Polymer Heat Exchangers Use.....	25
1.4.6 Embodied Energy of Polymer Heat Exchangers.....	26
1.5 Energy Education and Research Collaboration (EERC).....	30
1.6 Dissertation Goals.....	30
1.7 Approach.....	31
1.8 Dissertation Structure.....	31
2 Thermal design of polymer composite heat exchangers.....	33
2.1 Properties of polymers.....	33
2.2 Introduction to Thermally Enhanced Polymers.....	34
2.3 Gas/Liquid Heat Exchanger with Polymer Composites.....	36
2.3.1 Role of thermal conductivity.....	36
2.3.2 Case Study 1: Liquefaction of Natural Gas Using Seawater.....	39
2.3.3 Case Study 2: Water-to-Seawater Heat Exchanger.....	47
2.3.4 Case Study 3: Ocean Thermal Energy Conversion.....	50
2.4 Conclusions.....	54
3 Incorporating Moldability Considerations during the Design of PCHX.....	56
3.1 Introduction.....	56
3.2 Overview of Integrated Design Model for Polymer Heat Exchangers.....	58
3.3 Determination of Heat Transfer rate and Pumping Power.....	60
3.3.1 Heat Transfer Rate.....	60
3.3.2 Pumping Power and its Cost.....	63
3.4 Injection Molding Cost Determination.....	64
3.5 A Metamodel to Account for Moldability Considerations.....	68

3.5.1	Parametric analysis using Moldflow® to develop percent filled volume metamodel.....	68
3.5.2	Using Mold-fill Metamodel to Divide Design Space.....	72
3.5.3	Adjusting Production Cost Using Mold-fill Metamodel.....	73
3.6	Determination of Assembly Cost.....	76
3.7	Results and Discussion.....	77
3.7.1	Minimum-cost plate geometry without moldability analysis.....	78
3.7.2	Minimum-cost plate geometry with moldability analysis.....	79
3.8	Conclusions.....	84
4	Process Induced Thermal Anisotropy in Polymer Composite Fins.....	86
4.1	Fundamentals of fiber orientation in injection moldings.....	86
4.2	The Nielsen Model.....	92
4.3	Thermal conductivity calculated from orientation tensors.....	93
4.4	Numerical Prediction of 3D Fiber Orientation.....	95
4.4.1	Simulation Space and Parameters:.....	95
4.4.2	Filling Pattern.....	96
4.4.3	Fiber Orientation.....	97
4.4.4	Thermal Conductivity.....	100
4.5	Heat Transfer from Anisotropic Plate Fin.....	102
4.5.1	Gas-Liquid Polymer Heat Exchanger.....	102
4.5.2	Local Anisotropy.....	103
4.5.3	Effective Thermal Conductivity.....	107
4.6	Conclusions.....	111
5	A Novel Polymer Heat Exchanger.....	113
5.1	Webbed-Tube Heat Exchanger.....	113
5.2	Webbed-Tube Heat Exchanger Prototypes.....	115
5.2.1	Injection-molded webbed tube array.....	115
5.2.2	3D Printed webbed-tube heat exchanger.....	117
5.2.3	Overview of FDM.....	118
5.2.4	FDM Webbed-Tube Design.....	119
5.3	Heat Exchanger Test Facility.....	120
5.4	Thermal Anisotropy in Webbed-Tube Array.....	121
5.5	Thermo-fluid performance comparison to plate-fin heat exchanger.....	123
5.6	Analytical Modeling of Webbed-Tube Heat Exchanger.....	128
5.6.1	Flow in rectangular ducts.....	130
5.6.2	Heat transfer in tube bundles.....	134
5.7	Numerical simulation of webbed-tube heat exchanger.....	136
5.8	Analysis of Experimental Results and Conclusions.....	139
5.8.1	3D-Printed WTHX.....	139
5.8.2	Injection-molded WTHX.....	140
6	Conclusions.....	143
6.1	Summary and Contributions.....	143
6.1.1	Current State of the Art.....	143
6.1.2	Benefits of thermally enhanced polymer composites.....	143
6.1.3	Integrated Design Methodology.....	144
6.1.4	Process-Induced Thermal Anisotropy.....	145

6.1.5	Novel polymer composite heat exchanger	146
7	Appendices.....	147
7.1	Thermal conductivity measurement of polymer composite.....	147
7.2	Experimental validation of Moldflow filling predictions	148
7.3	Press Release.....	150
8	References.....	152

List of Tables

Table 1 Geometrical characteristics and performance limits of commercially available PHX [16].....	17
Table 2 Thermal conductivity and embodied energy of corrosion resistant materials	29
Table 3 Thermal and mechanical properties of raw polymers [3].....	34
Table 4 Thermal and mechanical properties of commercially available thermally-enhanced polymeric materials [53].....	35
Table 5 Ammonia evaporator dimensions [65]	51
Table 6 Design variables.....	59
Table 7 Effect of melt temperature and injection pressure in production cost parameters.....	75
Table 8 Assembly time estimates	77
Table 9 Summary of design variables effects.....	79
Table 9 Minimum-cost geometry for 500-kW HX (Methane: 50 m ³ /s, Seawater: 0.1 m ³ /s)	80
Table 11 Modeled Fin Geometries	96
Table 12 Summary of model discrepancy for anisotropic fins.....	110
Table 13 Accuracy of measured quantities.....	121
Table 13 Heat Exchanger Parameters.....	126
Table 15 Ansys Icepak Inputs.....	136
Table 16 Flow distribution in WTHX.....	137
Table 17 Thermal conductivity measurements using laser flash method for out-of-plane samples.....	147

List of Figures

Figure 1 Family tree of heat exchangers highlighting several types of Polymer Heat Exchangers	2
Figure 2 Flue gas cooler made by Wallstein using AlWaFlon® pressure hoses for power plant use.	15
Figure 3 Electricity generation in the United States by Source [30]	19
Figure 4 Emissions from electricity generation in the last decade [30].....	20
Figure 5 Water withdrawals in the United States by end use [34].....	22
Figure 6 Current implementation of cooling systems for thermoelectric power plants [37].....	23
Figure 7 Power output and installed cost of thermoelectric power plants based on cooling system [38].....	23
Figure 8 Water withdrawals across fuel cycles [32].....	25
Figure 9 Analytically predicted gas/liquid thermal performance in a counterflow plate-fin heat exchanger	37
Figure 10 Gas/Liquid COPT in a counterflow parallel plate heat exchanger	39
Figure 11 Methane/Seawater HX Module	40
Figure 12 Heat Transfer Rate of an LNG Train Gas Cooler Module as a Function of Thermal Conductivity	43
Figure 13 Heat Transfer per Kilogram of Heat Exchanger Mass	44
Figure 14 Overall energy expenditures of a 1MW-methane-cooler	45
Figure 15 Energy Expenditures of a 1MW Methane Cooler for a 10-year Life.....	46
Figure 16 Heat transfer rate of a water-to-seawater HX module as a function of thermal conductivity	48
Figure 17 Thermal resistances in a water-to-seawater HX module as a function of thermal conductivity	48
Figure 18 Overall energy expenditures of a 1MW water-to-seawater heat exchanger.....	49
Figure 19 Heat transfer rate of an ammonia-to-seawater hx module as a function of thermal conductivity	52
Figure 20 Overall energy expenditures of a 2MW ammonia evaporator	53
Figure 21 Seawater-methane heat exchanger module	60
Figure 22 Heat transfer rate for a counterflow HX module.....	62
Figure 23 Pumping power for a counterflow HX module	63
Figure 24 Square Finned Plate.....	65
Figure 25 Finned plate cost.....	68
Figure 26 Filled mold volume.....	72
Figure 27 Feasible boundary (mold fill % = 90).....	80
Figure 28 HX Cost along feasible boundary in scenario 1	82
Figure 29 HX Cost along feasible boundary in scenario 2	83
Figure 30 HX Cost along feasible boundary in scenario 3	84
Figure 31 Composite conductivity as a function of filler volume fraction.....	93
Figure 32 Flow front movement during filling of finned plate.....	97
Figure 33 Simulated finned plate geometry showing location of cross-section	98
Figure 34 Predicted fiber orientation tensor plots.....	100

Figure 35 Predicted thermal conductivity values along the x, y, and z directions of fin #1.....	102
Figure 36 Predicted thermal conductivity values along the x, y, and z directions of fin #2.....	102
Figure 37 Temperature profiles for anisotropic fins of various geometries high h ..	104
Figure 38 Temperature profiles for anisotropic fins of various geometries low h ...	105
Figure 39 Anisotropic fin heat loss as a function of heat transfer coefficient and fin geometry	106
Figure 40 Predicted heat transfer rate using effective thermal conductivities vs. actual anisotropic heat rate	109
Figure 41 Profile view of Webbed-Tube heat exchanger plate	114
Figure 42 3D rendition of the WTHX geometry	114
Figure 43 Drawing of aluminum mold cavity for webbed-tube array	116
Figure 44 Injection-molded webbed-tube array.....	117
Figure 45 Webbed tube heat exchanger drawing (tube length = 36.58 mm).....	117
Figure 46 Assembled Injection-Molded WTHX	117
Figure 47 ULTEM HX tested for water leaks	119
Figure 48 FDM Tool Paths	120
Figure 49 FDM WTHX made with polycarbonate	120
Figure 50 Thermocouple Locations (location marked by red dots).....	121
Figure 51 Thermal conductivity tensor components along the radius of the tube....	123
Figure 52 Sketch of both exchangers with appropriate dimensions	124
Figure 53 Heat Exchanger Pumping Power.....	126
Figure 54 Heat Exchanger Heat transfer Rate	127
Figure 55 Heat Exchanger Mass-Specific Heat Transfer Rate	128
Figure 56 Nusselt Number as a function of Reynolds Number ($Pr=0.71$, $Pr_{wall} = 0.72$ Aspect Ratio = 0.09, $L/D=9$)	135
Figure 57 Velocity Streamlines in Webbed-Tube Heat Exchanger (air flow = 4000 cc/s, inlet temperature = 120 °C)	137
Figure 58 Temperature contours across WTHX (air flow = 4000cc/s, inlet temperature = 120 °C).....	138
Figure 59 Heat transfer coefficient as a function of mass flow rate	139
Figure 60 3D Printed WTHX Performance	140
Figure 61 Experimental Heat Transfer Rate as a Function of Mass Flow Rate	141
Figure 62 Sum of squared residuals as a function of thermal conductivity.....	141
Figure 63 Thermal conductance as a function of mass flow rate	142
Figure 64 Cross sectional pictures of laser flash test specimen used to measure thermal conductivity.	147
Figure 65 Experimental verification of Moldflow filling predictions	148
Figure 66 Fabrication of a molded ABS polymer finned plate.....	149

1 Introduction

This chapter begins with a description of the current status of polymer heat exchangers, highlighting notable applications while reviewing their history. The information in this chapter is aimed to underscore the advantages and limitations of using polymers in heat exchangers. The chapter closes with the motivation for the proposed research work which includes the use of polymers, specifically polymer composites, in seawater heat exchangers for potential energy and water savings in many industrial applications.

Finally, a description of the general structure of this dissertation is included at the end of this chapter for the reader's reference.

1.1 Current Status of Polymer Heat Exchangers

Polymer heat exchangers (PHX) are needed today for many heat transfer applications. Some applications require exclusive use of polymers because of their unique physical properties: flexibility, low weight, corrosion-resistance, and ease of manufacturing. These unique properties have led to some notable commercial offerings. In the last few decades, there has been a strong push in the automotive industry to replace heavy metal parts with polymer parts in order to reduce weight and increase fuel efficiency. Although polymers, or plastics (in this dissertation the two terms are sometimes used interchangeably), are not currently used as the heat transfer surface in automotive radiators, some high-profile companies have shown interest in developing such heat exchangers (HX), as well as radiator end tanks [1]. Following Hewitt, Shires, and Botts [2], the family tree of heat exchangers in Figure 1 can be used to categorize

PHX applications by function and geometry. Note that most of the PHXs in use today are within the “Transmural HX” category, in which heat flows across a polymer wall, but cooling towers fall into the “Direct Contact” category, in which the polymers are used to create the evaporative cooling surface.

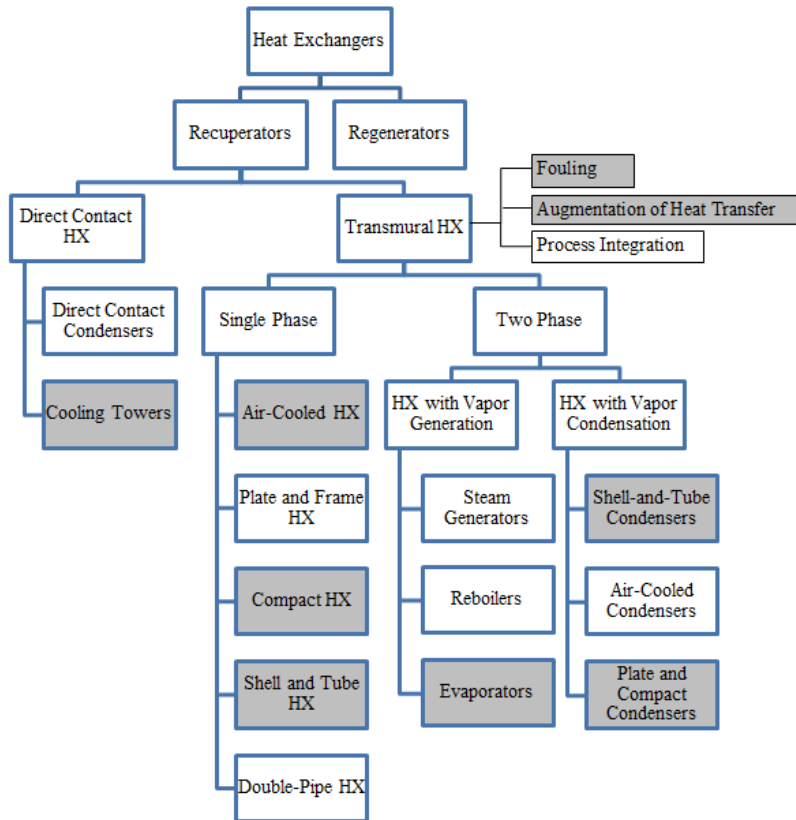


Figure 1 Family tree of heat exchangers highlighting several types of Polymer Heat Exchangers

Adapted from [2]. Shaded cells denote heat exchanger configurations in which polymers are used. Notes: Transmural refers to HXs in which heat transfer takes place through the walls separating the two streams [2]. The use of polymers in cooling towers refers to the use of plastic sheets inside the cooling tower to create more surface area.

The three cells to the right of the transmural HX box refer to three attributes that characterize all transmural HX’s: fouling prevention, heat transfer augmentation, and process integration. The use of plastic coatings to prevent corrosion fouling of metallic surfaces will not be discussed here, although significant interest has been shown in this topic [3]-[4], and coated tubes are available commercially. This section is focused on applications in which polymers are used as the main heat transfer

surface. The use of polymers to minimize HX fouling in a heat exchanger has also been reported in the form of plastic twisted tapes used to remove the fouling on the internal surface of tubes [5]. Such tapes rotate using part of the energy of the flowing fluid, and strike and scrape fouling material that has adhered to the surface of the tube. Plastic inserts are used to enhance heat transfer by increasing the wetted area and changing the fluid velocity profile to enhance convection [6]. The majority of the work outlined here focuses on trans mural HXs, both single-phase and two-phase. In the following sections, many heat exchangers which fall in these two categories will be identified. Few or no regenerators fabricated entirely with polymers are in use today. Despite the limited use of PHXs, there is a remarkable amount of research aimed at developing many of the different types of PHX listed in Figure 1, as discussed in this chapter. Actual applications of PHXs in industry will be discussed in detail, where appropriate.

1.2 Basic Thermal Performance Considerations in Polymer Heat Exchangers

Before examining the evolution of plastic heat exchangers, it is important to revisit an important metric of HX thermal performance: the overall thermal conductance, UA . This metric serves to evaluate the heat exchanger performance as a function of the convective coefficients and wall thermal conductivity [7]. Examining the heat exchanger heat transfer paths, it is possible to identify five thermal resistances in series: (1) hot-fluid-side convection resistance, (2) hot-fluid-side fouling resistance, (3) wall thermal resistance, (4) cold-fluid-side fouling resistance, and (5) cold-fluid-side convection resistance. The overall thermal resistance can be obtained by simply

summing all these resistances, as shown in Equation 1, and more explicitly in Equation 2.

$$R_o = R_h + R_{h,f} + R_w + R_{c,f} + R_c \quad (1.1)$$

$$R_o = \frac{1}{(\eta_o h A)_h} + \frac{1}{(\eta_o h_f A)_h} + R_w + \frac{1}{(\eta_o h_f A)_c} + \frac{1}{(\eta_o h A)_c} \quad (1.2)$$

The wall thermal resistance can be defined as:

$$R_w = \begin{cases} \frac{\delta_w}{k_w A_w}, & \text{for a flat wall} \\ \frac{\ln(d_o/d_i)}{2\pi k_w L}, & \text{for a circular tube} \end{cases} \quad (1.3)$$

Finally, the overall thermal conductance of a HX, UA , is simply the inverse of its overall thermal resistance, R_o :

$$UA = \frac{1}{\frac{1}{(\eta_o h A)_h} + \frac{1}{(\eta_o h_f A)_h} + R_w + \frac{1}{(\eta_o h_f A)_c} + \frac{1}{(\eta_o h A)_c}} \quad (1.4)$$

The overall heat transfer coefficient, U , can be defined by dividing the UA by a reference area defined as A , hence the product UA . The heat transfer rate can be expressed in terms of the UA , as:

$$q = UA \cdot \text{LMTD} \quad (1.5)$$

where the log-mean temperature difference (LMTD) is the logarithmic average of the temperature difference between the two streams, and depends on the configuration of the exchanger.

Examining Equations 3 and 4, it may be seen that any reduction in the individual thermal resistances will result in an improvement in the thermal conductance, UA . A high wall thermal conductivity k_w reduces the wall resistance. Meanwhile, the convective resistances, which depend on fluids thermo-physical properties (sometimes restricted by the application) can be reduced by increasing the heat transfer coefficients h , which is most commonly achieved by increasing the fluid velocity (there are many more methods to increase h). The fouling coefficients h_f usually depend on the surface material and the fluid properties. A high h_f value implies that there is a low propensity for fouling to occur. Note that all thermal resistances can be reduced by increasing their corresponding surface area, subject to surface efficiencies if extended surfaces are used.

The thermal conductance UA alone does not provide an assessment of factors affecting the cost of a HX such as pumping power consumption, and material and space usage. However, the overall heat transfer capability can be quantified using UA and provide the means for evaluating the effect of thermal conductivity on the thermal performance of polymer HX's. Note that polymers generally have a significantly lower thermal conductivity than most metals, and the wall resistance R_w can, thus, be expected to be relatively high. However, in certain applications where the wall thickness is small and the heat transfer coefficient of at least one of the fluids is relatively low, the wall resistance can be smaller than the convective resistance.

This is the case, in fact, for many gas/liquid and gas/gas exchangers, in which the gas side convective resistance has a dominant role in the UA .

1.3 History of Polymer Heat Exchangers

1.3.1 20th Century Developments

Over 40 years ago, engineers at DuPont were the first to successfully design and manufacture plastic heat exchangers [8]. Prior to this, others had been unable to overcome the difficulties associated with the use of plastics, including very low thermal conductivity compared to metals, reduced strength at higher temperatures, and the absence of an established manufacturing process. The DuPont PHX design, installed in over 40 sites, mainly within DuPont, consisted of many small-diameter, thin-walled polytetrafluoroethylene (PTFE or Teflon), tubes bundled and joined at each end to form a rigid honeycomb structure. This structure eliminated the need for conventional tube sheets in these exchangers. Considering PTFE's resistance to corrosion, scaling, and fouling, the applications included cooling of acids (e.g. sulfuric acid, nitric acid), heating of chemicals (e.g. chloride solution, phosphatizing bath, metasilicate), partial condensing (solvent-air), evaporative air-water cooling, water/water heating, to mention just a few. Experiments were performed to verify the anti-scaling and anti-fouling characteristics of PTFE. Scaling tests revealed that calcium carbonate and calcium sulfate scaling (two common foulants) on PTFE tubes is much less problematic than on nickel tubes due to PTFE's low surface energy.

The corrosion resistance of PTFE is quite unique because its composition is fully fluorinated. Since fluorine is the most electronegative of the halogens, it forms strong bonds with carbon atoms, which ultimately results in high chemical resistance and a

wide range of corrosion resistance [3]. In fact, only the most potent oxidizing and reducing agents will attack PTFE. For example, fluorine itself is absorbed by PTFE, and the resulting mixture is sensitive to ignition. Alkali metals also attack PTFE by removing fluorine from the polymer molecule [3].

To help overcome the effects of low thermal conductivity, DuPont's PHX tube wall thickness was kept to 5%-15% of the tube diameter, and HX surface area per unit volume was increased from $130 \text{ m}^2/\text{m}^3$ -for a typical metal heat exchanger- to $650 \text{ m}^2/\text{m}^3$. This increase in surface area was made possible by the added number of small tubes bundled together. The tube bundles could have as few as 60 tubes and as many as 5,000 tubes, with outer diameters ranging from 2 mm to 6 mm. The overall heat transfer coefficient depended on the application and ranged from $34 \text{ W}/\text{m}^2\text{K}$, for an air/gas exchanger, to $560 \text{ W}/\text{m}^2\text{K}$ for water/water exchangers, with the wall thermal resistance dominating the overall resistance when the convective heat transfer coefficients were high. Due to the low HX material thermal conductivity, the overall heat transfer coefficient could only be as high as $840 \text{ W}/\text{m}^2\text{K}$ for the thinnest tube walls (0.2 mm). The relatively high thermal resistance posed by the low conductivity tube wall will be a reoccurring theme in this dissertation.

In the late 1960's and early 1970's in Australia, Pescod [9]-[12] conducted experiments to measure the thermal performance of enhanced plate heat exchangers for air conditioning applications. The HX was made of thin plastic sheets that were vacuum-formed with surface enhancements. The enhancements were either regular protuberances or corrugations that promoted turbulence in the flow to increase the heat transfer coefficient relative to plane parallel plates. The plates were thin enough

to make the plastic wall thermal resistance negligible because of the high convective resistances in this air-to-air heat exchanger. Initial experiments were performed with polystyrene (PS) sheets approximately 200 mm square and 0.25 mm thick, but in later exchangers the plates were made of polyvinyl chloride (PVC) instead, and their thickness was reduced to 0.2 mm. Experimental results showed that heat transfer coefficients were higher for the enhanced plates than for bare plates with only slightly higher friction factors.

The plates were assembled in a cross-flow configuration and were heat sealed or electrically welded at the edges to prevent any fluid leakage. The protuberances in the sheets also served as physical support between plates, and when plates only had corrugations, protrusions were added to facilitate assembly. The HXs had a maximum operating temperature limit of about 50 °C, above which the plate would experience some distortion. The technology was licensed by Dricon Air Pty. Ltd. and manufactured for various air conditioning applications.

Owing to the success of DuPont's PTFE heat exchangers, and increasing energy costs, in the 1970's the U.S. Department of Energy commissioned Argonne National Laboratory (ANL) to review the state-of-the-art in plastic heat exchangers, focusing on low temperature heat recovery applications [13]. Thirteen years after their introduction, DuPont's tube exchangers had been adopted for many industrial applications, such as pickling in steel manufacturing, heating of agitated reactor vessels, and heating/cooling of distilled water, which provided evidence of the value of plastic heat exchangers. The ANL review identified candidate materials for further study based on several selection criteria: strength, known properties and fabrication

techniques, compatibility with proposed applications, and commercial availability.

Three plastics were selected as the most promising candidates:

polytetrafluoroethylene (PTFE-Teflon), polyphenylene sulfide (PPS), and polyvinylidene fluoride (PVDF). However, material properties were found to be very sensitive to the fabrication process (and post-fabrication treatment). The review also listed additives and treatments for enhancing the mechanical and thermal properties of polymer resins, as well as possible low-cost fabrication techniques. Finally, some areas of activity were recommended for future research and development, including development of techniques for producing composites, identifying applications of low temperature heat recovery, and improving existing – or developing new - fabrication techniques for polymer composite HX components. All these challenges were partly addressed in the years following the publication of the review.

Today, DuPont no longer manufactures PTFE heat exchangers. However, they continue to provide fluoropolymer resins to companies such as Ametek, which manufactures and sells heat exchangers using DuPont's resins, for applications in highly corrosive environments.

In 1989, a review paper by Reay [14] examined available materials, HX configurations, and expected trends in polymers. Several thermoplastic resins were highlighted because of their corrosion resistance or high operating temperature. It was reported that polyphenylene sulfide (PPS), for example, had outstanding performance in corrosion tests with 85% sulfuric acid at 120 °C for up to 5,000 hours, but that polyvinylidene fluoride (PVDF) showed some corrosion. Polyetheretherketone (PEEK) reportedly survived a continuous operating temperature of 250 °C, and

retained its mechanical properties at over 300 °C. PEEK was also found to offer high resistance to chemical attack except from concentrated nitric and sulfuric acids.

1.3.2 21st Century Developments

The present decade has seen considerable expansion of the above efforts to develop PHX technology. In 2001, a two-year consortium project funded by the European Union was completed, which reviewed technologies for both polymer forming and modular heat exchanger assembly [15]. The goal was to develop a prototype polymer heat exchanger evaporator, as a replacement for metallic evaporators, which could operate at over 100°C in corrosive and fouling environments, with competitive capital and maintenance costs. A laboratory-scale prototype heat exchanger was built and tested. Made with 120 welded perfluoroalkoxy (PFA) tubes, the prototype had a surface area of 8.4 m², and was capable of producing 40 kg/h of water vapor. Results of the tests performed are not available in the published report, but it was reported that an industrial pilot was built and tested under corrosive environments. PFA is a fully fluorinated thermoplastic with good corrosion resistance, but it is not as strong as PTFE at elevated temperatures. Like PTFE, PFA is not subject to UV degradation. It is used in many applications in the chemical process industry, generally as lining for pipes and vessels [3].

Compact HXs, particularly a new design of a polymer film compact heat exchanger (PFCHX), were reviewed in detail by Zaheed and Jachuck in 2004 [16]. The PFCHX design consists of a plate heat exchanger made of 100 µm-thick PEEK films that are then corrugated and stacked into a cross-flow configuration. The thin polymer films were used to decrease the wall thermal resistance, hence increasing the overall heat

transfer coefficient. It was also found that at this film thickness, PEEK maintains its mechanical strength, thereby sustaining a differential pressure of 1,000 kPa, at 25°C. In fact, PEEK has tensile properties that exceed most thermoplastics, and has excellent creep properties. This and other properties make it a great choice for bearing applications, in which the material must withstand a high load for an extended period of time at a high temperature [3]. Calculations showed that this liquid-liquid PFCHX could provide significant weight savings, while yielding heat duties similar to those of metallic heat exchangers.

Work at the Solar Energy Laboratory at the University of Minnesota [17]-[21] focused on the use of polymers in solar hot water systems. The low density (weight) and low cost of polymers were the main factors motivating this research. Raman et al. [18] reviewed polymer materials suitable for solar hot water systems, i.e. compatible with water or propylene glycol, as well as capable of withstanding 82 °C and 1.1 MPa of internal pressure. Initial candidate materials were selected based on the National Sanitary Foundation (NSF) certification for use with potable water, compatibility with water and glycol, heat distortion temperature, thermal index (i.e. maximum service temperature at which the polymer tensile strength degrades to half of its original value in 50,000 hrs), glass transition temperature, and water absorption. To refine material selection, a figure-of-merit for the wall was specified, thermal conductance per dollar per unit area. With this figure of merit a material is selected based on its thermal conductivity, tensile strength, and cost. To quantify this figure-of-merit, the thermal conductance per unit surface area of the polymer material K

(W/m²K) is the ratio of the thermal conductivity k to the minimum wall thickness t_{\min} required to withstand the operating pressure (1.1 MPa):

$$K = \frac{k}{t_{\min}} \quad (1.6)$$

K is then divided by the material cost of a unit surface area C_A (\$/m², based on costs in 2000). The resulting metric K/C_A (W/K·\$) is a measure that combines heat transfer capabilities, strength and cost. Using this figure of merit to compare candidate materials, it was determined that nylon (PA, 7600 W/K·\$), polypropylene (PP, 3300 W/K·\$), and cross-linked polyethylene (PEX, 3200 W/K·\$) were best suited for thin-walled tubing. It is to be noted that polyphenylene oxide (PPO) was found to offer a figure-of-merit value of 5100 W/K·\$, but was ruled out due to unavailability of commercial tubing. Other materials, including PTFE and PVDF, had very low figures of merit (<500 W/K·\$) due to their very high material costs.

The work of Alizadeh [22] expanded the use of polymer heat exchangers to solar liquid desiccant air conditioning (LDAC). The system featured a polymer plate HX used both for dehumidification and indirect evaporative cooling. The exchanger, developed by Ficom Pty. Ltd. in South Australia, consisted of 0.2 mm- thick sheets of polymer with dimples to serve as spacers and keep the plates separated. The sheets' thickness was minimized to reduce the conductive resistance and increase the thermal effectiveness of the heat exchanger. The exchanger had a cross-flow configuration in which the air stream is indirectly cooled by a secondary air stream (return), and dehumidified by a liquid desiccant sprayed into the air stream.

In the late 1990's, Magneti Marelli Climatizzazione SpA and DuPont [23] jointly developed plastic heat exchangers suitable for automotive use. A charge air cooler (CAC) was seen initially as the most promising application. Since this is an air-to-air heat exchanger with high convective thermal resistances, the low thermal conductivity of DuPont PA-based material (Caltrel) used to build the prototype was not a performance limitation. Unlike the conventional metal heat exchanger with louvered fins, additional surface area in the prototype CAC was created by using many thin, closely-spaced tubes. The tubes had a diameter of 3 mm and the tube pitch was 4.1 mm. On the other hand, the metal CAC had a tube pitch of 15 mm. The increased number of tubes decreased the cooling air side free flow area and increased the pressure drop. Thermal performance was, in fact, better for the polymer CAC because the less-efficient area provided by the fins was replaced by primary surface area of the thin tubes. The overall heat transfer coefficient in the plastic CAC ranged from 10 to 18 W/m²K for a range of cooling air mass flow from 0.1 to 0.4 kg/s, and – on average – 15% higher than the metal CAC. For the stated mass flow, the pressure drop ranged from 100 to 1100 Pa, on average 28% higher than the metal CAC. Despite these modest differences in performance and pressure drop, field tests of a vehicle equipped with a polymer HX, failed to reveal any differences in the performance of the vehicle associated with the use of the polymer heat exchanger. Recalling DuPont's first polymer heat exchangers, PTFE is still a prominent heat transfer surface material. In Belchatów, Poland, a new 858-MW generating unit was built at Europe's largest lignite-fired power plant [24]. For this unit, Wallstein of Recklinghausen, Germany commissioned two flue gas coolers (Figure 2), with the

recovered energy being used to preheat the combustion air. The coolers use as tubes approximately 500,000 meters of AlWaFlon® pressure hose, which was developed jointly by Wallstein, DuPont, and Fluortubing (Utrecht, Netherlands). The base resin for these hoses is DuPont's PTFE, and the resulting pressure hoses are said to have an upper service temperature of 260 °C. The hoses were tested for internal pressure-induced creep rupture, and the new resin out-performed other polymers with similar corrosion resistance. For example, at 175 °C a 12 mm diameter AlWaFlon pipe could withstand about 5 MPa of hoop stress for 10,000 hours, while a Perfluoroalkoxy (PFA) pipe could only withstand approximately 4.5 MPa, and a standard PTFE pipe only approximately 3.5 MPa [24].

Each of the coolers developed by Wallstein nominally transfers 32 MW and reduces gas temperature by 50 °C. As the gas cools, several contaminants condense on the hose surface, including sulfur dioxide (SO₂), sulfur trioxide (SO₃), hydrogen fluoride (HF), and hydrochloric acid (HCl) [24]. These pollutants combine with the moisture content to form corrosive acid mixtures. However, the fluoropolymer is chemically-inert and can resist corrosion from these acids. Another HX made with AlWaFlon tubing will be installed in Vattenfall's new CHP (combined heat and power) plant in Siekierki, Poland [25]. It will cool about 2 million m³/h of flue gas from 185 °C to 127 °C, with a total heat transfer rate of approximately 55.5 MW).



Figure 2 Flue gas cooler made by Wallstein using AIWaFlon® pressure hoses for power plant use.
Courtesy of DuPont [24].

Chen et al. [26] presented an experimental investigation of the thermal performance of three finned-tube heat exchangers. The finned-tubes were successfully manufactured from fiber-filled polypropylene composites with thermal conductivities of 2.3 and 16.5 W/m·K. For comparison purposes, a heat exchanger with un-reinforced polypropylene (0.2 W/m·K) was also fabricated and tested. Their experiments with air/water cross-flow confirmed predictions that the wall thermal resistance is only dominant when the thermal conductivity is extremely low, as is the case for un-reinforced polypropylene. For the case of composites, the high convective resistance of the air-side dominates the thermal conductance, UA.

1.3.3 Current Commercial Applications

Table 1 compiles a representative sample of commercially-available plate, immersion coil, and shell-and-tube PHXs, including dimensions and operating limits. This summary is derived from commercial HX data (offered by vendors cited in Zaheed and Jachuck [16], who reviewed the availability and application of polymer heat

exchangers). The data in Table 1 show that maximum operating pressures and temperatures are generally less than 700 kPa and 150°C, respectively. These relatively low upper-bound operating parameters reflect the low strength and glass transition temperatures of the candidate polymer heat exchanger materials considered. Other popular commercial products are Renewaïre’s energy recovery ventilation products, which use Mitsubishi’s Lossnay core. The Lossnay core is a cross flow, air-to-air plate-fin heat exchanger made of a specially processed paper. The permeability of the “composite resin” plate allows the HX to transfer both heat and moisture from one air stream to the other [27].

Table 1 Geometrical characteristics and performance limits of commercially available PHX [16]

Manufacturer	HX Type	Application	Dimensions	Materials	Performance
Greenbox Co. www.greenbox.uk.com	Plate	Can handle airflows with sensible and latent heat exchange	Walls are less than 0.5 mm	PVC	Temp. -15°C to 60°C. Max. pressure 1 kPa
George Fischer www.us.piping.georgefischer.com	Plate, coils, shell and tube	Heat transfer between corrosive fluids		PVDF and PP	
Plastic Magen www.plasticmagen.com	Plate	Solar collectors for heating swimming pools	Rectangular cavity transversed by 5 mm OD, 5 mm wall tubes	PVDF and PP	PVDF can withstand 600 kPa at 100°C. PE 200 kPa at 80°C
AB Segerfrojd www.segerfrojd.com	Plate	Ventilation, humidifying, electronic cooling, wet flue gas recuperation	Sheet thickness from 2 to 5 mm	Extruded PP sheets	Temp. -40 to 90 °C. Compressive strength 188 kPa at 2.88 mm
Ail Research, Inc www.ailr.com	Plate	Corrosive liquid cooling	Plates are made from a 5 mil (0.127 mm) film	Thermofomed plastic	Temp. of up to 148°C. Pressure up to 275 kPa
Process Technology www.process-technology.com	Shell-and-tube, coils	Immersion heat exchanger	0.76 mm thick wall	Shell: PP of PVDF. Tube: PFA.	Max.pres./temp Tube: 241 kPa at 120 °C. Shell 206 kPa at 100 °C
Fluorotherm www.fluorotherm.com	Shell and Tube	Semiconductor and biotechnology (ultrapure), environmental, laboratory and products finishing industries		Shell are PVC and CPVC. Tubing are PTFE, FEP and PFA	Max. temp for shell 60 – 93 °C. Working pressure are 276 kPa at 60 °C and 172 kPa at 100 °C
Cesaroni Technology Incorporated www.cesaronitech.com	Plate	Chiller applications	(28 x 42 x 7.6 cm)	Polyamide	Operating Pressure: up to 550 kPa. Temperature Range: -40 to 115°C

In this section, a selection of important developments has been highlighted to illustrate the advantages and limitations of polymer heat exchangers. A more complete overview was published in the journal Heat Transfer Engineering [28]. The next section discusses the motivation for the use of polymer composites in heat exchangers; specifically, seawater heat exchangers.

1.4 Motivation for use of polymers in seawater HX

Polymer heat exchangers (PHXs), using thermally-enhanced composites, constitute a “disruptive” thermal technology that can lead to significant water and energy savings in the thermoelectric energy sector. This section reviews current trends in electricity generation, water use, and the inextricable relationship between the two trends in order to identify the possible role of PHXs in seawater cooling applications. The use of once-through seawater cooling as a replacement for freshwater recirculating systems is identified as a viable way to reduce the use of freshwater and to increase power plant efficiency. The widespread use of seawater as a coolant can be made possible by the favorable qualities of thermally-enhanced polymer composites: good corrosion resistance, higher thermal conductivities, higher strengths, low embodied energy and good manufacturability. Also, a seawater cooling case study is used in Chapter 2 to explore the potential water and energy savings made possible by the use of PHX technology. The results from said study suggest that heat exchangers made with thermally enhanced polymer composites require less energy input over their lifetime than corrosion resistant metals, which generally have much higher embodied energy than polymers and polymers composites. Also, the use of seawater can significantly reduce the use of freshwater as a coolant, given the inordinate amounts of water required for even a 1MW heat exchanger.

The material presented in section 1.4 and its subsections was originally presented at the International Mechanical Engineering Congress & Exposition in 2011 [29].

1.4.1 Trends in Electricity Generation

Electricity generation in the United States has increased dramatically from 3037 TWh in 1990 to 3950 TWh in 2009, an average increase of 1.6% annually [30]. The overwhelming majority of electricity generated came from thermoelectric, fossil fuel – primarily coal and natural gas – power plants, which accounted for more than 70% of the generated power during this period, as shown in Figure 3.

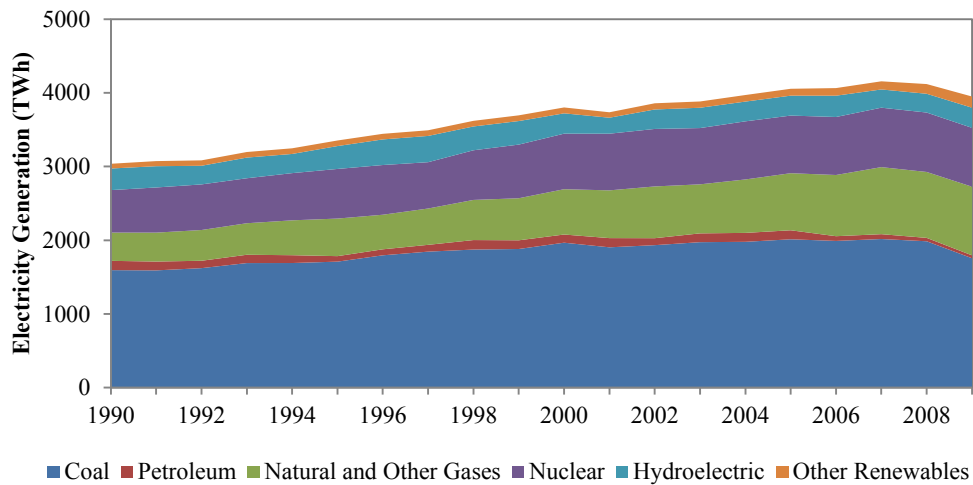


Figure 3 Electricity generation in the United States by Source [30]

The trends from Figure 3 also show the recent decline in electricity generation at coal power plants (a decrease of 11.6% from 2008 to 2009, thus accounting for 44.5% of total generation in 2009) and increase in generation at natural gas power plants (an increase of 4.3% from 2008 to 2009, thus accounting for 23.3% of total generation in 2009). These trends reflect the increase in delivered coal prices and the decrease in delivered natural gas prices, as well as the cost of compliance with current environmental regulations [30]. Renewables, other than hydroelectric power, increased 19.8% in 2008 and 14.4% in 2009, enhancing the contribution of this sector that has increased 87.2% since 1998. These trends in generation as well as the installation of new emission control devices have led to decreased emissions from

electricity generating facilities, as shown in Figure 4. Although total generation increased 9.1% from 1998 to 2009, carbon dioxide emissions from electricity generation were reduced by 3.5%, sulfur dioxide emissions were reduced 55.7% and nitrogen oxides emissions were reduced 62.9%.

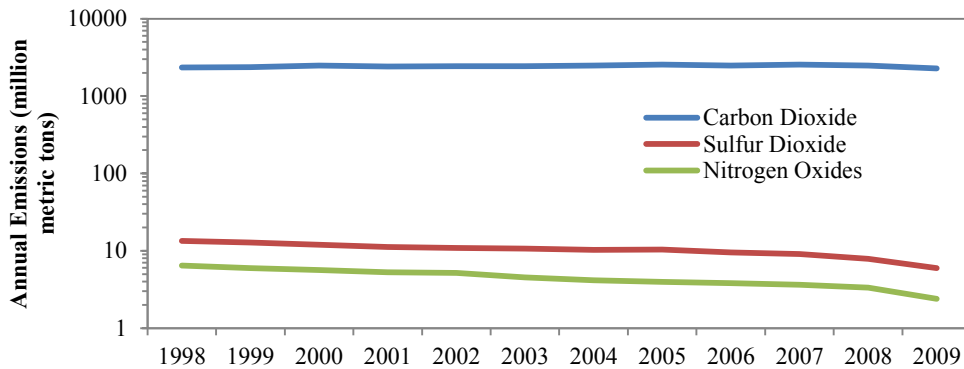


Figure 4 Emissions from electricity generation in the last decade [30]

It is expected that electricity generation will continue to grow and projections to 2035 are available. Based on Energy Information Administration estimates, electricity generation including net imports is expected to grow from 4015 TWh in 2009 to 4286 TWh in 2015 to 4704 TWh in 2025 to 5181 TWh in 2035 [31]. This growth will generate new challenges as the U.S. attempts to meet increasing demand while reducing greenhouse gas emissions and supplying freshwater for irrigation and domestic uses.

1.4.2 Trends in Water Use

Current trends in water use show that demands on the United States' water supply are growing, while storage capacity of surface water is becoming more limited and ground water is being depleted [32]. Water supply issues are exacerbated by strong population growth in water-scarce areas, such as in Nevada and Arizona, where populations increased by 32.3% and 28.6%, respectively, between April 2000 and

July 2009 [33]. Figure 5 shows water withdrawals in the United States by end use, revealing that withdrawals for cooling of thermoelectric power plants accounted for 49% of all withdrawals in 2005 [34]. Although withdrawals were greatest for the thermoelectric cooling sector, consumption of this sector was less than 3% of total consumption, which was dominated by irrigation and public supply end uses [34]. Note that according to the United States Geological Survey, withdrawal is defined as water removed from the ground or diverted from a surface-water source for use, while consumption is defined as the part of water withdrawn that is evaporated, transpired, incorporated into products or crops, consumed by humans or livestock, or otherwise removed from the immediate water environment [34]. It must be noted, however, that water withdrawn for power plant cooling cannot directly re-enter the domestic water supply and must be actively treated or allowed to re-enter the natural water cycle before becoming available for irrigation and or domestic use.

Current withdrawals for cooling of thermoelectric power plants include modest use of saline water. Surface water was the source for 99% of total withdrawals for thermoelectric cooling and 28% of the surface water withdrawals were saline [34].

Saline surface water withdrawals for thermoelectric power accounted for 93% of total saline withdrawals for all categories [34], which demonstrates that thermoelectric cooling is one of the few end uses that can operate while using saline water.

However, recent history suggests that the thermoelectric power industry is not focusing on the use of saline water. Between 2000 and 2005, total withdrawals for thermoelectric cooling increased by 3%, of which freshwater withdrawals increased 7%, whereas saline withdrawals decreased 4% [34]. It is evident that thermoelectric

cooling is a significant market for the use of saline water, although this resource is not being fully utilized because of the difficulties associated with the use of saline water (e.g., environmental impact concerns, corrosion).

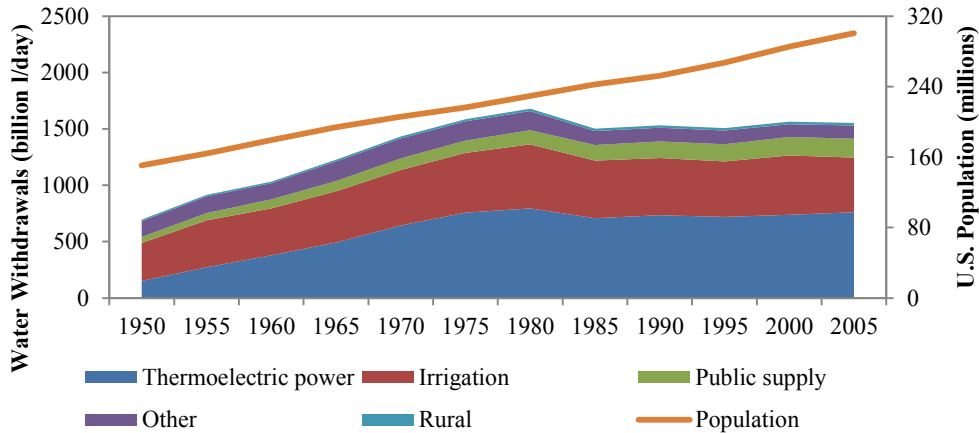


Figure 5 Water withdrawals in the United States by end use [34]

1.4.3 Electricity Generation and Water Use Nexus

The relationship between electricity generation and water use is largely the result of the need for cooling water for condensing steam in thermoelectric power plants. Thermoelectric power plants rely on the heat generated by combustion of a fuel resource (e.g., fossil or biomass) to evaporate water at high temperature and high pressure, after which the steam expands through a turbine connected to a generator to produce electricity. After leaving the turbine, the low-pressure steam must be condensed before returning to the evaporator and thus, cooling water is fed through a condenser to remove heat from the steam. Cooling water mass flow rates can be 50 times or more as high as steam mass flow rates depending on the allowable temperature rise of the cooling water, which is typically 8-14°C [35]. Figure 6 shows the breakdown of currently installed cooling systems on thermoelectric power plants in the United States.

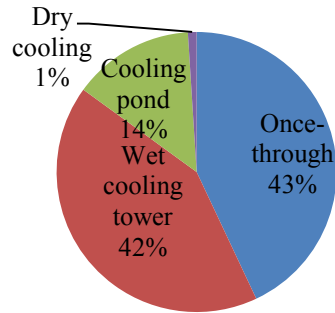


Figure 6 Current implementation of cooling systems for thermoelectric power plants [37]

1.4.4 Cooling System Effects on Power Plant

The relative power output and installed cost of thermoelectric power plants are dependent on the selected cooling method, as shown in Figure 7. Once-through systems have the highest power output and lowest installed cost because they have the lowest heat sink temperature and most compact cooling solution [38]. Dry cooling systems have lower efficiency than wet cooling towers or once-through systems because of parasitic losses from operation of the cooling system (i.e., fan blowing) [39]. Dry systems are expensive because they require larger structures to dissipate the heat because of the poor performance of air as a heat transfer fluid.

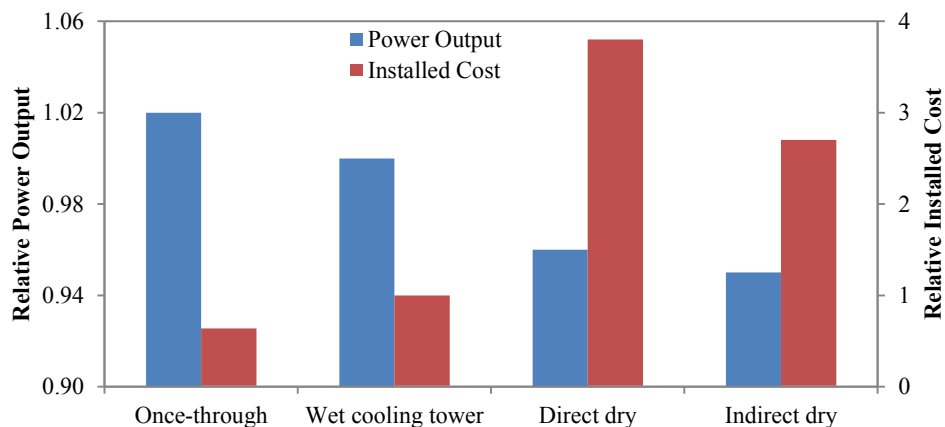


Figure 7 Power output and installed cost of thermoelectric power plants based on cooling system [38]

Cooling method selection has important implications on the life-cycle water use of the power plant. Fthenakis and Kim [32] studied the life cycle water withdrawals for

various fuel cycles, incorporating withdrawals for extraction and processing of fuels and manufacturing. Their results, shown in Figure 8, reveal that recirculating and cooling ponds generally require less withdrawals than once-through systems and that high efficiency cycles, such as those for natural gas combined cycles, reduce water use. It is noteworthy that water withdrawals for biomass power plants vary widely based on the irrigation requirements of the crops, which is a function of growth location. Other renewable sources, such as photovoltaics and wind, demonstrate multiple benefits by reducing emissions and reducing water withdrawals for electricity generation. Fthenakis and Kim considered only withdrawals because there is minimal information on upstream consumptive water usages [32]. Nonetheless, their results demonstrate the importance of both selecting a generation source and the cooling method for that source.

It is anticipated that water withdrawals will increase in the future for fossil fuel fed thermoelectric power plants due to carbon sequestration practices. A report from the National Energy Technology Program estimated that carbon capture based on monoethanolamine scrubbing to remove carbon dioxide would increase water withdrawals by 90% in subcritical pulverized coal power plants, 87% in supercritical pulverized coal power plants, 45% in integrated gasification combined cycle power plants and 79% in natural gas combined cycle power plants [37].

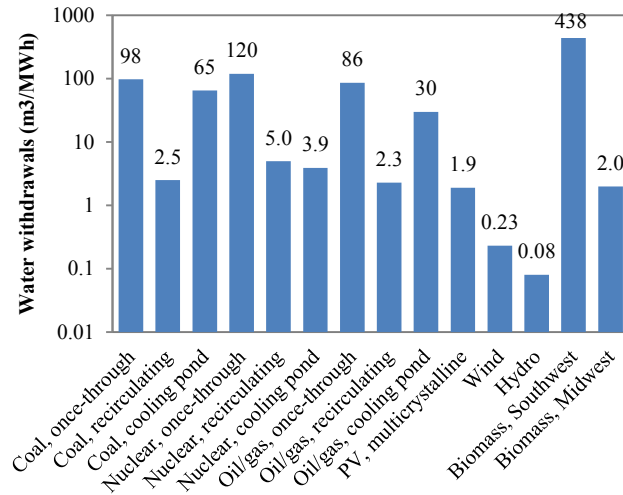


Figure 8 Water withdrawals across fuel cycles [32]

1.4.5 Role of Polymer Heat Exchangers Use

Polymer heat exchangers (PHXs) can play an important role in the future of energy-water issues. In a world confronting the twin challenges of supplying sufficient electricity and water to support a growing standard of living for the world's population, the use of PHXs for seawater cooling of thermoelectric power plants could alleviate this industry's voracious appetite for freshwater, freeing resources for irrigation and domestic consumption, as well as increasing power plant efficiency. Polymer composites offer corrosion resistance, higher thermal conductivities, higher strengths, low embodied energy and manufacturability that will allow for the fabrication of inexpensive, low embodied energy heat exchangers for corrosive environments. Heat exchangers that can operate in corrosive environments are also useful for geothermal and ocean thermal power generation, desalination, chemical processing and waste heat recovery. While freshwater supplies are considered constrained, the availability of saltwater is unlimited [32]. If 25% of current freshwater recirculating systems were replaced with once-through seawater cooling,

made possible by PHX technology, the U.S. electric grid would gain 1.47 GW of generating capacity without construction of additional power plants.

The next section reviews the embodied energies of polymers and polymer composites and compares them with metallic materials used in seawater heat exchangers. A lower embodied energy can be an important factor in the life cycle energy use of a heat exchanger, as will be shown later in a case study in Chapter 2.

1.4.6 Embodied Energy of Polymer Heat Exchangers

Embodied energy refers to the total energy required to bring a material to its final form. This collective energy value includes energy required for material production, product manufacture, product use, and product disposal. The determination of the embedded energy of polymer composites is more complex because the value is a function of more than one material. In the next chapter, polymer composites with enhanced thermal conductivity are discussed in more detail. In this section, the composites are exclusively thermoplastics filled with short carbon fibers. In examining polymer composites, Suzuki and Takahashi [40] estimated the energy content of polypropylene to be 24 MJ/kg and more than ten times that value – 286 MJ/kg – for carbon fibers. These values include the energy for raw material production and the processing and assembly of the polymer and fibers. It is noteworthy that the energy content value for the fibers was 286 MJ/kg in 2004, which represented a large decrease from the 478 MJ/kg estimated in 1999 [40]. It is expected that the energy content of pitch-based fibers will continue to decrease as production increases and lower energy content stocks are used as raw material.

The energy content of three polymer composites were estimated: a low-k composite with an aligned-direction thermal conductivity of 5 W/m·K, a medium-k composite with a conductivity of 10 W/m·K, and a high-k composite with a conductivity of 20 W/m·K. The energy content of polymer composites is the sum of the energy content of the polymer and the fibers, based on their respective weight fractions. The required volume fraction, and corresponding weight fraction, of carbon fibers to achieve the selected conductivities was calculated according to the Nielsen model [41], which is provided in Equations 1.7-1.10.

$$\frac{k}{k_m} = \frac{1 + AB\varphi_2}{1 - B\varphi_2} \quad (1.7)$$

$$A = k_E - 1 \quad (1.8)$$

$$B = \frac{\frac{k_f}{k_m} - 1}{\frac{k_f}{k_m} + A} \quad (1.9)$$

$$\varphi = 1 + \left(\frac{1 - \varphi_m}{\varphi_m^2} \right) \varphi_2 \quad (1.10)$$

where k is the composite conductivity, k_m and k_f are the thermal conductivity of the matrix (0.25 W/m·K) and filler (550 W/m·K), respectively. The density of the matrix is 1.169 g/cm³, and the density of the fibers is 2.2 g/cm³. "A" is a parameter based on the fiber aspect ratio and its orientation, calculated using the Einstein coefficient k_E . φ_2 is the fiber volume fraction and φ_m is the maximum packing fraction. The A parameter is equal to two times the fiber aspect ratio (aspect ratio = 20) parallel to uniaxial oriented fibers, and A equals 0.5 perpendicular to uniaxial oriented fibers [41]. The maximum packing fraction for three-dimensional random fibers is 0.52 [41]. The embedded energy of the polymer composites is compared to the embedded

energy of corrosion resistant materials in Table 2. The results show that polymer composites bridge the gap between low thermal conductivity, low energy content unfilled polymers and high conductivity, high energy content metals. The material of choice in corrosion resistant applications is titanium, which has excellent corrosion resistance and can withstand high velocities (to minimize biological fouling) without experiencing erosion/corrosion. Another common, and more traditional, choice in seawater systems is copper-nickel alloys, which inhibit biological fouling and resist corrosion well [42]. Certain aluminum alloys are widely used in marine applications because they show good corrosion resistance, favorable strength, and good weldability. However, aluminum and its alloys generally do not inhibit biological fouling, which can decrease performance significantly [43].

Table 2 Thermal conductivity and embodied energy of corrosion resistant materials
[40][44][45][45]

Material	Density (g/cm³)	Thermal conductivity (W/m·K)	Embodied Energy (MJ/kg)	Embodied Energy (GJ/m³)
Unfilled polymer	1.20	0.25	24	29
Low-k composite (46 wt. %)	1.49	5	145	216
Medium-k composite (62 wt. %)	1.65	10	187	309
High-k composite (74 wt. %)	1.79	20	219	392
Titanium	4.50	20	1000	4500
Copper-nickel	8.90	45	72	641
Aluminum Alloy 5052	2.68	138	306	820

When comparing the embodied energy of the materials in Table 2, titanium stands out as the most energy intensive material. A single kilogram requires 1000 MJ to be produced [44], while a raw polymer requires only 24 MJ. The three polymer composites have different weight fractions of carbon fibers embedded in the polymer matrix. Nielsen’s model shows that increasing the fiber content increases the thermal conductivity of the composite. Accordingly; the low-k, medium-k, and high-k composites have carbon fiber weight fractions of 46%, 62%, and 74%, respectively. Since carbon fibers have high embodied energies, increasing the fiber content in a composite increases the embodied energy proportionately to the weight fraction. The embodied energy per unit volume of polymer composites offer further improved performance relative to metals (as shown in Table 2), due to the relatively lower density of polymer composites. Furthermore, the embodied energy per unit volume provides the best comparison among materials for a fixed volume. It may thus be surmised that the use of polymer composites may offer similar heat transfer performance and corrosion resistance of a metallic heat exchanger, while offering lower embodied energy and cost.

1.5 Energy Education and Research Collaboration (EERC)

The work in this dissertation has been largely funded by the Energy Education and Research Collaboration (EERC) between the University of Maryland and The Petroleum Institute at Abu Dhabi. The project was originally focused on the use of polymer heat exchangers in seawater cooling used in the liquefaction of natural gas. The goal of the project was to develop a systematic approach for designing polymer heat exchangers that accounts for all life cycle considerations: thermal performance, structural performance, manufacturability, and life cycle cost (e.g., manufacturing, installation, operation, maintenance). The work in this dissertation has been focused primarily on thermal performance and manufacturability, while other students involved in this project focused their theses work on other aspects [46][47][48].

1.6 Dissertation Goals

The goals of this dissertation are:

- Identify the current state-of-the-art of raw polymers and polymer composite heat exchangers
- Develop an integrated design methodology for polymer heat exchangers using thermo-fluid and manufacturing considerations
- Demonstrate the new design methodology by creating a design tool that highlights the value of integrating thermal and manufacturing considerations
- Develop and/or identify optimal heat exchanger geometries that take advantage of the intrinsic properties of polymer composites
- Develop an understanding of the process-induced properties in polymer composites, and their effect on polymer heat exchanger performance

1.7 Approach

The following is a summary of the research activities in this dissertation:

- Reviewed history and new developments in PHX
- Developed thermofluid analysis tool for HX using classical analytical solutions
- Defined methodology for manufacturability tool for PHX
- Developed integrated design tool for PHX
- Applied design tool to classical plate-fin geometry
- Identified novel HX geometry and demonstrate advantages
- Developed thermofluid analysis tool for novel HX geometry
- Identified a novel HX manufacturing process and demonstrated feasibility for PHX

1.8 Dissertation Structure

In Chapter 1, the history of polymer heat exchangers was reviewed as well as current applications. It was noted that corrosive applications are the main user of polymer heat exchangers. The low thermal conductivity of a raw polymer is a major impediment for the widespread application of polymers in heat exchangers. The potential benefits of using polymer composites for seawater applications were identified. It was shown that the use of polymers in seawater heat exchangers could potentially bring along significant energy and water savings.

In Chapter 2, thermally enhanced polymers is discussed more in depth. This family of polymers bridges the gap between unfilled polymers and corrosion resistant metals.

Several case studies are used to illustrate the modeling approach and to highlight potential benefits of polymer composites in seawater applications.

In Chapter 3, a systematic approach to the design of heat exchangers made with thermally enhanced polymer composites is presented. An integrated design model is introduced that accounts for heat transfer performance, molding cost, and assembly costs. It is shown that incorporating moldability considerations directly affects the choice of optimum designs that minimize the cost.

In Chapter 4, the anisotropic variation of thermal conductivity in an injection-molded heat exchanger part is studied. Numerical predictions of the fiber orientation, coupled with the classic Nielsen model, and finite element thermal simulations, are used to determine the effect of the thermal conductivity variations on the overall performance. The use of analytical fin equations with an effective thermal conductivity is also discussed.

In Chapter 5, an in-depth study of the thermal performance of a novel gas-to-liquid webbed tube heat exchanger is presented. This novel HX an equivalent thermal performance to a plate-fin heat exchanger, while providing significant mass savings. Laboratory-scale prototype heat exchangers were built using injection molding and fused deposition modeling, and were tested in a cross flow air-to-water test facility. An effective thermal conductivity was deduced by comparing experimental results to analytical and numerical results.

Finally, in Chapter 6, a summary of the dissertation is presented along with a description of the intellectual contributions of this work.

2 Thermal design of polymer composite heat exchangers

This chapter summarizes some of the modeling done to evaluate thermally enhanced polymer heat exchangers. The results from the modeling reveal the true role of thermal conductivity in gas/liquid heat exchangers, while highlighting the potential energy and water savings brought on by the use of thermally enhanced polymers in seawater heat exchangers.

2.1 Properties of polymers

In a recent review paper, T'Joel et al. [49] assessed the merits of PHXs for Heating, Ventilation, Air Conditioning, and Refrigeration (HVAC&R) applications. They also compiled data for physical and thermal properties of relevant polymers that can be used in heat exchangers, as shown in Table 3. Unless otherwise stated, the properties in Table 3 were taken at 25 °C. Note that all the materials listed here have very low densities, especially when compared to metals. However, the main limitations of polymer materials can be seen in their low strength, low thermal conductivity, and low operating temperature, when compared to an annealed aluminum alloy commonly used in HVAC&R heat exchangers [50]. It is important to note that some polymers can absorb a significant amount of water (or other fluids) when exposed to moisture. Most notably, polyamides can absorb up to 2% by volume of moisture. This can cause swelling, cracking, and penetration to the substrate of a lined component. Swelling can also lead to softening of the material, with losses in tensile strength and modulus [3].

Table 3 Thermal and mechanical properties of raw polymers [3]

Properties and unit	Polymer material									
	AA3003*	FEP	PA 6	PC	PEEK	PFA	PTFE	PVDF	PPS	PP
Specific gravity	2.71	2.12-2.17	1.12-1.14	1.2	1.3-1.32	2.12-2.17	2.14-2.20	1.77-1.78	1.35	0.9-0.91
Water absorption (24 hr at 23 °C), %		<0.01	1.3-1.9	0.15	0.5	0.03	<0.01	0.03-0.08	0.01-0.07	0.01-0.03
Tensile strength at break, MPa	179	19-21	41-165	63-72	100	28-30	21-34	24-50	48-86	31-41
Tensile modulus, GPa	69	0.34	2.6-2.8	2.4	3.4	0.48	0.40-0.55	1.38-552	3.3	1.14-1.55
Elongation at break, %		250-330	30-100	110-120	50	300	200-400	12-600	1.6	10-600
CTE, \square m/m-°C	7.2	1.5-1.9	144-149	122	4.7-11	140-218	126-216	126-256	49-88	146-180
Thermal conductivity W/m-K	169	0.25	0.24	0.20	0.25	0.25	0.25	0.10-0.13	0.08-0.29	0.12
Deflection temperature at 1.8 MPa, °C		51	68-85	120-135	160	48	46	84-118	100-135	49-60
Max. operating temperature, °C	400-500	190	79-150	120-135	250	260	260	160	230	82

Note: Unless otherwise stated, properties are given at 25 °C. Properties of annealed aluminum alloy AA3003 are shown for comparison in the second column [50]

Another property not listed in Table 3 is the permeability of the polymer. Polymers can have an order of magnitude greater permeability than metals, which makes this property a fundamental consideration when designing heat exchangers. Other aspects that are important to consider when designing with plastics are creep and stress relaxation, which are a result of the viscoelastic behavior of polymers. Finally, note that common fillers such as glass fibers are generally used to increase the material strength, stiffness, chemical resistance, dimensional stability, heat resistance, and moisture resistance [3].

2.2 Introduction to Thermally Enhanced Polymers

In 2004, Zweben reviewed in detail the use of fillers with very high thermal conductivity in composite materials, with special attention paid to polymer matrix composites, most notably, fiber-filled composites [51]. Composites with thermal conductivities up to two orders of magnitude higher than un-reinforced plastics can be produced with the use of pitch-based carbon fibers, along with “vapor-grown” fiber and carbon nano-tubes, which offer very high conductivities (~ 1000 W/m·K for

fibers, >2000 W/m·K for nano-tubes). The production costs of these fillers, however, and of the resulting composites still remain relatively high compared to more common carbon-based fillers [51]. Also, the thermal conductivities achieved in polymer composites are generally highly anisotropic, depending on the alignment of the filler particles inside the matrix. In the most extreme cases, out-of-plane conductivities can be as much as one order of magnitude lower than in-plane conductivities. Table 4 provides a list of selected commercially available “thermally-conductive” polymers, along with important mechanical and thermal properties. These composites have improved impact strength, and yield strength, well above those of the raw polymers. Note that PPS and liquid crystal polymers (LCP) composites have relatively high heat deflection temperatures and tensile strengths. The heat deflection temperature, HDT, is the temperature at which a polymer deforms to a standard deflection under a specified load. HDT provides a basis for comparison among polymers and often serves to define the upper-bound operating use temperature of the subject materials [52].

Table 4 Thermal and mechanical properties of commercially available thermally-enhanced polymeric materials [53]

Vendor	Matrix	Thermal Conductivity (W/m·K)	Tensile Strength (MPa)	Tensile Modulus (GPa)	Density (g/cc)	HDT @ 1.8 MPa (°C)
Cool Polymers	PPS	20	45	13	1.7	260
Cool Polymers	PP	5	25	5.2	1.38	-
Sabic IP	PPS	7/2.2	139	27.6	1.74	270
Sabic IP	PA 6/6	1.2	95	11.9	2.04	216
PolyOne	PPS	10-11	100	26.2	1.82	282
PolyOne	LCP	18-20	103.4	20.7	1.82	277
PolyOne	PA 12	10	110	20.7	1.61	185
RTP	LCP	18.01	45	24.1	1.7	232
RTP	PPS	2.31	62	26.2	1.7	260
Ovation Polymers	PC	6.1	59	6.9	1.45	136

Note: HDT = heat deflection temperature.

2.3 Gas/Liquid Heat Exchanger with Polymer Composites

2.3.1 Role of thermal conductivity

To understand the role of thermal conductivity, Luckow et al. [54] studied the thermofluid characteristics of a seawater-methane heat exchanger module made with thermally-enhanced polymer composites and targeted for use in the liquefaction of natural gas on offshore platforms. The main goal of this study was to evaluate the thermal performance of polymer composites having a range of thermal conductivities comparable to those of corrosion-resistant metals (5-40 W/m·K). Using the ϵ -NTU method and well-established heat transfer correlations, the heat transfer rate of a conceptual plate-fin heat exchanger module was determined for a range of plate-fin dimensions and gas flow velocities (hot gas at 90°C cooled by 35°C seawater). The analysis was extended to include metrics that could account for the energy invested in the heat exchanger, starting from the pumping power and including the energy required for formation and fabrication (manufacturing). The fabrication energy, generally proportional to the mass of the heat exchanger, could constitute a large fraction of the total lifetime energy consumption, especially for heat exchangers with short service lives.

The heat transfer rate of the 1 m by 1 m module under study was found to be relatively insensitive to thermal conductivity, down to approximately 5 W/m·K, due to the dominance of the gas-side thermal resistance. In this application, if the thermal conductivity is only 0.25 W/m·K (unfilled polymer), approximately two thirds of the thermal resistance is contributed by the gas side, and the remaining one third essentially by conduction through the wall. However, if the thermal conductivity is 10

W/m·K (polymer composite), the contribution of the wall drops to approximately 10% with nearly 90% of the thermal resistance contributed by the gas side. Careful inspection of Figure 9 reveals that at a pumping power of 200 W (for both fluids), a carbon-filled polymer composite having a thermal conductivity of 5 W/m·K yields a heat transfer rate of 5.5 kW, which is close to 85% of what could be achieved with a copper heat exchanger ($k= 300$ W/m·K) with the same dimensions and fluid velocities. Once the thermal conductivity of the polymer composite reaches 10 W/m·K, 92% of the thermal performance of copper could be achieved, while a conductivity of 20 W/m·K (equivalent to the thermal conductivity of titanium) would provide 95% of the performance achieved by a copper heat exchanger.

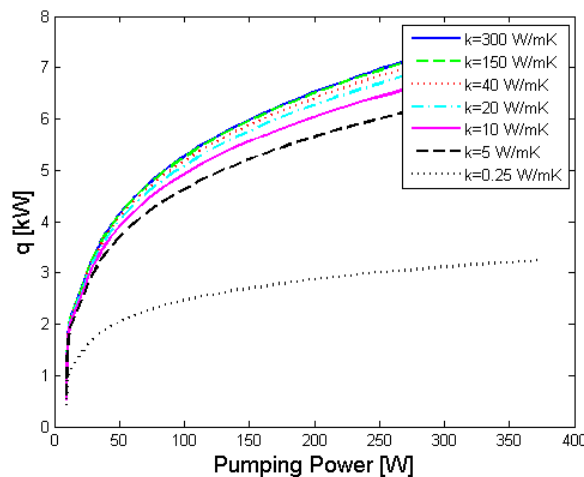


Figure 9 Analytically predicted gas/liquid thermal performance in a counterflow plate-fin heat exchanger
Plate width and length =1 m, fin height=10 mm, fin and wall thickness=1 mm, liquid velocity: 1 m/s, no. of fins on
methane side=100, no. of fins on water side=5 [54]

The energy efficiency of various heat exchangers can be characterized using the Total Coefficient of Performance, or COP_T , defined as the ratio of the lifetime heat transfer rate to the sum of the lifetime pumping power and the manufacturing energy, i.e., the ratio of energy transfer to energy input [54].

$$\text{COP}_T = \frac{q_T t_L}{W_{PP} + W_M} \quad (2.1)$$

For the corrosive environment of the LNG application examined in [54] and shown in Figure 10, comparison of the filled polymers with unfilled polymer and corrosion resistant titanium, as well as copper and aluminum, with an assumed useful life of 1 year, highlights the dominant role of the fabrication energy in the COP_T . Due the high levels of energy invested in manufacturing titanium (1,000 MJ/kg), this material displays a far weaker optimum and a plateau-like dependence of the COP_T on pumping power, barely reaching 10. On the other hand, aluminum's high conductivity (150 W/m·K) compensates in part for the high energy content and reaches a COP_T of 40. It is noteworthy that copper (300 W/m·K) and copper-nickel alloy (40 W/m·K), with their moderate energy content, perform similarly, with peak COP_T values around 45, in spite of their conductivities being quite different. Due to its low energy content, the unfilled polymer displays the highest values of COP_T , reaching 83 at low pumping powers, despite yielding low heat transfer rates. The weakening influence of pumping power on heat transfer rate, displayed in Figure 9, contributes to the second salient trend visible in Figure 10. At approximately 40 W of pumping power, the polymer composites reach a COP_T of about 60, and then decrease towards a common asymptote of 20 – for polymer and metallic materials alike – as the pumping power increases and begin to dominate the denominator of the COP_T .

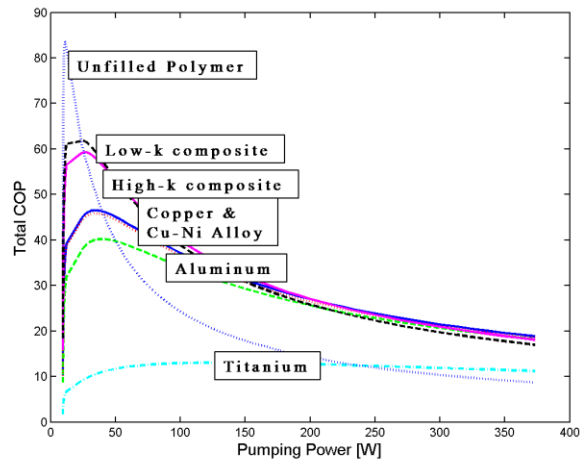


Figure 10 Gas/Liquid COPT in a counterflow parallel plate heat exchanger

Plate width and length= 1 m, fin height =10 mm, fin and wall thickness 1 mm, seawater velocity: 1 m/s, no. of fins on methane side =100, no. of fins on water side =5, HX lifetime: 1 year [54]

2.3.2 Case Study 1: Liquefaction of Natural Gas Using Seawater

The process of liquefaction of natural gas requires large amounts of heat to be extracted from the feed gas. A single production train requires a multitude of heat exchangers to bring the feed gas to cryogenic temperatures. Many of these exchangers utilize copious amounts of water as the coolant. In Das Island, an island off the coast of Abu Dhabi, 5.5 billion kilograms of liquefied natural gas (LNG) are produced in a year [55]. There, 135 million kilograms of cooling seawater per hour are needed not only for process coolers but for ancillary equipment as well [55]. The use of seawater can meet the need of a water-thirsty operation such as LNG production, not only in Das Island, but in very many locations around the globe. For this LNG case study we have chosen to focus in a single heat exchanger module of a gas cooler. After being compressed to 1200 kPa, a multi component refrigerant vapor (MCR) composed of various hydrocarbons (methane, propane, butane) goes into a heat exchanger at 60 °C to be cooled by seawater coming in at 35 °C [55]. For

simplicity, we model the hydrocarbon vapor as only methane and set a target heat transfer rate of 1MW. The HX module is a doubly finned square plate with 1 m on each side arranged in a counterflow configuration (see Figure 11). The plate and fin thickness is held constant at 2 mm, and the fin height is 10 mm. Since the water-side has a sufficiently high heat transfer coefficient, fins are needed only on the methane side to reduce the gas-side thermal resistance but fin-like ribs are present on the water side mostly for structural support. There are only 20 water-side fins, while there are 80 fins on the methane-side to increase the wetted area. The mass flow rates into the module are 0.1 kg/s and 15 kg/s for methane and seawater, respectively. Once the value of the heat transfer rate for a single module is calculated, the number of modules is increased until the target heat duty (1MW) is achieved.

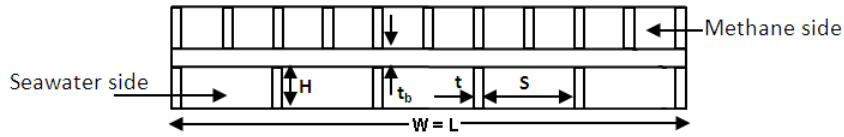


Figure 11 Methane/Seawater HX Module

(Length L = Width W = 1m, Plate thickness t_b = Fin thickness t = 2mm, Fin height H =10mm, 20 water-side fins, 80 air-side fins, m_{methane} =0.1kg/s, m_{seawater} =15kg/s)

At the flow rates defined above, the Reynolds numbers were $\sim 10,000$ for the methane-side, and $\sim 40,000$ for the water-side, so the velocity and temperature profiles are always turbulent. Appropriate friction factor and Nusselt number correlations were identified for this study. The friction factor for fully developed turbulent flow in a smooth duct was provided by Pethukov [56]:

$$f_{fd} = \frac{1}{(0.79 \ln Re_{D_h} - 1.64)^2} \quad (2.2)$$

$$\text{for } 3000 < Re_{D_h} < 5.0 \times 10^6$$

where Re_{D_h} is the Reynolds number based on the hydraulic diameter D_h . The apparent friction factor due to the effect of the developing region can be approximated by [57]:

$$\bar{f} \approx f_{fd} \left(1 + \left(\frac{D_h}{L} \right)^{0.7} \right) \quad (2.3)$$

where L is the flow length. The total pumping power is defined as the product of the pressure drop Δp and the volumetric flow rate \dot{V} :

$$P = \{\Delta p \dot{V}\}_{\text{methane}} + \{\Delta p \dot{V}\}_{\text{water}} \quad (2.4)$$

where the pressure drop, is the sum of the friction and dynamic (entrance and exit) losses:

$$\Delta p = f \frac{L}{D_h} + K_{L,\text{entry}} + K_{L,\text{exit}} \quad (2.5)$$

The Nusselt number for fully developed turbulent flow was provided by Gnielinski [58]:

$$Nu_{fd} = \frac{(f_{fd}/8)(Re_{D_h} - 1000)Pr}{1 + 12.7\sqrt{f_{fd}/8}(Pr^{2/3} - 1)} \quad (2.6)$$

$$\text{for } 0.5 < Pr < 2000 \text{ and } 2300 < Re_{D_h} < 5.0 \times 10^6$$

where Pr is the Prandtl number. The average Nusselt number was approximated by Kakac et al. [59] for the developing region, as:

$$\bar{Nu} \approx Nu_{fd} \left[1 + C \left(\frac{x}{D_h} \right)^{-m} \right] \quad (2.7)$$

where x is the location along the flow length. Typical values of C and m are 1.0 and 0.7 [57].

The heat transfer rate, \dot{q} , of a heat exchanger can be calculated using the ε -NTU method:

$$\dot{q} = \varepsilon q_{\max} = \varepsilon C_{\min}(T_{i,1} - T_{i,2}) \quad (2.8)$$

where C_{\min} is the smallest heat capacity of the two fluids. The effectiveness, ε , of a counterflow heat exchanger is:

$$\varepsilon = \frac{1 - e^{[-NTU(1-C_r)]}}{1 - C_r e^{[-NTU(1-C_r)]}} \quad (2.9)$$

where C_r is the ratio of the fluids' heat capacities, and NTU is the number of transfer units, defined as:

$$NTU = \frac{UA}{C_{\min}} \quad (2.10)$$

Examining the variation of the heat transfer rate of the LNG gas cooler module with thermal conductivity of the plate and fin material, shown in Figure 12, reveals an asymptotic relationship between q and k . Thus, an unfilled polymer with a thermal conductivity of 0.25 W/m·K yields a transfer rate of 1.4 kW, while for an enhanced polymer, with a thermal conductivity of 5 W/m·K, the heat transfer rate more than doubles and the module transfers 3.3 kW. However, further increases in thermal conductivity yield only marginal improvements in heat transfer rate. The plot shows that above a thermal conductivity of 20 W/m·K, the heat transfer rate reaches a plateau at a value of 4 kW. This behavior is due to the relatively low heat transfer coefficient on the gas-side (120 W/m²K), which creates a thermal resistance on the gas-side of 3.48×10^{-3} K·m²/W (relative to base area, not finned area). This gas-side thermal resistance constitutes 97% of the overall thermal resistance (3.59×10^{-3} K·m²/W). Note that at a thermal conductivity of 20 W/m·K, the wall thermal resistance is only 0.1×10^{-3} K·m²/W, so further improvements in thermal conductivity

will not yield significant reductions of the overall thermal resistance. Note also that in seawater heat exchangers, fouling resistances on the seawater-side can often reach values of $0.2 \times 10^{-3} \text{ K}\cdot\text{m}^2/\text{W}$ [55], which can become dominant if all other thermal resistances are negligible, i.e., the heat transfer coefficients and the thermal conductivity are sufficiently high.

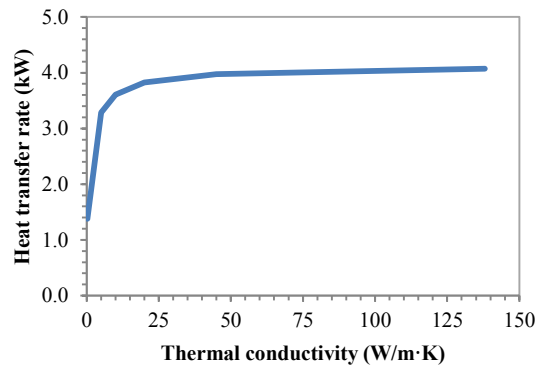


Figure 12 Heat Transfer Rate of an LNG Train Gas Cooler Module as a Function of Thermal Conductivity
(L=W=1m, $t_b=t=2\text{mm}$, H=10mm, 20 water-side fins, 80 air-side fins, $m_{\text{methane}}=0.1\text{kg/s}$, $m_{\text{seawater}}=15\text{kg/s}$, $T_{\text{methane,inlet}}=60^\circ\text{C}$, $T_{\text{water,inlet}}=35^\circ\text{C}$)

Using the calculated heat transfer rate, and taking into account the density of each material (shown in Table 2), the amount of heat transfer per kilogram of heat exchanger mass can be calculated and compared, as in Figure 13. The polymer composites are ahead of the rest of the materials due to favorable thermal conductivity and relatively low density. It is interesting to point out that the increase in performance due to a higher thermal conductivity is offset by the increase in density due to the higher fiber content in the medium-k and high-k polymer composites, and so they transfer less energy per kilogram. Due to their high density, titanium and copper-nickel transfer less than half the energy transferred by the enhanced polymer composites per unit mass, while the aluminum alloy can transfer only 70% the energy of the enhanced composites. An unfilled polymer can transfer more per kilogram than titanium and copper nickel due to its low density and to the

relatively small role of thermal conductivity in the heat transfer rate shown in Figure 12.

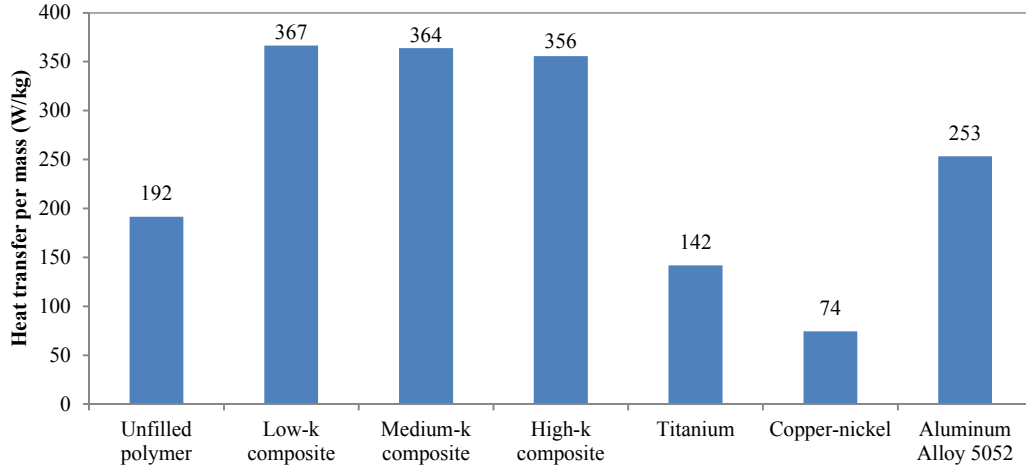


Figure 13 Heat Transfer per Kilogram of Heat Exchanger Mass

($L=W=1\text{m}$, $t_b=t=2\text{mm}$, $H=10\text{mm}$, 20 water-side fins, 80 air-side fins, $m_{\text{methane}}=0.1\text{kg/s}$, $m_{\text{seawater}}=15\text{kg/s}$, $T_{\text{methane,inlet}}=60^\circ\text{C}$, $T_{\text{water,inlet}}=35^\circ\text{C}$)

The results from Figure 13 can help in investigating the overall energy expenditures of a 1MW-methane cooler. By taking into account the embodied energy and the energy required to pump both fluids, the overall energy expenditures related to a 1MW methane cooler can be compared for all materials, as is shown in Figure 14 below for a heat exchanger life of 1, 5 and 10 years. The values in the plot reveal that, in general, the high-k composite requires the least amount of energy, followed by copper-nickel, aluminum, and the other enhanced polymers. Titanium and the unfilled polymer require the most energy of the six materials. Titanium's main energy expenditure is due to its embodied energy. On the other hand, the low thermal performance of the unfilled polymer has a two-fold effect: first, considerable energy must be invested in pumping the fluid to increase the heat transfer rate; second, more mass is required to add heat transfer area, though this effect is very small due to its low embodied energy.

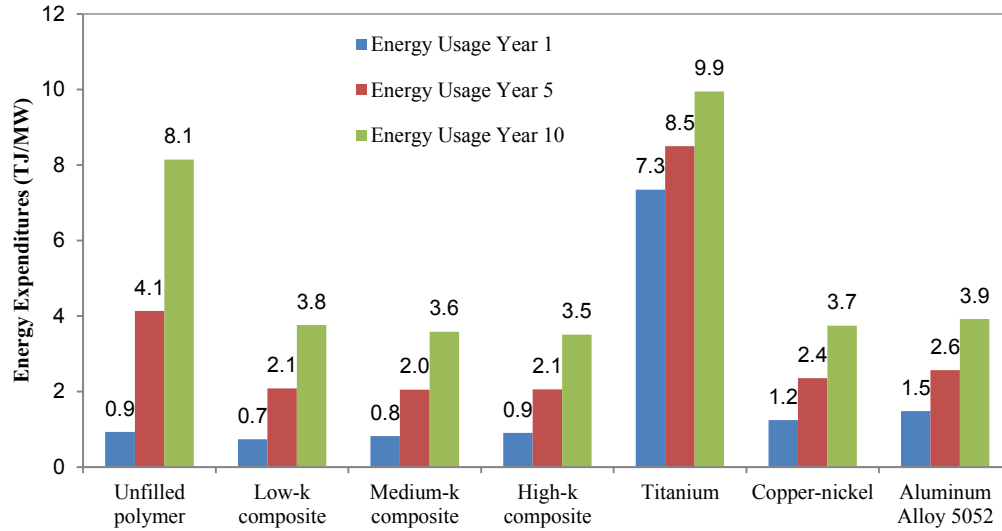


Figure 14 Overall energy expenditures of a 1MW-methane-cooler

($L=W=1\text{m}$, $t_b=t=2\text{mm}$, $H=10\text{mm}$, 20 water-side fins, 80 air-side fins, $m_{\text{methane}}=0.1\text{kg/s}$, $m_{\text{seawater}}=15\text{kg/s}$, $T_{\text{methane,inlet}}=60^\circ\text{C}$, $T_{\text{water,inlet}}=35^\circ\text{C}$)

2.3.2.1 Energy Savings

During the first year, the main energy expenditure for all materials, except the unfilled polymer, is their embodied energies. Interestingly, among the composites, the high-k polymer uses more energy than the others only in the first year, which follows directly from the behavior observed in Figure 13. By year 10, for most materials the main energy consumption is related to the power needed to pump the two fluids. It is instructive to separate the energy used in 10 years into two categories: embodied and pumping energy as shown in Figure 15. Note that even after ten years most of the energy used by a titanium heat exchanger (70%) is the material's embodied energy. Over a life a ten years, a 1MW-heat exchanger using an enhanced polymer composite with a thermal conductivity of 20 W/m·K uses around 6.5 TJ less than a titanium heat exchanger; even a composite with a conductivity of 10 W/m·K uses 6.2 TJ less than titanium. A copper-nickel alloy uses 0.24 TJ more than a high-k composite, and 0.17 TJ more than a medium-k polymer composite. An aluminum alloy uses 0.42 TJ more than a high-k composite and 0.340 TJ more than a medium-k polymer composite.

It is important to note that a medium-k ($k=10 \text{ W/m}\cdot\text{K}$) composite HX uses less energy over a life of 10 years than all the corrosion resistant metals shown in Figure 14. Even though a high-k composite HX uses even less energy, it is perhaps not recommendable to use a composite material with such a high filler fraction given the manufacturing issues associated with high filler-loading [60]. Thus, the medium-k composite would be a preferable choice.

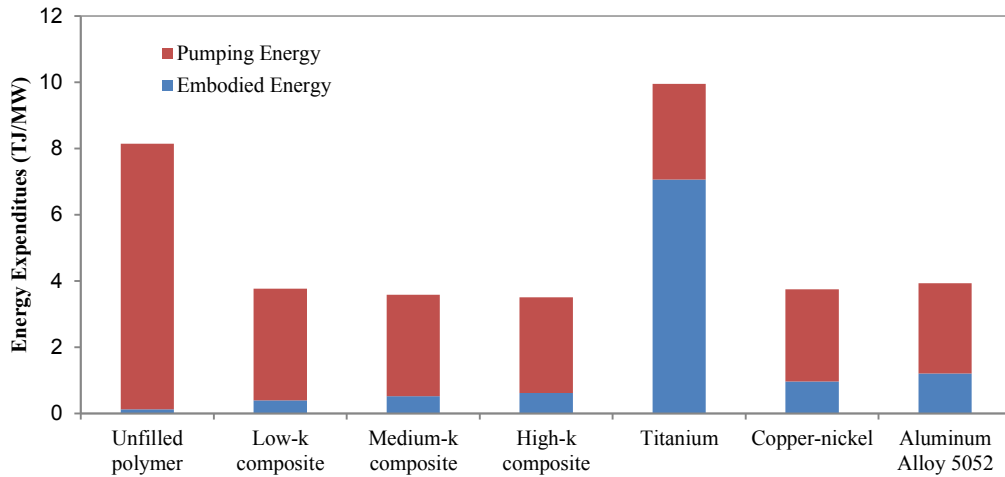


Figure 15 Energy Expenditures of a 1MW Methane Cooler for a 10-year Life

($L=1\text{m}$, $t_b=t=2\text{mm}$, $H=10\text{mm}$, 20 water-side fins, 80 air-side fins, $m_{\text{methane}}=0.1\text{kg/s}$, $m_{\text{seawater}}=15\text{kg/s}$ -flow rates are per HX module-, $T_{\text{methane,inlet}}=60^\circ\text{C}$, $T_{\text{water,inlet}}=35^\circ\text{C}$)

2.3.2.2 Freshwater Savings

A single 1MW methane cooler made of a medium-k polymer composite requires 124 billion kilograms (roughly 125 billion liters) of water in a year. If seawater is used instead of freshwater, the reduction in freshwater withdrawals can be significant given that a heat exchanger of only 1 MW requires such large amounts of water (Note that seawater has higher density and higher viscosity than freshwater, so a minor increase in pumping power can be expected).

2.3.3 Case Study 2: Water-to-Seawater Heat Exchanger

Seawater may also be used to extract heat from freshwater running in a closed loop circuit in power plant applications. This type of indirect cooling may be necessary when the cooling medium needs to be freshwater or a mixture of freshwater and ethylene glycol, for example. Seawater is often not used if fouling creates a large performance gap between freshwater and seawater systems. However, if significant fouling can be avoided, seawater becomes a great secondary cooling medium for indirect systems. For this case study, we revisit the counterflow HX used as a methane cooler (see Figure 11 in the previous case study, but instead apply it as a freshwater to seawater heat exchanger. Freshwater at 90 °C is to be cooled by seawater at 35 °C at the inlet. The flow rate for both hot and cold fluids is 15 kg/s. Using Equations 2.2-2.10, the heat transfer rate was calculated for this heat exchanger, and it is plotted as a function of thermal conductivity in Figure 16. The plot shows a similar behavior to that observed in Figure 12 for a methane cooler, where a maximum heat transfer rate is reached quickly after a certain thermal conductivity threshold. In this case, at a thermal conductivity of 0.25 W/m·K the heat exchanger can only transfer 2.3 kW. Once a thermal conductivity of 5 W/m·K is reached, the heat exchanger transfers 3.3 kW, very close to a maximum heat transfer rate of 3.4 kW. While similar, the behavior observed in Figure 16 differs from that in Figure 12 in that once the conductive thermal resistance is reduced by increasing the thermal conductivity, the overall thermal resistance is reduced to a value close to its minimum value, or the overall thermal conductance UA is very close to its maximum value. Thus at $k > 5$ W/m·K, the heat exchanger effectiveness defined in Equation 2.9

approaches a value of 1, and the heat transfer rate approaches its thermodynamic limit defined in Equation 2.8 as q_{max} . Figure 17 below shows how the wall thermal resistance, initially at $0.008 \text{ K}\cdot\text{m}^2/\text{W}$, vanishes for $k > 5 \text{ W/m}\cdot\text{K}$ to less than $0.0004 \text{ K}\cdot\text{m}^2/\text{W}$, and since the heat transfer coefficients are relatively high around $10,000 \text{ W/m}^2\text{K}$, the convective thermal resistances are less than $0.0001 \text{ K}\cdot\text{m}^2/\text{W}$. Further improvements in thermal conductivity increase the heat transfer rate only marginally since the heat exchanger effectiveness is already near its maximum value of 1.

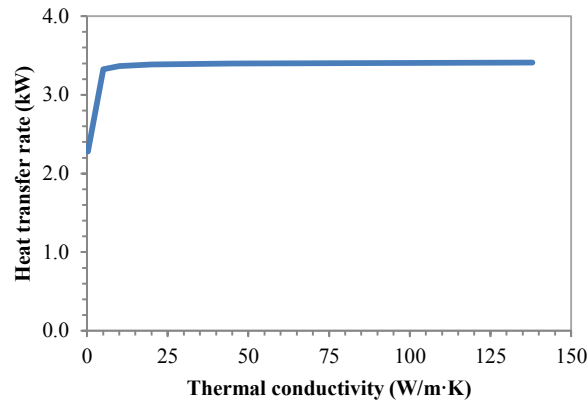


Figure 16 Heat transfer rate of a water-to-seawater HX module as a function of thermal conductivity
(L=W=1m, $t_b=t=2\text{mm}$, H=10mm, 20 water-side fins, 20 seawater-side fins, $m_{\text{water}}=15\text{kg/s}$, $m_{\text{seawater}}=15\text{kg/s}$, $T_{\text{seawater,inlet}}=90^\circ\text{C}$, $T_{\text{water,inlet}}=35^\circ\text{C}$)

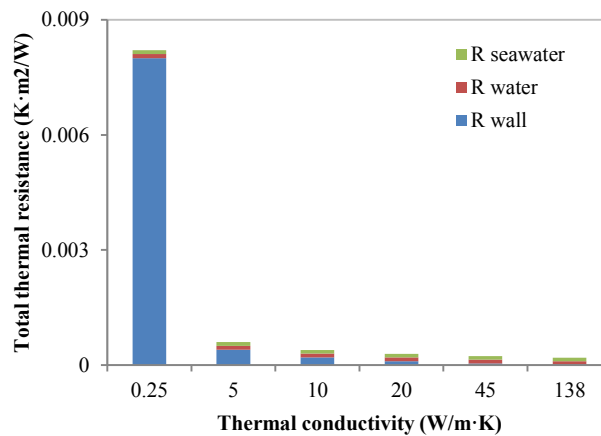


Figure 17 Thermal resistances in a water-to-seawater HX module as a function of thermal conductivity
(R values are relative to base area, L=W=1m, $t_b=t=2\text{mm}$, H=10mm, 20 water-side fins, 20 seawater-side fins, $m_{\text{water}}=15\text{kg/s}$, $m_{\text{seawater}}=15\text{kg/s}$, $T_{\text{seawater,inlet}}=90^\circ\text{C}$, $T_{\text{water,inlet}}=35^\circ\text{C}$)

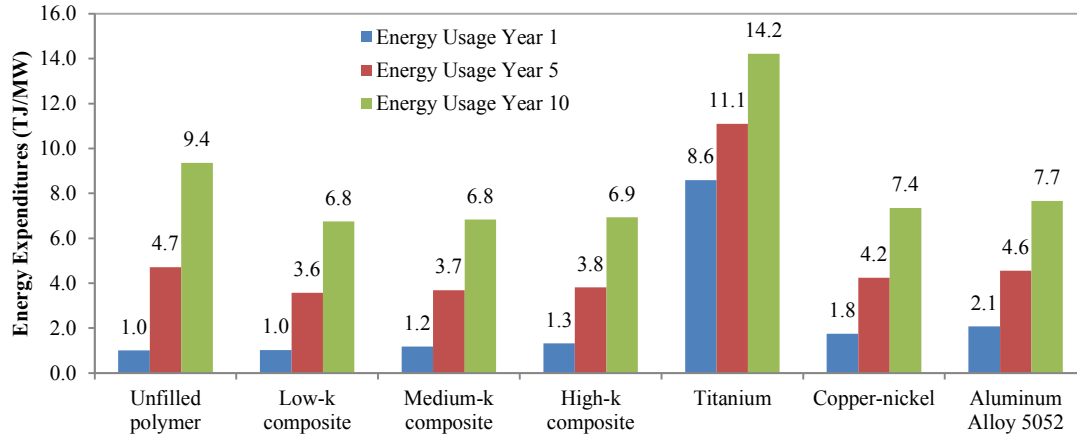


Figure 18 Overall energy expenditures of a 1MW water-to-seawater heat exchanger

($L=W=1\text{m}$, $t_b=t=2\text{mm}$, $H=10\text{mm}$, 20 water-side fins, 20 seawater-side fins, $m_{\text{water}}=15\text{kg/s}$, $m_{\text{seawater}}=15\text{kg/s}$, $T_{\text{seawater,inlet}}=90^\circ\text{C}$, $T_{\text{water,inlet}}=35^\circ\text{C}$)

2.3.3.1 Energy Savings

Looking now at the overall energy expenditures, shown in Figure 18, it can be seen that the enhanced composites are again the most energy efficient, followed by copper-nickel. In this case, the low-k polymer is the better of the composites instead of the medium-k and high-k polymers in Case Study 1. The marginal improvements in heat transfer rate provided by the medium-k and high-k composites are offset by the increase in embodied energy due to the higher carbon-fiber fraction. Over a life of 10 years, a 1MW-heat exchanger using an enhanced polymer composite HX with a thermal conductivity of 5 W/m·K uses 7.5 TJ less than a titanium heat exchanger, while a composite with a conductivity of 20 W/m·K uses 7.3 TJ less than titanium. A copper-nickel alloy HX uses 0.60 TJ more than a low-k composite HX and 0.42 TJ more than a high-k polymer composite HX. An aluminum alloy HX uses 0.90 TJ more than a low-k composite, and 0.72 TJ more than a high-k polymer composite. In this case, it is clear a HX made with a 5 W/m·K polymer composite is sufficient to outperform the corrosion resistant metals and also its fellow polymer composite HXs.

2.3.3.2 Freshwater Savings

A single 1MW water-to-seawater exchanger made with a 5 W/m·K polymer composite requires 142 billion kilograms (roughly 143 billion liters) of seawater in just a year. If freshwater were to be used as a coolant as opposed to seawater, the increase in freshwater use would undoubtedly be significant.

2.3.4 Case Study 3: Ocean Thermal Energy Conversion

Ocean Thermal Energy Conversion (OTEC) uses the temperature gradient between surface water and water at depths of several hundred meters to drive a low-efficiency thermodynamic cycle. OTEC is feasible in regions where the temperature difference between deep water and surface water is between 20-25°C. Closed cycles are the focus of this case study.

In closed cycles, warm water vaporizes a low boiling point working fluid (e.g., ammonia), after which the working fluid expands through a turbine that is connected to a generator. The working fluid is condensed using cold seawater and then pumped back to the evaporator to repeat the cycle. In a hybrid cycle, warm surface water is evaporated at low pressure and then the steam passes through a heat exchanger where it vaporizes the working fluid. The working fluid passes through a turbine and then through the condenser, where it is cooled using cold seawater. After condensing, the working fluid repeats the cycle.

There are currently nine operational OTEC facilities worldwide. Five facilities in the United States and Japan have demonstrated electricity generation via OTEC and two facilities in India have demonstrated desalination via OTEC. Estimates of the potential energy provided from OTEC vary widely. A reasonable estimate based on

the literature available is 43,800 TWh annually [61], of which 350 TWh is practical near or onshore [62]. Global electricity generation totaled 18,800 TWh in 2007 [63]. A primary limitation to widespread adaptation of OTEC has been high costs, which have been said to range from \$0.08-\$0.24/kWh [64]. The leading contributors to high costs are the high pumping power requirements and the use of expensive corrosion-resistant material in large heat exchangers. As such, development of low-cost high-volume heat exchangers could play an important role in the growth of electricity-generation via OTEC.

The heat transfer performance of an ammonia evaporator was modeled following the model given by Panchal [65] for a plate fin evaporator. The model assumes that annular flow prevails in the heat exchanger, preceded by slug flow. In annular flow, heat transfer through the film is assumed to be governed by conduction, and momentum changes in the film are negligible. Also, the flow of liquid is assumed to be evenly distributed on the fin and the plate. The following geometric and flow parameters were taken directly from Panchal’s work [65] and used in this analysis:

Table 5 Ammonia evaporator dimensions [65]

Ammonia side	
No. of fins	530
Fin thickness	0.4 mm
Fin height	7 mm
No. of channels	9
wall thickness	2.9 mm
Water side	
No. of fins	22
Fin thickness	3.2 mm
Fin height	19.7 mm
No. of channels	8
Wall thickness	2.9 mm
Overall	
Width	73 cm
Length	4.7 m
Height	25 cm

The heat transfer rate of the ammonia evaporator is shown in Figure 19 as a function of thermal conductivity. Seawater flowing at a volumetric rate of $0.2 \text{ m}^3/\text{s}$ at $26 \text{ }^\circ\text{C}$ at the inlet is used to evaporate ammonia flowing at $0.0016 \text{ m}^3/\text{s}$ at $17 \text{ }^\circ\text{C}$ at the inlet. It can be seen that the heat transfer rate is very sensitive to conductivity in the range of 0 to $150 \text{ W/m}\cdot\text{K}$. At a conductivity of $0.25 \text{ W/m}\cdot\text{K}$, the evaporator only transfers 23 kW, and if the conductivity is increased 20-fold to $5 \text{ W/m}\cdot\text{K}$ it transfers 143 kW (vapor quality at the outlet = 10%). Further improvements in the thermal conductivity increase the heat transfer rate even more, reaching 900 kW (outlet vapor quality = 74%) at $140 \text{ W/m}\cdot\text{K}$. In this case study, copper-nickel was not used in the comparison, since it is not compatible with ammonia [66]. Also, at $0.25 \text{ W/m}\cdot\text{K}$, evaporation did not occur in the exchanger, and so it was excluded from the analysis since its resulting energy cost was prohibitively larger than the others materials.

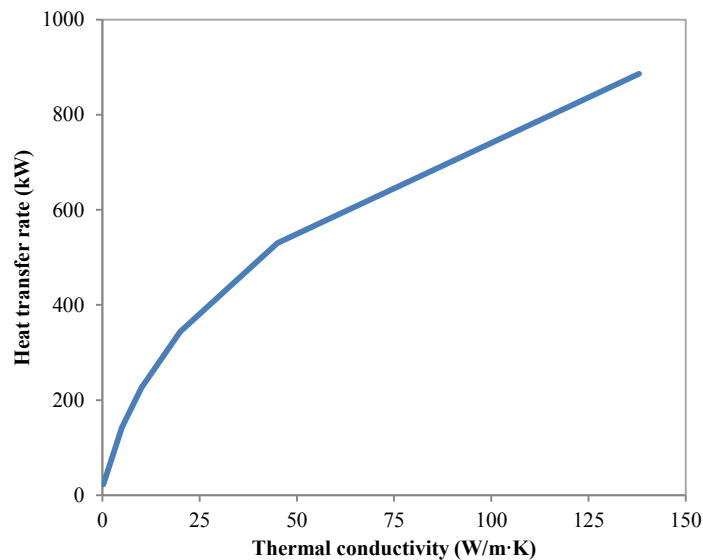


Figure 19 Heat transfer rate of an ammonia-to-seawater hx module as a function of thermal conductivity (Seawater: $0.2 \text{ m}^3/\text{s}$, $T_{\text{inlet}}=26 \text{ }^\circ\text{C}$, ammonia: $0.0016 \text{ m}^3/\text{s}$, $T_{\text{inlet}}=17 \text{ }^\circ\text{C}$, see Table 5 for HX dimensions)

2.3.4.1 Energy Savings

Following the trend seen in Figure 19 and the results of the previous case studies, the most energy efficient evaporator is the one made with a lightweight material with relatively good thermal conductivity and with low embodied energy. The aluminum alloy uses significantly less energy than every other material applied to a 2MW ammonia evaporator (see Figure 20 below). The high-k composite follows as the second most energy efficient material. The increase of embodied energy with respect to the other composites is offset by the significantly improved thermal performance. The overall energy expenditures reveal just how critical the thermal conductivity is for an OTEC application. When the composite conductivity is only 5 W/m-K, the extra pumping power needed to provide 2MW of heat duty is such that over ten years, the heat exchanger requires 0.300 TJ more than a titanium heat exchanger, even when the embodied energy of titanium is almost seven times higher. On the other hand, a HX made with a high-k composite requires 4.4 TJ less than if titanium were used.

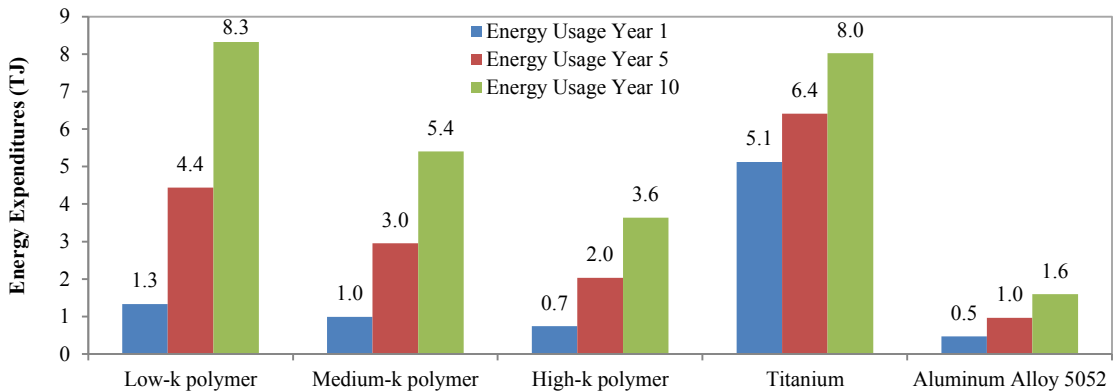


Figure 20 Overall energy expenditures of a 2MW ammonia evaporator

(Seawater: 0.2 m³/s, T_{inlet}=26 °C, ammonia: 0.0016 m³/s, T_{inlet}=17 °C, see Table 5 for HX dimensions)

2.4 Conclusions

In this section we analyzed further the inextricable relationship between energy and water discussed in Chapter 1 and identified the need for a novel cooling technology that reduces energy use and water demand. It was noted that the implementation of PHXs could offer increased electricity output while alleviating demand for freshwater. A case study of a gas/liquid HX was used to present the potential energy and water savings brought on by the use of polymer heat exchangers for seawater cooling; specifically, heat exchangers made with thermally enhanced polymers. In general, an energy efficient heat exchanger requires a lightweight material with relatively good thermal conductivity and low embodied energy. It was found that the choice of material for each of the applications studied here depends on the relationship between heat transfer rate and thermal conductivity. These results revealed that the use of seawater as a coolant appears to be a viable mechanism to reduce the use of freshwater, as long as a suitable corrosion-resistant material is used. For the methane cooler, a thermal conductivity over 10 W/m·K brings about diminishing improvements in heat transfer. Therefore, the medium-k or high-k composites are needed for the HX to use less energy than the metal HXs. In Case Study 2, however, it was found that improvements in heat transfer rate can be neglected for thermal conductivities over 5 W/m·K. Considering the relatively higher embodied energy of all metals, and the fact that a high thermal conductivity is not needed, the best suited material was the low-k polymer composite. Finally, the performance of the OTEC evaporator in Case Study 3 was found to be very sensitive to the wall thermal resistance, more specifically, to thermal conductivity. The

embodied energy was not as significant as it was for the other applications, so the aluminum alloy was the best candidate. It was followed by the high-k composite, which possesses a combination of relatively high conductivity and low embodied energy. Finally, the results in Case Studies 1 and 2 revealed that the use of seawater as a coolant appears to be a viable mechanism to reduce the use of freshwater, as long as a suitable corrosion-resistant material is used.

3 Incorporating Moldability Considerations during the Design of PCHX

This chapter presents a systematic approach to the design of plate-fin heat exchangers made with thermally enhanced polymer composites. We have formulated the design problem as a life cycle cost minimization problem. The integrated design model introduced here accounts for heat transfer performance, molding cost, and assembly costs. We have adopted well known models to develop individual parametric models that describe how heat transfer performance, molding cost, and assembly cost varies as a function of the geometric parameters of the heat exchanger. Thermally enhanced polymer composites behave differently from the conventional polymers during the molding process. The desired thin walled large structures are expected to pose challenges during the filling phase of the molding process. Hence we have utilized experimentally validated simulations to develop a metamodel to identify difficult and impossible to mold design configurations. This metamodel has been integrated within the overall formulation to address the manufacturability considerations. This section also presents several case studies that show how the material and labor cost strongly influence the final design.

3.1 Introduction

Polymer manufacturing processes available today vary in cost according to complexity, size, and quality of the part. Injection molding is a popular high-throughput manufacturing process, and is often used to make geometrically complex shapes in a wide variety of sizes. Hence this process is naturally suited for making polymer composite heat exchangers (PCHX) parts that have complex surface

enhancements. From an injection molding perspective, thermally enhanced polymer composites can exacerbate flow length limitations (flow length is the length a polymer will flow before solidifying in a channel [52]). For carbon fiber-filled polymers, the presence of a high-fiber fraction in the matrix will cause the viscosity of the melt to increase [67]. A higher viscosity causes the flow length of the polymer inside the mold to be reduced, for a fixed injection pressure and melt temperature. Additionally, fibers with high thermal conductivity increase the cooling rate of the melt as it flows in the mold reducing the flow length even further. While a higher injection pressure can increase polymer flow length, excessively high injection pressures may require a high-clamping-force machine, which increases production costs [68] and may lead to defective parts [69]. Similarly, the use of higher melt temperatures to increase the flow length increases the molding cycle time, which adds to production costs as well.

When designing heat exchangers using thermally enhanced polymers, many issues arise, concerning the physical characteristics of these new composite materials, and the design process can be seen as the integration of multidisciplinary tools that address the molding considerations and meet certain heat transfer and pumping power requirements.

A finned plate is a building block for making an important class of heat exchangers. Plate-fin heat exchangers are compact heat exchangers that provide increased surface area per unit volume. A plate with rectangular fins is a simple geometry but yet reveals the complexities in optimizing heat exchangers. Hence, in this chapter we have focused on this simple geometry. Often, heat transfer performance,

manufacturing cost, and manufacturability considerations are in conflict with each other. For example, thin plates are good for heat transfer but they pose a major manufacturability problem. Similarly, larger plates provide more surface area, but a larger projected area is more difficult to manufacture. There are many such conflicts related to the number of fins and their thickness. For example, many fins provide structural support and surface area; however, the addition of fins increases the manufacturing cost, so selecting the optimal design parameters becomes a non-trivial task. This study illustrates the complexity in the PCHX design.

In more advanced designs of heat exchangers, small flow breaking features are added to the fins to introduce turbulence. These features make finned plates truly three-dimensional in nature. For such three dimensional polymer composite shapes, injection molding is the only viable process option. For the sake of brevity, in this chapter we restrict our discussion to simple fins.

3.2 Overview of Integrated Design Model for Polymer Heat Exchangers

The next section focuses on determining the heat transfer rate and pumping power. Next follows a section on the cost of injection-molding. A moldability metamodel is introduced next, based on injection-molding simulation data. Then, a model to determine the cost of assembling a heat exchanger using finned plates is discussed. Lastly, results using all models to determine a heat exchanger costs are presented and discussed.

Table 6 Design variables

Design Variable	Parametric Range
Base length, L	200 mm – 1000 mm
Base thickness, t_b	1 mm – 4 mm
Fin spacing, S	3 mm – 20 mm
Fin thickness, t	1 mm – 5 mm

Table 6 above shows the parametric ranges of the four geometric variables chosen for this study. The lower and upper boundaries of the design variables were identified based on heat transfer considerations and molding limitations. As an initial requirement, a heat transfer rate of at least 1 kW was chosen to be a performance minimum for a single module. A base length of 200 mm was identified to provide heat transfer rates of roughly 1 kW, for the flow parameters defined in section 3.3.1. A maximum base length was chosen based on knowledge of current manufacturing process limitations, given that parts with large projected areas require very large machines. Similarly, minimum base and fin thickness were chosen based on molding limitations. The range of fin spacing considered reflects the need for a minimum number of fins to achieve significant heat transfer enhancement. Fin height was left as a constant in this analysis ($H = 10$ mm) after an initial exploratory analysis of simulation data suggested that the effect of fin height on mold filling would not be as significant as the other variables.

The cost of the heat exchanger can initially be described as:

$$\text{HX Cost} = C_{\text{molding}} + C_{\text{assembly}} \quad (3.1)$$

However, the cost in Eqn. (3.1) only reflects manufacturing considerations and does not take into account the energy needed to operate the heat exchanger. Alternatively, the pumping power cost may be included if a life cycle cost is desired:

$$\text{LC Cost} = \text{HX Cost} + C_{\text{pumping}} \quad (3.2)$$

The polymer heat exchanger geometry can be optimized by selecting the set of four geometric variables that yields the lowest cost. Examples of searching for the minimum cost are shown in the results section. Even though the examples shown in the results section are limited to the use of Eqn. (3.1) and do not consider the cost of pumping the fluids through the heat exchanger, the topic is briefly mentioned in the following section.

3.3 Determination of Heat Transfer rate and Pumping Power

3.3.1 Heat Transfer Rate

The determination of heat transfer rates and required pumping power is done using standard analytical models for counterflow heat exchangers. In this paper, these calculations are performed for a single module, a diagram of which is shown in Figure 21. The hot fluid is methane gas with an inlet temperature of 90 °C, while the cold fluid is seawater with an inlet temperature of 35 °C. The choice of fluids is based on a possible application of thermally enhanced polymer heat exchangers to the cooling of off-shore natural gas using seawater [70]. Natural gas (composed mostly of methane) is cooled at different stages in the process of liquefaction, and seawater is often the most abundant coolant available at off-shore and seaside locations.

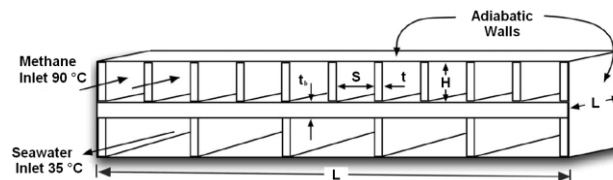


Figure 21 Seawater-methane heat exchanger module

The determination of the heat transfer rate for a single module provides the basis for calculating the number of modules needed to transfer any given amount of heat. For the sake of brevity, the modeling of heat transfer performance and pumping power is omitted here since we have discussed it in previous chapters. The goal of this section is to understand the heat transfer rate's dependence on the four selected design variables. The following parameters were assumed to be constant:

Fin spacing on water side = 50 mm
Fin thickness on water side = 2 mm
Fin height (both sides) = 10 mm
Thermal conductivity of the wall = 10 W/m·K

In designing a heat exchanger, the fins are mostly useful where the largest thermal resistance occurs. In the case of a gas-liquid heat exchanger, the largest convective resistance is that of the gas side. Since no thermal improvement is needed for the convective resistance of the cooling water, the spacing and the thickness of the fins on the water side are held constant. Reflecting specified operating conditions for the industrial gas liquefaction process, the gas and liquid flow rates are also held constant.

Careful study of the heat transfer rate in Figure 22 revealed that increasing the base length has a significant effect on the overall heat transfer rate due to the increase in base area (Figure 22a). On the other hand, increasing the thickness of the base plate increases its conductive thermal resistance, and thus reduces the heat transfer rate (Figure 22b). However, the conductive thermal resistance (for a thermal conductivity of 10 W/m·K) is always much smaller than the convective resistance on the gas side, so increasing t_b causes only a very small reduction in heat transfer rate.

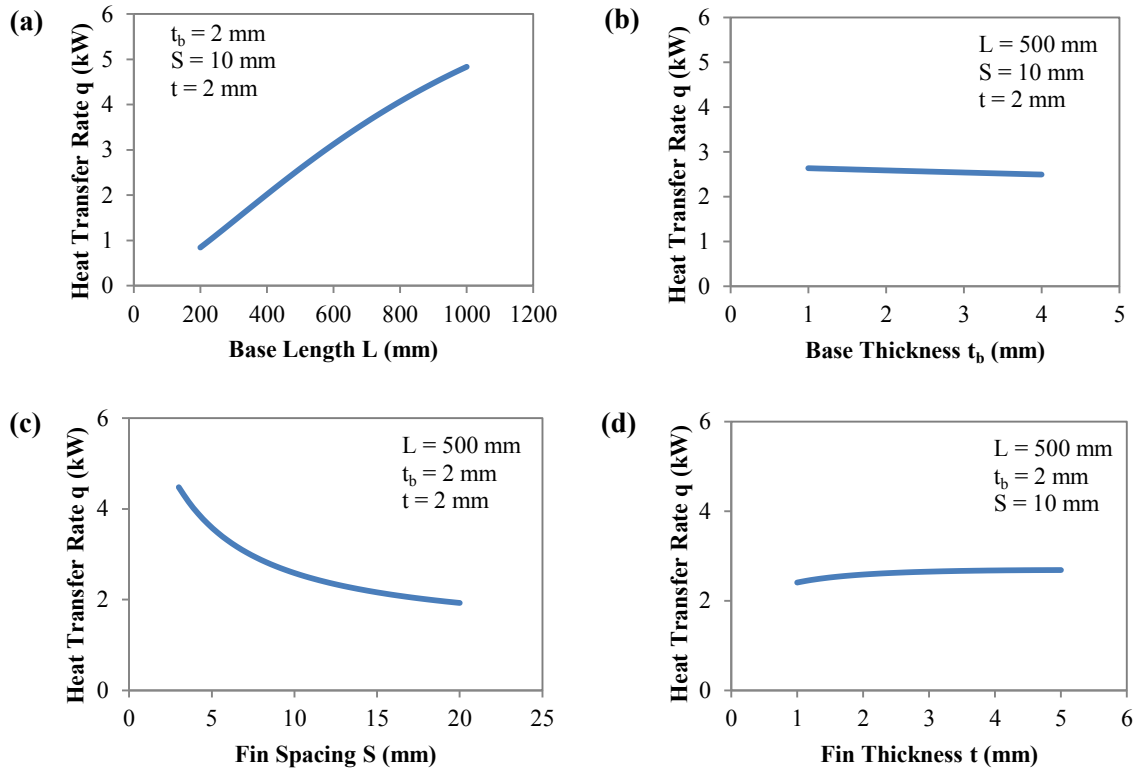


Figure 22 Heat transfer rate for a counterflow HX module
 (a) Base Length L , (b) Base Thickness t_b , (c) Fin Spacing S , (d) Fin Thickness t . (Methane: $0.1099 \text{ m}^3/\text{s}$, inlet 90°C . Seawater: $0.018 \text{ m}^3/\text{s}$, inlet $= 35^\circ\text{C}$)

Fin spacing has a significant effect on the heat transfer rate. Having more fins (lower spacing) increases both the heat transfer coefficient and the wetted area, and thus improves the heat transfer rate (Figure 22c). Finally, varying fin thickness has only a small positive effect on the heat transfer rate. While it is intuitive to expect a better heat transfer rate from a thicker fin, thicker fins decrease the number of fins (and number of flow channels) that can fit on the plate, which decreases the total flow area and increases the average fluid velocity, if the flow rate is constant. This results in a higher heat transfer coefficient that could improve the transfer rate. But, this effect is opposed by a reduction of wetted area and fin efficiency, so the net improvement is very small (Figure 22d).

3.3.2 Pumping Power and its Cost

Figure 23 shows the parametric variation of the overall pumping power required with respect to the key design variables. For a constant flow rate, increasing the plate length, L (and the width since we have assumed that the plate is square), reduces the mean fluid velocity, u_m , and also reduces the pressure drop (the increase in friction losses due to longer flow lengths is too small to increase the pressure drop). Similarly, increasing the fin spacing makes the hydraulic diameter larger and also reduces the fluid velocity (due to fewer channels). Therefore, the pumping power decreases, but at a slower rate than it does for increasing L . Recalling that in the previous section it was noted that having thicker fins reduces the free-flow area and increases the fluid velocity, so will the pressure drop increase due to the change in mean fluid velocity.

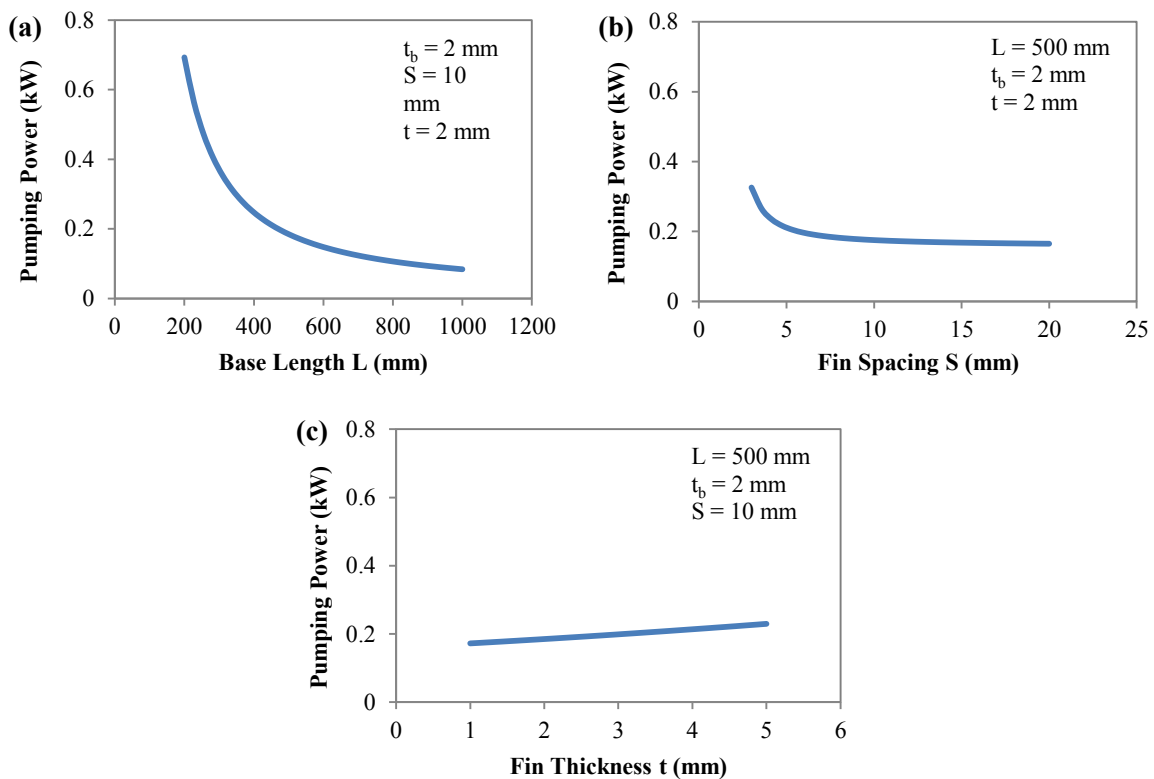


Figure 23 Pumping power for a counterflow HX module
(a) Base Length L , (b) Fin Spacing S , (c) Fin Thickness t (Methane: 0.1099 m³/s, inlet 90 °C, seawater: 0.018 m³/s, inlet 35 °C)

We can account for the total cost of pumping both fluids across the heat exchanger, by assuming a nominal lifetime, and a cost for the energy required to pump the fluids. The cost associated with providing this pumping power can be found as the product of the pumping power of a single module, the number of modules for the required heat load, a nominal lifetime t_{LC} , and a unit energy cost, E .

3.4 Injection Molding Cost Determination

Currently, there are many models available that can be used to determine the cost of manufacturing a molded component. These cost estimation models vary in complexity, but in all the models the total cost of manufacturing is equal to the sum of: material cost, tooling cost, and production cost.

To develop a molding cost metamodel, we have two options. The first option involves estimating various components of the processing time using first principles. The method described in the book by Boothroyd et al. [68] gives a method and equations for doing this. However, the cost data published in the book is rather dated. So we have chosen to follow a statistical approach to building a cost metamodel. We have fitted an equation to cost data generated by using a popular on-line molding cost estimation tool: Custompartnet.com. This method works well for parameterized geometries and is applicable to designs involving relatively small number of parameters (less than 10). The fitting procedure is automated. So this approach can be easily adapted to other design configurations and materials. The number of coefficients in the resulting equation appears to be consistent with the large number of coefficients used in the first-principle based equations that capture cooling time, mold resetting time, mold filling time, mold machining time, and mold finishing time.

An approach based on first principles would be more suitable for more complex designs. However, that will require updating cost data.

The cost provided in Custompartnet.com is composed of three factors: material cost, production cost, and tooling cost. A sketch of a modular finned plate is shown in Figure 24. The cost estimate is obtained by inputting the basic geometric parameters of the part that is to be molded:

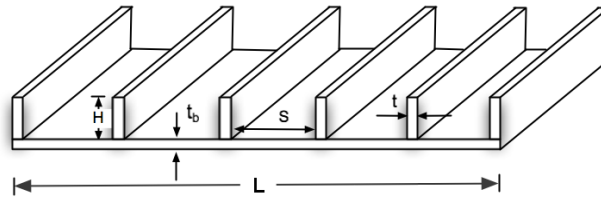


Figure 24 Square Finned Plate

Part envelope: $[x, y, z]$ dimensions of smallest box that can contain the part = $[L, L, t_b + H]$

Maximum wall thickness: thickest feature of a part (needed for cooling time calculations) = $\max(t_b, t)$

Projected area: area projected onto mold surface (parting direction assumed to be along height of fins) = L^2

Volume: total volume of plate = $L^2 \cdot t_b + N \cdot L \cdot H \cdot t$

Feature count: for a finned plate = number of fins N

Parting surface: surface where mold halves meet = flat

Production quantity: assumed to be low-volume production = 10,000

Material: closest to Nylon 12 in the available library was Nylon 6 (a price adjustment is discussed later in this section and was used in determining the results in later sections).

Other features: This part requires no side action, side cores, lifters, or unscrewing devices; and the surface roughness and tolerance are not critical in this application. The cost metamodels were generated using 50 design points (combinations of the four design variables) for which the three cost components were obtained from Custompartnet.com, as previously outlined. The choice of design points was started with a two-level factorial design for the four variables at their highest and lowest value ($2^4=16$ design points). Then, 8 combinations of center points and high/low values were added to the design, e.g. [L= 600 mm (center), $t_b = 2.5$ mm (center), S = 20 mm (high), $t = 1$ mm (low)]. Afterwards, other combinations of variables were added (1/3 and 2/3 of parametric range) until a model with low residuals (studentized residuals less than 3) was found for all three cost factors using Design Expert® as a tool for fitting the data.

The metamodels presented here are only a function of the design variables, and thus are limited to the geometry shown in Figure 24. The three metamodels for cost per part have high R^2 values (0.98-0.99), and are shown below:

$$C_{\text{Material}} = -5.17 + 0.0190 L - 0.531 t_b + 0.256 S + 0.313 t + 0.00362 L \cdot t_b - 0.00061 L \cdot S + 0.00221 L \cdot t - 0.0535 S \cdot t \quad (3.3)$$

$$C_{\text{Production}} = 0.424 - 0.00468 L + 0.283 t_b + 0.00368 S - 0.408 t + 0.000527 L \cdot t_b + 0.000745 L \cdot t - 0.1051 t_b \cdot t - 0.00258 S \cdot t + 7.6 \times 10^{-6} L^2 + 0.101 t^2 \quad (3.4)$$

$$C_{\text{Tooling}} = 0.111 + 0.0178 L - 0.0583 S - 0.254 t - 0.00016 L \cdot S + 0.0132 S \cdot t \quad (3.5)$$

Overall, a close agreement was observed between the model and a simulation dataset generated at random, with an average discrepancy of 9.4%. CustomPartNet does not currently support thermally enhanced polymer composites. Hence, the initial material

cost metamodel was obtained based on unfilled nylon prices (\$3.63/kg). The actual prices of composite materials with high thermal conductivity are in the range of \$20-\$60 per kilogram, based on the information provided by a vendor of the composite polymer. Therefore, for the subsequent analyses Equation 3.3 was scaled to reflect prices of composite materials. The plots herein show a scaled material cost model. Figure 25 shows sample plots of injection molding cost for a finned plate. It is evident now that the dominant factor in manufacturing a single plate is the material cost, due to the high cost of the composite material. The trends seen below agree with well-known molding rules. For example, a larger projected area (see Figure 25(a)) increases the production and tooling cost. Also, thicker parts take longer to cool in the mold, so the production cost will increase. This is shown in Figure 25(b) and (d) where the production cost increases –only slightly- for thicker plates and thicker fins, respectively. Finally, reducing the number of features in the mold (number of fins) reduces the tooling cost. Accordingly, the tooling cost decreases for a part with widely spaced fins, shown in Figure 25(c).

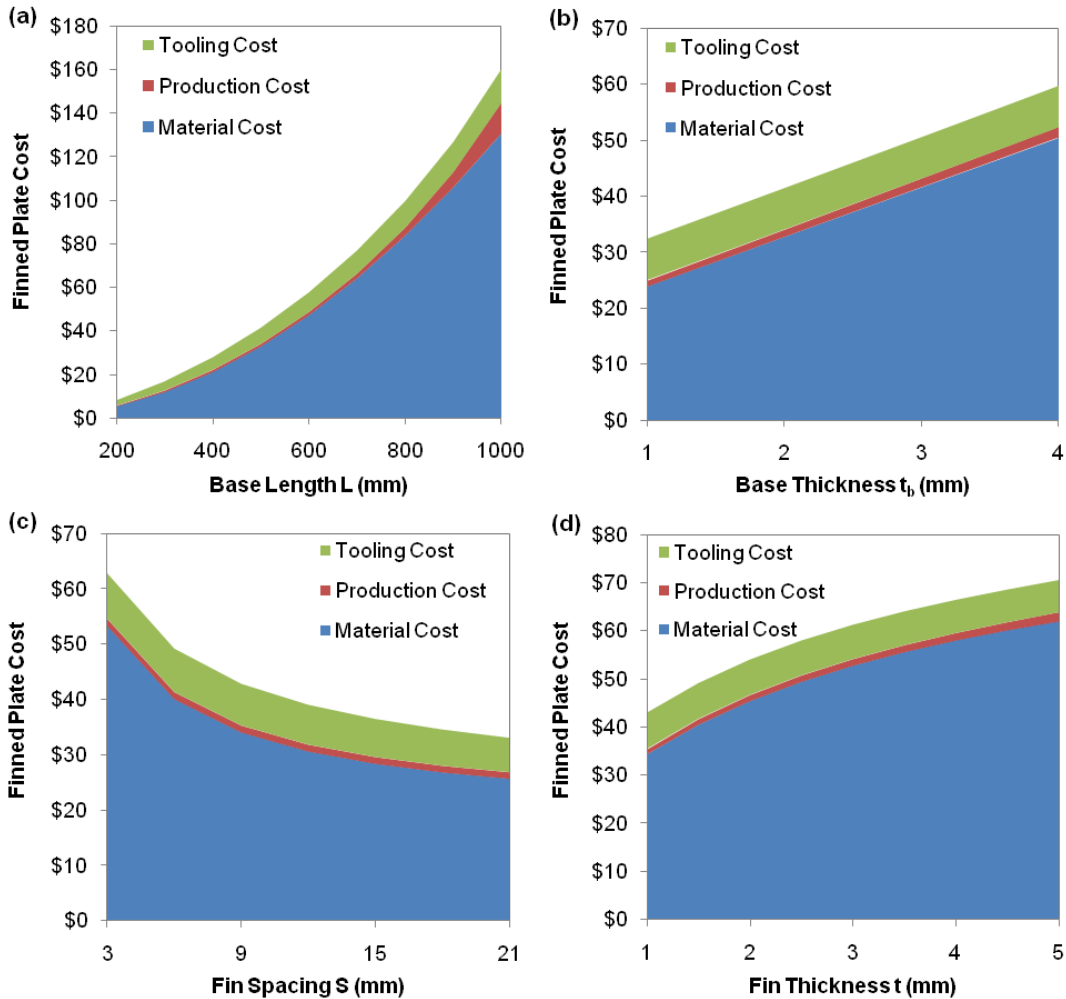


Figure 25 Finned plate cost
 As a function of (a) base length L ($t_b = 2$ mm, $S = 10$ mm, $t = 2$ mm), (b) base thickness t_b ($L = 500$ mm, $S = 10$ mm, $t = 2$ mm), (c) fin spacing S ($L = 500$ mm, $t_b = 2$ mm, $t = 2$ mm), (d) fin thickness t ($L = 500$ mm, $t_b = 2$ mm, $S = 10$ mm); Production qty. = 10,000 parts, Material = \$22/kg

3.5 A Metamodel to Account for Moldability Considerations

3.5.1 Parametric analysis using Moldflow® to develop percent filled volume metamodel

A parametric analysis for the injection molding of a square finned plate (plate shown in Figure 24) was done through a simulation-software, Moldflow®. The simulations consisted of a “Fill analysis” using a single gate placed in the center at the base of the plate. The simplicity of the geometry, made it possible to reduce computational time by choosing a 2.5 D mid-plane mesh style, although for geometries with higher complexity a 3D mesh would be required.

The polymer chosen for this study was a Nylon 12 resin filled with 50%-by-weight carbon fibers offered by a vendor. For all the simulations, the melt temperature was taken as 277 °C, which is the highest melt temperature recommend by the vendor, and the maximum injection pressure was set to 180 MPa. Finally, the mold temperature was fixed at 80 °C, which is within the mold temperature range recommended for this material. Moldflow's simulations were experimentally verified via a spiral flow length experiment, using a rectangular channel 2.286 mm wide by 1.27 mm high. This spiral mold was used to conduct filling experiments using a Babyplast injection machine to create parts with PolyOne's thermally enhanced Nylon 12. The parts were injected at two different pressures: 150 MPa and 160 MPa, with a melt temperature of 270 C. The measured length of the spirals was compared with the length predicted by Moldflow® under similar conditions. It was observed that Moldflow® predictions were approximately within 20% of the experimental measurements.

The design points chosen for the injection molding simulations were originally picked based on a two-level factorial analysis, giving 16 data points (2^4), and then expanded using adaptive sampling to 35 data points. The 19 additional points where chosen as combinations of center values, thirds and two-thirds values, and high/low values.

After initial observations, it was determined that base length (L) and base thickness (t_b) were the most influential parameters, so particular attention was devoted to having design points at many values in the range of these two variables.

When the operating conditions — such as machine shot size, flow rate profile, and injection pressure profile — are held constant, relatively simple parametric relationships can be found. If the same shot size and flow rate profile were to be used,

increasing the base length would decrease the % volume filled roughly as $1/L^2$, since the volume of a square mold increases as L^2 , and if t_b remains fixed, the maximum amount of mass injected will remain unchanged. Increasing t_b alone will cause the percent filled volume to increase linearly. This occurs because cooling time increases proportionally to t_b^2 , but the flow velocity decreases linearly with increasing t_b . This behavior is similar to what is seen in flow length vs. thickness curves commonly used in the industry.

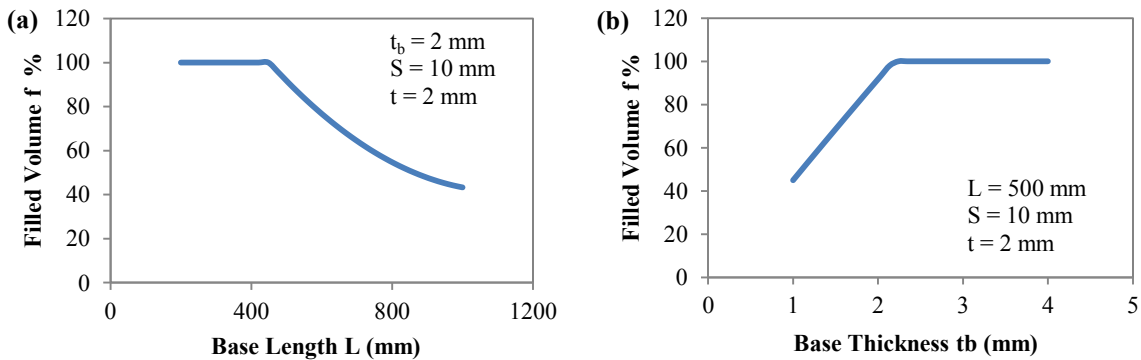
The effects of fin spacing and fin thickness are less drastic, yet they are still important. Increasing fin spacing reduces the number of fins and the total mold volume roughly as $1/S$, but it also increases the channel thickness at certain locations, which will decrease pressure drop at certain points and increase the % volume filled. Finally, fin thickness has a similar effect to base thickness, but lower in magnitude. There are also interactions between the design parameters, most notably due to changes in wall thickness in the plate-fin geometry. For example, if the base length is increased, but its thickness increased, the % volume filled will not decrease as steeply as with the original thickness.

In practice, the machine and molding process parameters have to be selected for each part geometry, and so the behavior and interactions become even more complex. Since it is difficult to account for variations in machine size and process parameters, the simple relationships described above are not sufficient to create a successful model. A more direct approach is found by using statistical techniques, such as provided by Design Expert®, to fit the Moldflow® simulation results. The simulation results were input into Design Expert® to produce a metamodel that predicts the

fraction of the volume inside the mold that can be filled with a single gate located in the center of the plate. It should be noted that the metamodel was developed using only design points in which the mold did not fill during simulations. The model is quadratic and the residual errors are less than 10% of volume filled. The metamodel has an R^2 value of 0.95 is shown below in Eqn. 3.6.

$$\begin{aligned} \phi = & 47.99 - 0.22 L + 59.82 t_b + 0.97 S + 15.36 t - 0.03 L \cdot t_b - 1.02 \times 10^{-3} L \cdot S \\ & + 0.65 t_b \cdot S - 0.12 S \cdot t + 1.32 \times 10^{-4} L^2 - 0.92 t_b^2 - 0.03 S^2 \\ & - 1.52 t^2 \end{aligned} \quad (3.6)$$

Figure 26 below shows sample plots of the percent-volume-filled meta-model as a function of the design variables. This illustrates the limited region of successful mold filling in the design space, which highlights the importance of considering such a model to distinguish between infeasible and feasible designs. Thus, for a certain base thickness, there is only a limited plate size that can be filled. Figure 26a shows that plates with base length higher than about 500 mm cannot be filled for a base thickness of 2 mm. However, the ability to fill the mold increases for thicker base plates or thicker fins, as in Figure 26b and d, respectively. Having many fins increases the total volume to be filled, and therefore the filled volume % decreases with smaller fin spacing.



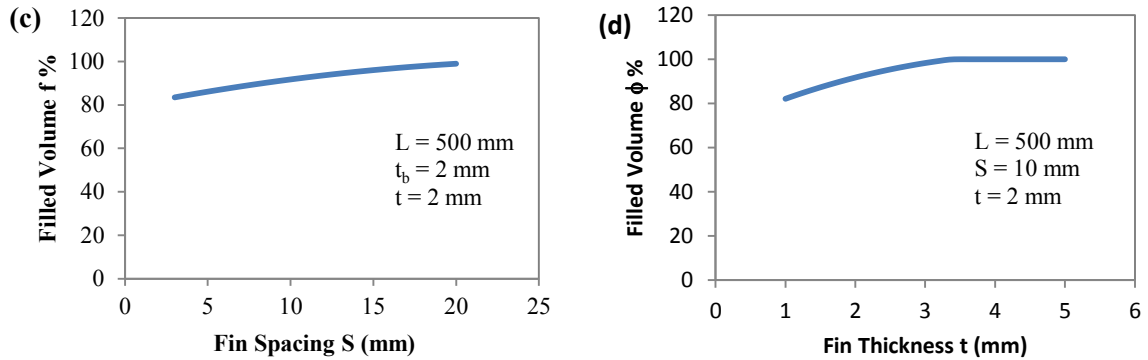


Figure 26 Filled mold volume
As a function of (a) Base Length, L ; (b) Base Thickness, t_b ; (c) Fin Spacing, S ; (d) Fin Thickness, t . (Max. Inj. Pressure = 180 MPa, Melt Temperature = 277 °C, Single Gate)

3.5.2 Using Mold-fill Metamodel to Divide Design Space

The metamodel can be used to define regions within the parametric space (Table 6) of infeasible and feasible designs. For this study, the feasibility regions were defined as follows:

For fill predictions $< 90\%$, the design is unfeasible

For fill predictions $\geq 90\%$, the design is feasible

A comparison of metamodel results and Moldflow® results was done for 42 verification points, and these fill prediction errors were translated into production cost errors as high as 21%. Also, 10% of the verifications were incorrectly identified as being infeasible designs. In light of these errors, any minimum cost solution found using this metamodel (see results section) may be refined using Moldflow® simulations around the solution point.

Alternatively, a more efficient approach for accurately defining the feasibility boundary was discussed by Hall et al [71]. The method proposed by Hall used adaptive search to locate the transition region while reducing the number of computational experiments. The method is well-suited for design exploration and

optimization and was successful in predicting the feasibility of candidate PHX designs.

3.5.3 Adjusting Production Cost Using Mold-fill Metamodel

In the introduction to this chapter we noted that the use of polymer composite can result in production cost increases. Due to the high material cost used in this study, the production cost is only a small fraction of the total molding cost. Therefore defining regions of feasibility is sufficient to account for moldability. However, if prices of thermally-enhanced polymer composites were to be drastically reduced in the future, the production cost would play a larger role in the overall cost. Thus it would be necessary to adjust the production cost near the feasibility boundary. In this section, we illustrate how such adjustments could be made with a simple example. Although these adjustments can be incorporated with little effort, the results in this chapter focus only in examples where the material cost dominates the cost of injection molding and production cost is negligible.

The regions of filled volume between 90% and 100% can be assumed to be regions where increases in melt temperature and injection pressure can help in successfully filling the mold. The production cost can be defined as [68]:

$$C_{\text{production}} = \left(\frac{N_t}{n}\right)(k_1 + m_1 F)t \quad (3.7)$$

Production cost of a single part is simply the product of the cost of operating the machine, which is defined in Equation 3.7 as a linear function of clamp force, and the cycle time. Thus, the effect of increasing melt temperature and injection pressure on both the cycle time and the clamp force must be quantified.

Recall that the cycle time is defined as:

$$t = t_I + t_C + t_R \quad (3.8)$$

where t_I is the injection time, t_C is the cooling time, and t_R is the resetting time.

The injection time can be estimated as the product of the shot volume and the ratio of the injection pressure to the injection power, as shown below [68]:

$$t_I = 2V_S \frac{p_I}{P_I} \quad (3.9)$$

where V_S is the shot volume, p_I is the injection pressure, and P_I is the injection power.

The cooling time t_C can be estimated by using a one-dimensional heat conduction equation to model the cooling of a polymer melt between two metal plates [68]:

$$t_C = \frac{D_W^2}{\kappa\pi^2} \ln \left[\frac{4}{\pi} \left(\frac{T_I - T_W}{T_E - T_W} \right) \right] \quad (3.10)$$

where κ is the thermal diffusivity of the polymer melt, T_I is the injection temperature, T_W is the mold wall temperature, and T_E is the ejection temperature.

The effects of increasing melt temperature and injection pressure can be quantified using equations 3.7-3.10. Table 7 shows the percentage increase of the main parameters in the production cost equation, assuming a 10 °C increase in melt temperature and a 20% increase in injection pressure, for example.

Table 7 Effect of melt temperature and injection pressure in production cost parameters
($T_1 = 277\text{ }^\circ\text{C}$, $T_E = 90\text{ }^\circ\text{C}$, $T_w = 80\text{ }^\circ\text{C}$)

		% increase		
		Injection time t_I	Cooling time t_C	Clamping force
Melt temperature	10 °C increase	-	1.5%	-
Injection pressure	20% increase	20%	-	20%

Examining the results of the Moldflow® simulations in the parametric range of interest, the injection times are at most ~2 seconds for a large plate, while cooling times are at most ~30 seconds. Assuming the resetting time is negligible and increasing melt temperature and injection pressure with the values in Table 7, we can estimate a cycle time increase of at most 2.7%. Finally, recalling that the cost of operating the machine is a linear function of the clamping force, a 20% increase in the clamping force will simply increase the cost by the same percentage. Combining both effects into equation 18, the production cost will increase by 23%. Assuming that this is the maximum percent increase in production cost, and that it occurs in the feasible/infeasible boundary ($= 90\%$), then a correction factor, β , can now be defined as a function of the mold-fill percent, ϕ :

$$\beta = \begin{cases} -0.0323\phi + 3.3, & 90\% \leq \phi \leq 100\% \\ 1, & \phi > 100 \end{cases} \quad (3.11)$$

Equation 3.11 simply states that if only 90% of the mold volume is filled, under the nominal operating conditions, the injection pressure and the melt temperature may be increased in order to fill the mold completely, causing a maximum production cost increase of 23%. This increase in cost decreases linearly to zero as fill-percent reaches 100%.

3.6 Determination of Assembly Cost

Selection of a cost-effective assembly method is often restricted by many different factors like part size, material, joining time. Additionally, other specifications may be set by the designer and restrict the choices even further. For a heat exchanger, it is of utmost importance that no leakage occurs from the exchanger channels. Therefore, a good seal between the exchanger plates is the first requirement for any assembly method. There are certain joining techniques that have limited part size capabilities; for example, ultrasonic welding can only be used for parts with size ranging from roughly 6 mm to 300 mm [72], so it cannot be used for the entire design range of this study. Similarly, material compatibility with the assembly technique is also an important consideration; i.e., some plastics do not weld.

For the geometries at hand, adhesive joining appears to be a logical choice of assembly technique, in order to provide good sealing of large parts at a low cost. Epoxy adhesives are low cost adhesives that are compatible with nylons. When using adhesives, a complete cost evaluation must consider several factors. Some of these factors are: amount of adhesive needed, cost of cleaning the bonding surfaces, costs of surface treatments (if needed), ventilation, and curing [72].

A more straightforward way to write the total cost of assembly may be:

$$C_{\text{assembly}} = n^{k_1} (k_2 + k_3 A_{fb}^{k_4}) \quad (3.12)$$

where n is the number of plates to be assembled, and A_{fb} is the area to which the adhesive will be applied and is defined as,

$$A_{fb} = N \cdot t \cdot L \quad (3.13)$$

k_1 and k_4 are exponents that reflect nonlinearities in the cost that arise from having more plates, or more area to be bonded. In this study, linear relationships are assumed for simplicity of the formulation, since a complete time-motion study would be required to obtain accurate values for these exponents. Therefore, we assume $k_1 = k_4 = 1$.

The coefficients k_2 and k_3 can be obtained by using handling time to calculate assembly cost for the largest and smallest parts in the design space. Handling time depends on part symmetry, size, thickness, and weight [68]. Using the standard rate for manual assembly in the state of Maryland (\$60/hr or \$1/min) as a baseline, the cost of each assembly operation can be calculated, and the coefficients follow by finding the slope and intercept of the line. The following times, shown in Table 8, were estimated based on performing assembly in our lab.

Table 8 Assembly time estimates

Part dimensions [L, t _b , S, t] in mm	[1000, 4, 3, 5]	[200, 1, 20, 1]
Handling time	2.5 minutes	5 minutes
Time to apply epoxy	2.5 minutes	5 minutes
Time for epoxy to cure	25 minutes	30 minutes
Total handling time	30 minutes	40 minutes

The values for k_2 and k_3 were then calculated to be 29.96 and 13.9, respectively.

3.7 Results and Discussion

The models presented in the previous sections can be used together to calculate the heat exchanger cost in Equations 3.1 or 3.2. In this study, we will focus only on Equation 3.1 to illustrate the use of an integrated model. As an example, a target of 500 kW was chosen as a required heat transfer rate of a polymer heat exchanger that will cool 50 m³/s of hot methane gas with 0.1 m³/s of seawater. The methane inlet

temperature is 90°C, while the seawater inlet temperature is 35°C. Depending on the plate geometry, a certain number of plates will be required to provide enough heat transfer surface area. The total number of plates had to be calculated iteratively, since additional plates will decrease the flow rate through each plate, as well as reduce the heat transfer coefficient (due to lower mean velocity). To illustrate the usefulness of the molding metamodel, the results are presented initially without considering moldability in section 3.7.1, i.e., any design in the parametric range is feasible. Then, section 3.7.2 shows how a moldability analysis drastically changes the design of a heat exchanger.

3.7.1 Minimum-cost plate geometry without moldability analysis

The effect of the design variables on the number of plates can be deduced using standard heat transfer analytical models. For example, if the plates are relatively short, many plates are needed to increase the surface area and meet the 500kW heat transfer target. As the base length is increased, the number of plates needed decreases drastically. Even though the total molding cost per plate is higher for longer plates, the reduction in the number of plates is such, that the overall cost of the heat exchanger is lower when larger plates are used, partly due to low assembly costs. These effects were summarized in Table 9 for all the design variables. If moldability were to be ignored, the plate geometry that would minimize the heat exchanger cost would simply be the lower or upper bound of each variable, following the guidelines in the last column of Table 9 ($L = 1000 \text{ mm}$, $t_b = 1 \text{ mm}$, $S = 3 \text{ mm}$, $t = 1 \text{ mm}$). It is noteworthy that without a moldability analysis, the combination of molding costs with heat transfer considerations yields some interesting results. For example, it is

preferable to have a few plates with many fins that are costly to mold, than to have many inexpensive plates with fewer fins.

Table 9 Summary of design variables effects

	per plate		per HX	
	Heat Transfer	Molding Cost	Number of plates	Overall Cost
Increase in L	Increase	Increase	Decrease	Decrease
Increase in t_b	Decrease	Increase	Increase	Increase
Increase in S	Decrease	Decrease	Increase	Increase
Increase in t	Increase	Increase	Decrease	Increase

Using the mold filling metamodel (Eqn. 3.6), the design space ($200 \leq L \leq 1000$, $1 \leq t_b \leq 4$, $3 \leq S \leq 20$, $1 \leq t \leq 5$) can be divided into feasible and infeasible regions. Since the solution would otherwise lie in the lower or upper bounds of the design variables (see Table 9), if such bounds happen to occur in the infeasible region, new bounds would then lie in the feasible boundary ($\phi = 90\%$). Finding a minimum-cost geometry now becomes much more difficult, as described next.

3.7.2 Minimum-cost plate geometry with moldability analysis

Given the complexity of the feasible boundary defined by the mold-filling metamodel, a two-level hierarchical search was used to locate minimum-cost plate geometries. At the first level, the parametric ranges were divided into large cells and a minimum value for cost was found. Then, the cells contiguous to the minimum value were subdivided into smaller cells, where a final search was done for a more refined solution. Three different scenarios were studied, and their solutions are shown in Table 10 below. In the first scenario, the nominal costs of material (\$22/kg) and assembly (\$60/hr.) defined in the previous sections were used. In the second scenario

the price of the material was doubled; while in the third scenario, the labor cost of assembly was doubled.

Table 10 Minimum-cost geometry for 500-kW HX (Methane: 50 m³/s, Seawater: 0.1 m³/s)

Scenario	L (mm)	t _b (mm)	S (mm)	t (mm)	# of plates	Cost (\$)
Material: \$22/kg Labor: \$60/hr.	872	3.52	3	2.58	26	7,179
Material: \$44/kg Labor: \$60/hr.	800	3.28	3	2.36	32	12,811
Material: \$22/kg Labor: \$120/hr.	912	3.73	3	2.44	24	8,043

The plate geometries that yield a minimum cost no longer lie in the lower or upper bounds of the design variables. In fact, the new minimum-cost solutions now lie in the feasible boundary, and these solutions cannot be found by simple inspection, as was done in the previous section.

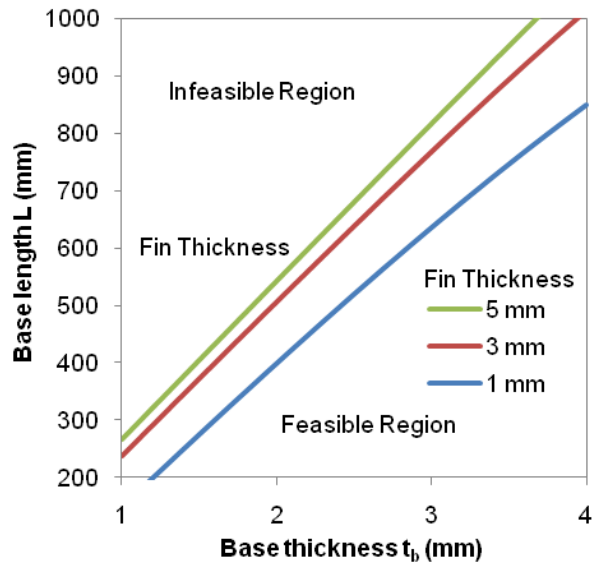


**Figure 27 Feasible boundary (mold fill % = 90)
(As a function of three of the design variables)**

Figure 27 illustrates the behavior of the feasible boundary (mold fill % = 90) as a function of three of the design variables. Base length has a linear relationship to base thickness, similar to “flow length vs. thickness” curves discussed previously. When the thickness of the fins is increased, the feasible design space becomes larger, as

seen by the shift of the boundary to the left. However, at higher fin thickness, only marginal increases of the design space are seen due to the existing flow restriction at the base prior to the fins.

Careful study of the overall heat exchanger cost along the feasible boundary can reveal why finding the minimum cost solutions is non-trivial. The heat exchanger cost is shown in Figure 28 as a function of base thickness along the feasible boundary.

Note that base length is not held constant in this plot. In fact, for the cost to follow the feasible boundary, the base length corresponds to the values shown in Figure 27, so increasing the base thickness entails increasing the base length, or vice versa. The reduction of heat transfer performance caused by a thicker base is initially offset by the increase in surface area (and heat transfer rate per plate) from having larger plates, thus the cost of the heat exchanger decreases sharply as the thickness of the base increases, following a sharp decrease in assembly costs. Eventually, the reduction of heat transfer performance due to very thick plates and the additional cost of having more material per plate starts offsetting the benefits of having larger plates, and so the overall cost starts increasing. This explains why each curve has a quadratic behavior and a single minimum. Thus, it can be said that the region to the left of the minima is dominated by assembly costs, while the region to the right is dominated by material costs.

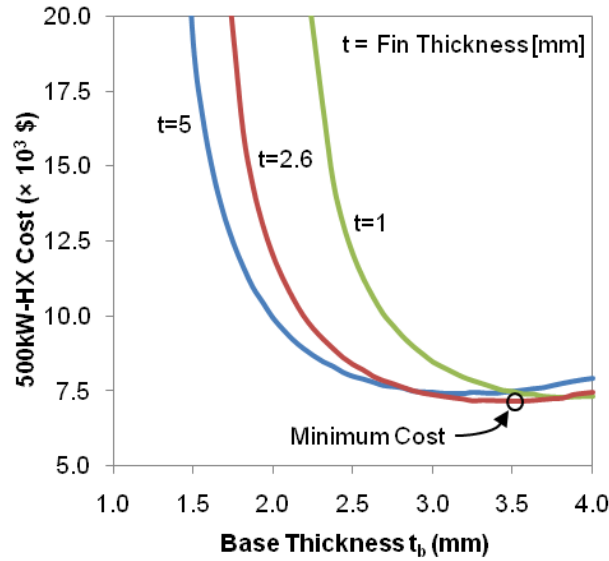


Figure 28 HX Cost along feasible boundary in scenario 1
 $(\phi = 90\%, S = 3 \text{ mm}, L = \{L | 200 \leq L \leq 1000 \text{ and } \phi = 90\%\}, \text{material: } \$22/\text{kg}, \text{assembly: } \$60/\text{hr})$

For thick fins, the heat transfer performance of each plate improves and fewer plates are needed; therefore the assembly cost is reduced. However, thick fins require more material per plate, so each plate is more expensive to mold. Due to these opposing effects, there is a single fin thickness value ($t = 2.58 \text{ mm}$) that yields a minimum cost. If the price of the material is doubled (second scenario), the base length at which the minimum cost occurs ($L = 800 \text{ mm}$) is lower than the nominal case ($L = 872 \text{ mm}$) in the first scenario. At this length, a thinner plate can be successfully filled so the base thickness decreases from 3.52 mm to 3.28 mm . Comparing Figure 29 to Figure 28, the minimum cost is seen to shift upwards and to the left. This can be visualized as an increase in size of the region dominated by material costs, or as stated before, the region to the right of the minimum cost.

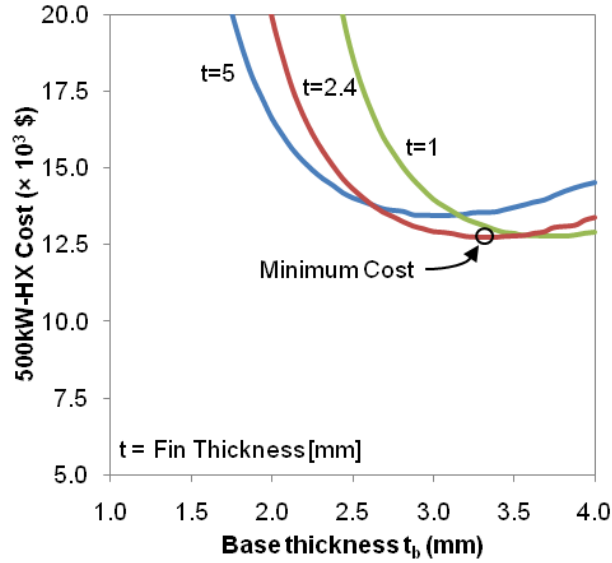


Figure 29 HX Cost along feasible boundary in scenario 2
 $(\phi = 90\%, S = 3 \text{ mm}, L = \{L | 200 \leq L \leq 1000 \text{ and } \phi = 90\%\}, \text{material: } \$44/\text{kg}, \text{assembly: } \$60/\text{hr})$

On the other hand, if the assembly costs are doubled (third scenario), the minimum cost simply shifts upwards and to the right in Figure 30. The base length needs to be increased ($L = 912 \text{ mm}$) to enhance the thermal performance of a single module, thereby reducing the number of plates needed and the number of assembly operations. Again, for longer plates, a thicker base is needed to successfully fill the mold ($t_b = 3.73 \text{ mm}$). In this case, it can be said that the region dominated by assembly costs (to the left of the minimum) is larger, which explains the shift of the minimum cost to the right.

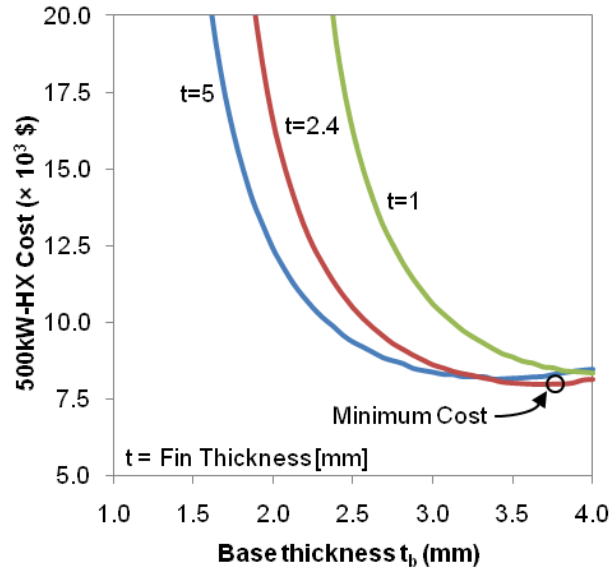


Figure 30 HX Cost along feasible boundary in scenario 3 ($\phi = 90\%$, $S = 3$ mm, $L = \{L | 200 \leq L \leq 1000 \text{ and } \phi = 90\%\}$, material: \$22/kg, assembly: \$120/hr)

3.8 Conclusions

This chapter describes the integration of thermo-fluid considerations, moldability issues, and assembly costs into a single design tool for thermally enhanced polymer heat exchangers, constructed from experimentally validated simulations. The moldability analysis metamodel was integrated into our formulation of the overall heat exchanger cost, which is composed of the molding cost and assembly cost (and pumping power cost is life cycle is considered). These cost components are functions of the heat exchanger design variables. The results show that incorporating molding limitations into the molding cost restricts the choice of optimum designs that minimize the cost, and that distinguishing between feasible and infeasible designs directly affects the choice of heat exchanger parameters. Additionally, the optimum heat exchanger geometry is highly dependent on the values of material price and labor costs because they influence which cost components dominate the design space.

In this work, we have used a simple metamodel for determining moldability. In more recent work [71], a more sophisticated metamodel to explicitly partition the design space into moldable and non-moldable regions was developed. In this new method, a metamodel was generated using the intelligent design of experiment approach that utilizes machine learning techniques to minimize the number of simulations needed to build the model. This new method relies on local interpolation over the stored data. Hence, it requires very few fitting parameters. We do not anticipate the final designs to be different as a result of using the new method. However, the new method is much more scalable and can handle designs requiring multiple gates.

Currently, the design tool is limited by a single choice of geometry. It would be desirable to have at our disposal a variety of complex heat exchanger geometries, which would give the designer freedom to explore more than one possible solution. Also, fiber-filled composites usually have anisotropic thermal conductivity, so more detailed thermal models could account for lateral/longitudinal conduction, and hence more precise estimations of thermal performance.

It should be noted that the work presented in this chapter was published in the Journal of Mechanical Design in 2011 [60].

4 Process Induced Thermal Anisotropy in Polymer Composite Fins

This chapter will provide an overview of an integrated molding-heat transfer modeling methodology used to study the thermal characteristics of polymer composite heat exchange surfaces. Numerical predictions of the fiber orientation in a representative, injection-molded plate fin will be used, via the classic Nielsen model, to determine the anisotropic variation of thermal conductivity in the fin. Thermal simulations will then be performed to determine the effect of the thermal conductivity variations on the performance of the fin. The use of analytical fin equations with an effective thermal conductivity, as a possible replacement for laborious thermal simulations, will also be discussed.

4.1 Fundamentals of fiber orientation in injection moldings

Detailed predictions of fiber orientation in injection-molded parts can be obtained from a variety of software tools. The solution schemes used in these tools are typically based on the work of Advani and Tucker [73], Bay and Tucker [74][75], and most importantly Folgar and Tucker [76], and reflect the observed patterns of preferential fiber orientation created by the flow during mold filling. The decoupling of the flow field from the orientation field, inherent in this approach, and the resulting neglect of the anisotropic viscosity, limits the accuracy of this approach to relatively thin mold cavities, in which the fibers mostly lie in the plane of the cavity and do not affect the friction between the mold surface and the polymer. This solution scheme is incorporated into the injection-molding simulation software, Moldflow [77], used in this study.

Following the work of Advani and Tucker [73] and VerWeyst et al [78], the orientation of a single fiber at a certain position can be expressed by a probability distribution function $\psi(\theta, \phi)$, incorporating dependence on two angles, θ and ϕ . The probability of finding a fiber oriented between the angles θ_1 and $(\theta_1 + d\theta)$, and ϕ_1 and $(\phi_1 + d\phi)$, can be written as

$$P(\theta_1 \leq \theta \leq \theta_1 + d\theta, \phi_1 \leq \phi \leq \phi_1 + d\phi) = \psi(\theta_1, \phi_1) \sin\theta_1 d\theta d\phi \quad (3.1)$$

The distribution function can also be expressed as a function of a unit vector \mathbf{p} with components:

$$p_1 = \sin \theta \cos \phi \quad (3.2)$$

$$p_2 = \sin \theta \sin \phi \quad (3.3)$$

$$p_3 = \cos \theta \quad (3.4)$$

This function is periodic, i.e. $\psi(\mathbf{p}) = \psi(-\mathbf{p})$, and since every fiber must have an orientation, the function meets a normalization condition:

$$\oint \psi(\mathbf{p}) d\mathbf{p} = 1 \quad (3.5)$$

If the fibers are assumed to move with the bulk motion of the fluid, ψ can be regarded as a convected quantity. Then, to describe the change in ψ with time, a continuity condition can be imposed, as

$$\frac{D\psi}{Dt} = - \frac{\partial}{\partial \mathbf{p}} (\psi \dot{\mathbf{p}}) \quad (3.6)$$

While the distribution function ψ is a “complete and unambiguous” expression of fiber orientation, it is hard to manage, and a more compact expression is needed for numerical simulations. Consequently, it is convenient to define orientation tensors by

taking dyadic products of the vector, \mathbf{p} , and integrating said products over all directions. Since ψ is periodic, or even, only the even-order tensors are of interest.

Then, the second- and fourth order orientation tensors are:

$$A_{ij} = \int (p_i p_j) \psi(\mathbf{p}) d\mathbf{p} \quad (3.7)$$

$$A_{ijkl} = \int (p_i p_j p_k p_l) \psi(\mathbf{p}) d\mathbf{p} \quad (3.8)$$

With these definitions in hand, the continuity condition, can be combined with a modified version of Jeffery's equation for dilute suspensions [79], to give

$$\begin{aligned} \frac{\partial A_{ij}}{\partial t} + u_k \frac{\partial A_{ij}}{\partial x_k} = & A_{ik} \Omega_{kj} - \Omega_{ik} A_{kj} + \lambda (A_{ik} E_{kj} + E_{ik} A_{kj} - 2A_{ijkl} E_{kl}) \\ & + 2C_I \dot{\gamma} (\delta_{ij} - 3A_{ij}) \end{aligned} \quad (3.9)$$

where E is the strain rate tensor,

$$E_{ij} = \frac{1}{2} \left(\frac{\partial u_j}{\partial x_i} + \frac{\partial u_i}{\partial x_j} \right) \quad (3.10)$$

Ω is the vorticity tensor,

$$\Omega_{ij} = \frac{1}{2} \left(\frac{\partial u_j}{\partial x_i} - \frac{\partial u_i}{\partial x_j} \right) \quad (3.11)$$

γ is the scalar magnitude of E , while δ_{ij} is the unit tensor.

And λ is a constant that depends on the fiber aspect ratio. In Jeffery's equation, it is equal to

$$\lambda = (r_e^2 - 1)/(r_e^2 + 1) \quad (3.12)$$

with r_e being the equivalent ellipsoidal aspect ratio [76]. So, for slender fibers (large r_e), λ is equal to unity.

It is to be noted that a rotary diffusivity term $C_1\dot{\gamma}$ has been defined to model the effect of fiber interactions. Fiber-to-fiber interactions are said to cause reorientations, and these reorientations are assumed to be “independent, identically distributed random variables with zero mean.” This assumption implies that reorientations do not have any directional bias, and that reorientations occur independently of whether the particles are in nearly random or nearly aligned suspensions. While reorientations may, in fact, depend on the particle distribution, especially in the more concentrated suspensions, this dependence is ignored in this model, so that the diffusivity term is analogous to that of Brownian motion of small particles.

It is further assumed that an interaction occurs whenever the center of a fiber moves within a distance l (fiber length) of a second fiber. Thus, the frequency of interactions is proportional to the strain rate, $\dot{\gamma}$, and the other factors contributing to the strength and rate of interactions are captured by the constant C_1 . As C_1 increases, the steady state fiber distribution becomes broader and more disperse (due to its randomizing effects) [76]. The interaction coefficient, C_1 , may be found by matching numerical predictions to results obtained in experiments involving simple shear flow, or by using a scaled volume fraction expression [80].

Note that the equation of change for the second order tensor A_{ij} , Equation 3.9, has the fourth order tensor A_{ijkl} in it. In fact, the equation of change of any tensor contains the next higher-order even tensor. It is common to approximate the fourth-order tensor in terms of the second-order tensor, using an appropriate closure approximation [81]. Moldflow uses a hybrid closure approximation, which combines linear and quadratic approximations of the orientation tensor. Details of these

approximations were described by Advani and Tucker [73] and are omitted here for brevity.

The fluid dynamics inside the mold can be described by the balance equations for mass, momentum, and energy [78]. The changes of volume with respect to pressure within the injection molding process are not sufficiently high to affect the flow field [67], so the fluid can be considered incompressible. The thermal conductivity of the polymer melt can be anisotropic and depend on the fiber orientation, but this effect is generally neglected in flow simulations [78]. Also, for low Reynolds number flows, or creeping flows, the inertial forces are negligible compared to the viscous forces. If the fluid is assumed to have constant density, specific heat, and conductivity, and body forces are neglected, the momentum and energy equations reduce, respectively, to

$$\frac{\partial u_i}{\partial x_i} = 0 \quad (3.13)$$

$$\rho \left(\frac{\partial u_i}{\partial t} + u_j \frac{\partial u_i}{\partial x_j} \right) = - \frac{\partial P}{\partial x_i} + \frac{\partial \tau_{ji}}{\partial x_j} \quad (3.14)$$

$$\rho c_p \left(\frac{\partial T}{\partial t} + u_i \frac{\partial T}{\partial x_i} \right) = k \frac{\partial}{\partial x_j} \left(\frac{\partial T}{\partial x_j} \right) + \tau_{ij} E_{ij} \quad (3.15)$$

Neglecting the effect of fibers on the stress, a generalized Newtonian fluid formulation can be used to define the stress as

$$\tau_{ij} = 2\eta E_{ij} \quad (3.16)$$

where the viscosity is defined using a Cross-WLF (Williams-Landel-Ferry) model [67],

$$\eta = \frac{\eta_0(T)}{1 + (\eta_0(T)\dot{\gamma}/\tau^*)^{1-n}} \quad (3.17)$$

and the temperature dependence of viscosity is defined as

$$\eta_0 = \eta^* e^{\left[\frac{-c_1(T-T_s)}{c_2+(T-T_s)}\right]} \quad (3.18)$$

In the equations above τ^* , n , η^* , c_1 , c_2 , and T_s are empirical constants.

The Folgar-Tucker [76] model is widely accepted for predicting fiber orientation, and it has been implemented in commercial software such as Moldflow®, the most popular injection molding software [77]. In Moldflow®, an extra term is added to the Folgar-Tucker model called a “thickness moment of interaction coefficient” D_z [80]. This term serves to tune the magnitude of the randomizing effect of out-of-plane interactions. So when $D_z=1$, the equation is simply the Folgar-Tucker model for 3D problems, while when $D_z=0$, the equation becomes the Folgar-Tucker model for 2D problems. However, the fundamental physics of the Folgar-Tucker model remain unchanged.

As noted above, Moldflow can be used to determine not only the flow patterns but also the statistical probability distribution of fiber orientation for polymer composites, anywhere in the molded space [80], using a moving flow front, or volume of fluid (VOF), method. The fiber orientation can then be used to determine the local thermal anisotropy of the molded structure, providing the capability for a more refined thermal analysis of polymer composite heat exchanger surfaces.

4.2 The Nielsen Model

The original model for the effective thermal conductivity of a composite polymer was proposed by Nielsen [41]. The validity of this model has been confirmed by numerous studies [82][83], for mixtures with modest filler concentrations [84], and is given as:

$$\frac{k}{k_m} = \frac{1 + AB\phi_f}{1 - B\phi_f} \quad (3.19)$$

$$A = k_E - 1 \quad (3.20)$$

$$B = \frac{k_f/k_m - 1}{k_f/k_m + A} \quad (3.21)$$

$$\phi = 1 + \left(\frac{1 - \phi_{\max}}{\phi_{\max}^2} \right) \phi_f \quad (3.22)$$

where ‘k’, ‘k_m’, and ‘k_f’ are the composite, polymer resin, and filler thermal conductivity, respectively, and ‘k_E’ is the Einstein coefficient (a function of aspect ratio and orientation of the fibers), ϕ_f is the filler volume fraction, and ϕ_{\max} is the maximum packing fraction. The Einstein coefficient, also known as the intrinsic viscosity, can be determined exactly for dispersed spheres and can usually be accurately estimated for particles with other geometries [85]. Elongated ellipsoids or rod-like particles will increase the Einstein coefficient [86]. Nielsen gives typical “A” values for various fillers, including an upper-bound value for uniaxially-oriented fibers equal to twice the aspect ratio, 2L/D, and an “A” value of 0.5 for heat flow across the fibers.

Fiber volume fractions for commercially available, thermally conductive polymers have been experimentally determined to reach as high as 70% [87]. The dependence of the composite thermal conductivity on carbon fiber volume, for a packing fraction

of 0.82, is shown in Figure 31. The figure shows the thermal conductivity in the direction parallel ($A = 2L/D$) and perpendicular ($A = 0.5$) to uniaxially oriented fibers. Examining this figure, it may be seen that with varying filler volume, the thermal conductivity of the polymer-composite, in the favorable direction, can vary from values just marginally above that of the pure polymer to values in the range of titanium (20 W/m·K) with concentrations of 0.6 and reach values as high as 40 W/m·K –comparable to Cu-Ni alloys– at a concentration close to 0.7. These high conductivities are achieved at the expense of very low values normal to the fiber direction, falling to just 1/80th of the in-line values and leading to strong thermal anisotropy in the molded parts.

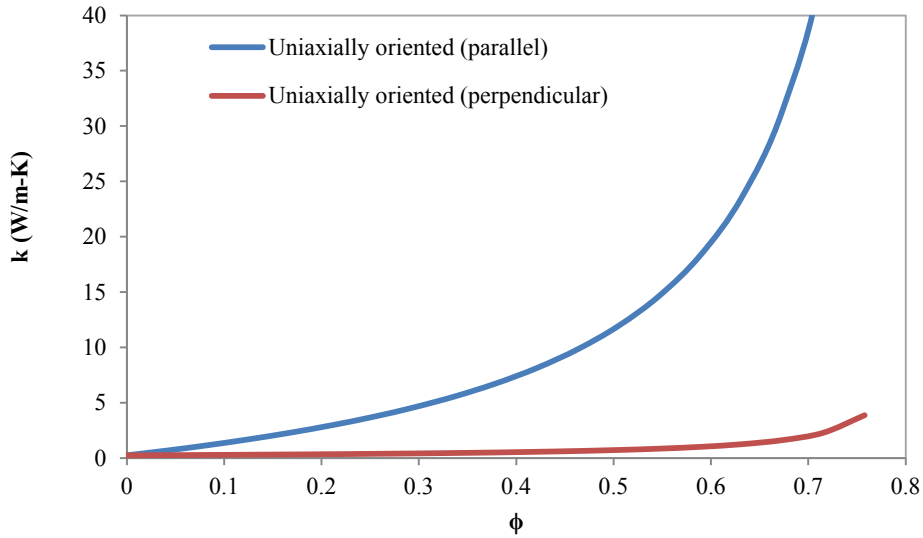


Figure 31 Composite conductivity as a function of filler volume fraction ($k_f = 590$ W/m·K, $k_m = 0.25$ W/m·K, $\phi_{max} = 0.82$, $L/D = 20$)

4.3 Thermal conductivity calculated from orientation tensors

For a second-order thermal conductivity tensor κ , its orientation average is defined as

$$\langle \kappa \rangle \equiv \oint \kappa(\mathbf{p}) \psi(\mathbf{p}) d\mathbf{p} \quad (3.23)$$

If we consider κ to be transversely isotropic, the tensor must have the form

$$\kappa_{ij}(\mathbf{p}) = A_1 p_i p_j + A_2 \delta_{ij} \quad (3.24)$$

where A_1 and A_2 are scalar constants. Taking the orientation average yields

$$\langle \kappa \rangle_{ij} = A_1 \langle p_i p_j \rangle + A_2 \langle \delta_{ij} \rangle \quad (3.25)$$

which simplifies to

$$\langle \kappa \rangle_{ij} = A_1 a_{ij} + A_2 \delta_{ij} \quad (3.26)$$

This result means that the orientation average of the second-order thermal conductivity tensor is “completely determined by the second-order orientation tensor, and by the underlying unidirectional property tensor [73].”

Let us define an arbitrary transversely isotropic thermal conductivity tensor as

$$\boldsymbol{\kappa} = \begin{bmatrix} k_{xx} & 0 & 0 \\ 0 & k_{yy} & 0 \\ 0 & 0 & k_{zz} \end{bmatrix} \quad (3.27)$$

with the x-axis as its axis of symmetry, so that

$$\mathbf{p} = (1,0,0) \quad (3.28)$$

Following Equation 3.24 we can say that

$$k_{xx} = A_1(1)(1) + A_2(1) \quad (3.29)$$

$$k_{yy} = A_1(0)(0) + A_2(1) \quad (3.30)$$

Solving for A_1 and A_2 gives

$$A_2 = k_{yy} \quad (3.31)$$

$$A_1 = k_{xx} - k_{yy} \quad (3.32)$$

Since $\boldsymbol{\kappa}$ is transversely isotropic tensor with an x-axis of symmetry, k_{xx} corresponds to the thermal conductivity in the direction of alignment, and $k_{yy}=k_{zz}$ correspond to the thermal conductivity in the direction transverse to the axis of alignment. We can generalize Equations 3.31 and 3.32 as

$$A_2 = k_{\perp} \quad (3.33)$$

$$A_1 = k_{\parallel} - k_{\perp} \quad (3.34)$$

Finally, Equation 3.26 becomes

$$\langle \kappa \rangle_{ij} = (k_{\parallel} - k_{\perp})a_{ij} + k_{\perp} \delta_{ij} \quad (3.35)$$

4.4 Numerical Prediction of 3D Fiber Orientation

4.4.1 Simulation Space and Parameters:

The geometry chosen for this numerical study of anisotropy is an injection molded finned plate, 26 mm long by 50 mm-wide with integral longitudinal, rectangular fins of different heights and thicknesses, as shown in Figure 32 and described in Table 11. Special attention is paid to the first four fin geometries, since their behavior summarize the overall trends found in this study. In the simulations performed, the thickness of the fins and of the plate was kept equal, so as to follow common “Design for Manufacturing” guidelines [68] and it is assumed that a homogenous mixture of polymer and carbon fibers is injected through a gate located in the center of the plate. The molding simulations were done with Moldflow Plastics Insight 6.1 (MPI) [77]. The polymer used in this study is PolyOne’s NJ-6000 TC, which consists of a pitch-derived carbon fiber filler, with a thermal conductivity of 590 W/m·K, a density of 2.1 g/cm³, and fiber diameter of 10 μm with an average fiber aspect ratio of 20 [88], dispersed in a Nylon 12 polymer matrix, with a conductivity of 0.25 W/m·K and density of 1.14 g/cm³ [89]. Based on the manufacturer’s specification for this commercially available composite, the fiber weight percentage was 51.8% and the fiber volume fraction 0.33 [90]. The filling simulation was performed for a maximum

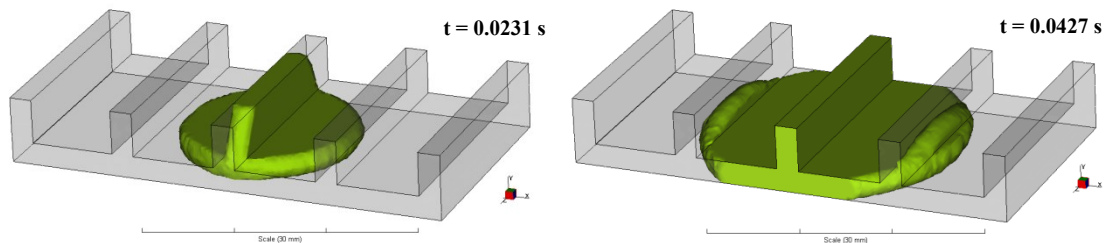
injection pressure of 180 MPa, a melt temperature of 270°C, and a mold temperature of 35°C.

Table 11 Modeled Fin Geometries
(Plate width = 50 mm, length = 26 mm, no. of fins = 5)

Geometry #	Fin height, b (mm)	Fin thickness, δ (mm)
1	5	2.5
2	10	2.5
3	5	1.5
4	5	3.5
5	10	3.5
6	10	1.5
7	5	2
8	10	2
9	5	3
10	10	3
11	12	3

4.4.2 Filling Pattern

Figure 32 shows the Moldflow-simulated flow front, as it advances through the mold cavity from the gate placed at the center of the plate (Geometry #1). The polymer-fiber mixture can be seen to initially flow radially outward from the gate, taking just 0.0427 second to fill the fin directly over the gate and to reach the base of the adjacent fins. A more complex flow pattern follows, with the tips of the outermost fins filling last and some 0.1034s being needed to completely fill the mold, for the stated conditions.



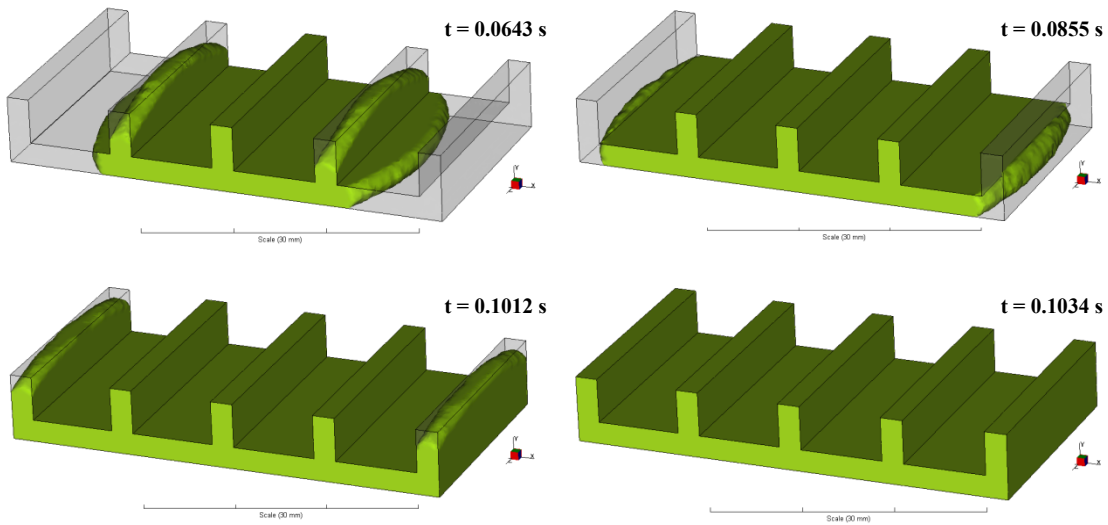


Figure 32 Flow front movement during filling of finned plate (melt temperature 270 °C, mold temperature 80 °C –uniform, no cooling channels defined-, maximum injection pressure 180 MPa, cooling time 20 sec, interaction coefficient C_1 0.0132)

4.4.3 Fiber Orientation

The computed fiber orientations were examined for mesh sensitivity. For 3D geometries, such as a finned-plate, a fine mesh is needed to capture the large accelerations and consequent variations in the velocity profile, as the melt turns from the base plate into the fin. The global edge length is a measure of the average element size and is the input parameter that Moldflow® uses to generate the mesh. As the number of elements increases, the computation time increases significantly. At an edge length of 1 mm, the simulation time was 41 minutes; while for an edge length of 0.5 mm, the computational time increased to 3 hours. For an edge length of 0.4 mm, the simulation time was close to six hours. The tensor values for an edge length of 0.5 mm were found to be within 4% of the 4 mm-edge-length values. Given the small differences between edge lengths of 0.5 and 0.4 mm, and because of the computational demands of small mesh elements, no further refinement was sought.

To explore the extent of thermal anisotropy typically generated by fiber orientation variations, it is instructive to examine a cross section (shown in Figure 33) in the molded finned plate. To quantify the anisotropy, the degree of alignment in the x, y, and z directions must be examined. The diagonal components of the orientation tensor; A_{xx} , A_{yy} , and A_{zz} [78], give the statistical fraction of fibers being aligned in each direction.

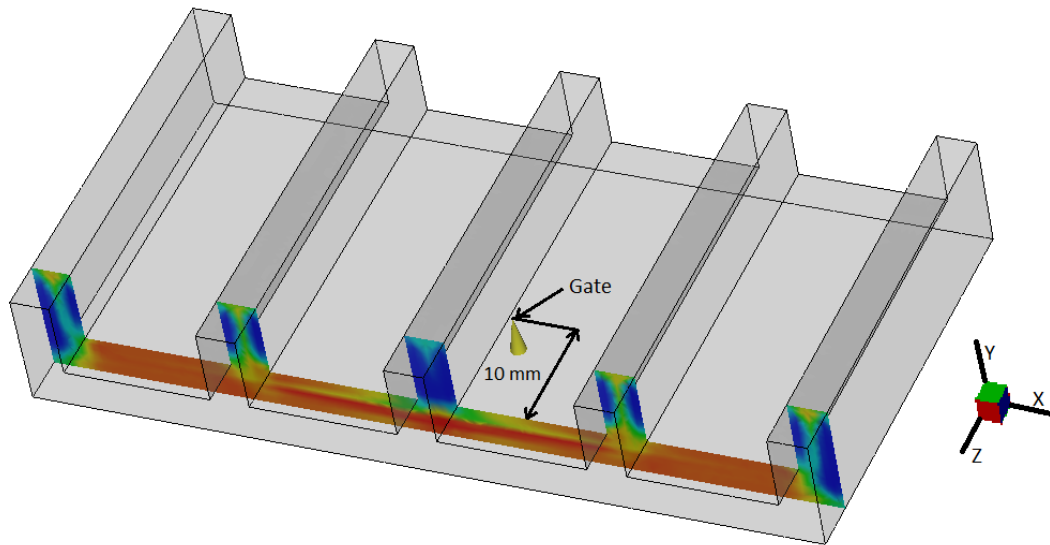
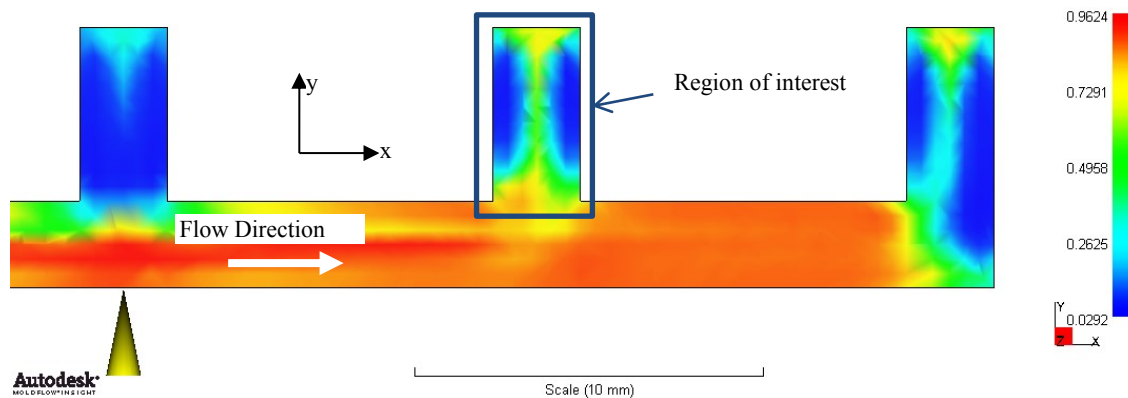


Figure 33 Simulated finned plate geometry showing location of cross-section

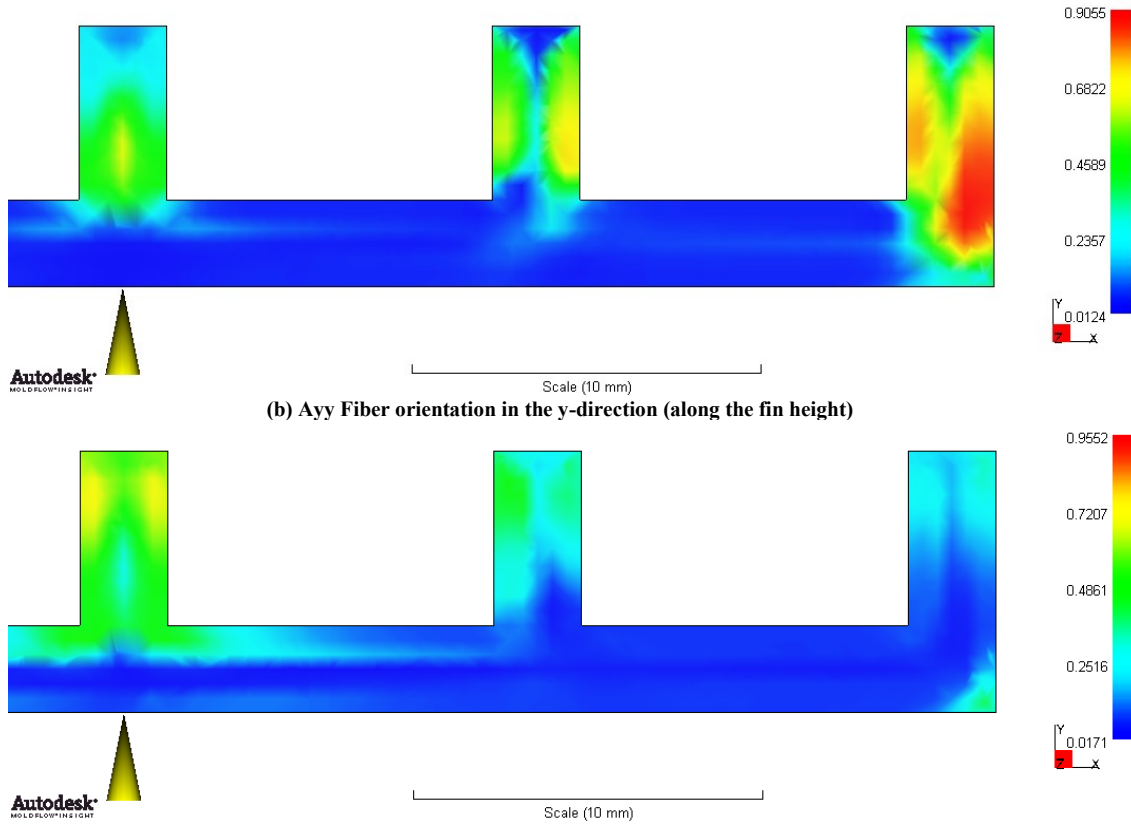
The results displayed in Figure 34 correspond to geometry #1 (see Table 11), and they show that for the location of interest, in the plate supporting the fins, the fibers are highly aligned in the x-direction (Figure 34a), with tensor values of 0.8 to 0.9. As the polymer turns upward to fill the fin, some of the fibers start re-aligning in the vertical direction (Figure 34b) causing the x-direction alignment to decrease to 0.50-0.75 at the base of the fin. Going from the fin base to the mid-height of the fin, a common pattern of shell-core-shell can be observed, where at the outer, or shell, layer, the orientation is mostly parallel to the vertical walls, with tensor values

ranging from 0.5 to 0.75, while tensors for the alignment perpendicular to the wall are less than 0.25. Away from the walls, in the thin core, the fibers are well mixed yielding nearly-equal probabilities of vertical (0.4) and horizontal (0.5) orientation. At the fin tip, where the flow must accommodate to the presence of the “cap”, fiber orientation changes again to roughly 50% in the horizontal direction and 25% in the vertical direction.

Figure 34c reveals that fiber alignment in the z-direction (normal to the plane of the cross section) is relatively low, ranging from 0 to 0.25 and reaching 0.30 only at the tip of the fin. Note that the non-zero values of the z-direction tensors reflect the fact the flow is moving radially outward from the gate. Due to the modest variations in fin temperature and heat transfer along the length of the fins the heat transfer analysis that follows addresses only two-dimensional conduction in the indicated fin.



(a) Axx Fiber orientation in the x-direction (across the fin thickness)



(b) Ayy Fiber orientation in the y-direction (along the fin height)
 (c) Azz Fiber orientation in the z-direction (normal to the plane of the cross-section)
 Figure 34 Predicted fiber orientation tensor plots
 (Geometry #1 $\delta=2.5\text{mm}$, $b=5\text{mm}$, note: the yellow cone under the plate indicates the location of the gate)

4.4.4 Thermal Conductivity

The observed complex variation in fiber alignment in the x-y plane of the central fin can be expected to lead to comparable variations in the thermal conductivity in the fin and its “footprint” on the base plate. Moreover, the low probability for vertical, y-direction, fiber orientation near the fin base impedes the effectiveness of heat transfer from the base plate to the fin, as well as directly from the fin base to the surrounding fluid.

Using Equations 3.19-3.22 and 3.35, a two-dimensional anisotropic conductivity map, shown in Figure 35, was generated for the 5 mm high, 2.5 mm thick fin highlighted in Figure 34a, using an almost identical spatial discretization to that used in the melt flow simulation. In a previous publication [91], a sample of only 15 zones was used

to generate an approximate map of thermal conductivity. However, the heat transfer rate was under-predicted by almost 20% compared to a map with nearly 200 zones. Thus, the latter map is used here to more accurately reflect the behavior of an anisotropic fin. Figure 35 displays significant local variations in the thermal conductivities showing the largest values in the x-direction at the base and top of the fin, reaching 7 W/m·K, and the lowest values reaching only 1 W/m·K close to the fin vertical walls. Alternatively, the largest values in the y-direction, again reaching almost 7 W/m·K, are found along the sides of the fin, or vertical walls, while the lowest values, of approximately 1 W/m·K, are found on the top and bottom of the fin. The conductivity values in the z-direction fall within a smaller range, between 1 and 4.5 W/m·K, throughout the cross-section of the fin. This behavior is directly related to the filling trends seen in Figure 32, where the regions of the fin closer to the gate are filled first which creates a z-direction flow pattern away from the gate. Figure 36 shows thermal conductivity maps of a fin with twice the height and an identical thickness (Geometry #2: $\delta=2.5\text{mm}$, $b=10\text{mm}$). The trends observed in the taller fin are similar to those in Figure 35, except that the longer melt flow path, the highly-aligned “mid-height” section, where the polymer melt flows mostly in the y-direction, occupies a much larger fraction of the fin height, results in a larger section of high of y-direction thermal conductivity and strong anisotropy between the y- and x-directions. Strong anisotropy, but with a reversed relationship, occurs in the narrow core region, where in x direction conductivity is high and the y-direction conductivity low. When the melt reaches the top of the fin, it is forced to change flow directions (x

and z directions), and high x- and z-conductivities are achieved. Similar behaviors were observed for the other two geometries studied here.

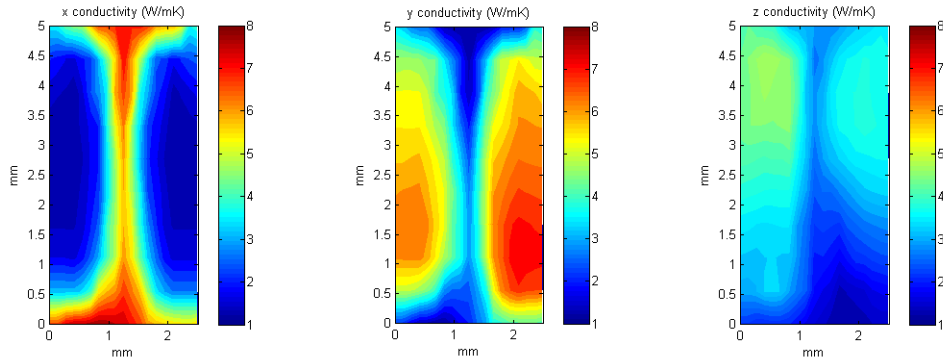


Figure 35 Predicted thermal conductivity values along the x, y, and z directions of fin #1 (Geometry #1: $\delta=2.5\text{mm}$, $b=5\text{mm}$)

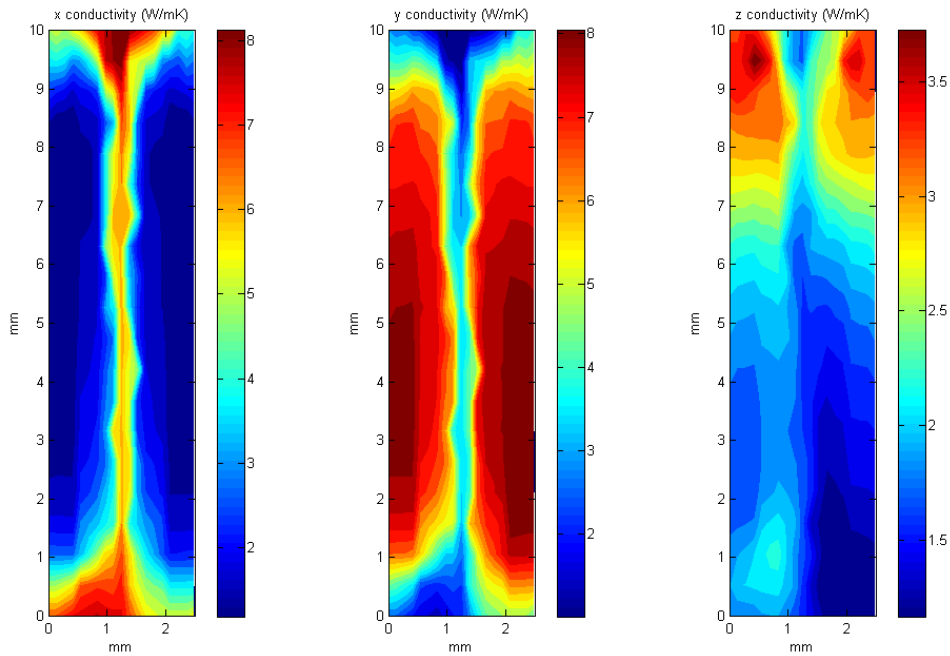


Figure 36 Predicted thermal conductivity values along the x, y, and z directions of fin #2 (Geometry #2: $\delta=2.5\text{mm}$, $b=10\text{mm}$)

4.5 Heat Transfer from Anisotropic Plate Fin

4.5.1 Gas-Liquid Polymer Heat Exchanger

The potential impact of anisotropy on the heat transfer characteristics of an individual fin, with local anisotropy variations, as shown in Figure 35 and Figure 36, are studied

by reference to the thermal performance of gas-side heat exchange surfaces in a gas-liquid polymer heat exchanger used to cool methane in an LNG liquefaction plant [70]. Simulations were conducted using ANSYS software, with a mesh size of 0.1 mm and a convection boundary condition at the sides of the fin, varying from 50 to 1000 W/m²K. While the gas-side heat transfer coefficient for low pressure methane can be expected to equal approximately 50 W/m²K, in the high pressure segments of the liquefaction heat exchange “train” the heat transfer coefficient can reach values of 200-300 W/m²K and increase to 1000 W/m²K or higher, when condensation is present.

4.5.2 Local Anisotropy

Figure 37 provides an opportunity to examine the effects of local anisotropy in 2D rectangular fins for the first four different geometries shown in Table 11, and possessing anisotropic thermal conductivity variations such as those shown in Figure 35 and Figure 36. The fins operate with a base excess temperature of 55 K, while cooled by a heat transfer coefficient of 1000 W/m²K. As expected, fins with low aspect ratio (thicker or shorter) are more efficient and thus hotter. This is why fins #1 and #4 are on average hotter than fins #2 and #3. Examining Figure 37 more closely, the temperature profiles have a strong two-dimensional character, reflecting the effect of the relatively low thermal conductivity of the polymer composite and its impact on the fin Biot Number, and the non-uniformity of the thermal anisotropy does appear to skew the lateral temperature distributions in the fins, leading to a thru-thickness temperature variation of approximately 5-7 K. The profiles follow the asymmetry of the thermal conductivity maps seen in Figure 35 and Figure 36, and the right side of

the fin is slightly hotter than the left side. As was discussed previously, this is caused by the direction of the melt flow coming from left to right, which causes the y-conductivity on the right side to be higher, especially at the bottom and mid-height of the fin. Note that the asymmetric behavior is more noticeable in fins with low aspect ratio (#1 and #4). Compare, for example, the left and right sides of the y-conductivity map of fin #1 in Figure 35. The right side has, on average, a higher thermal conductivity than the left. However, the y-conductivity map of fin #2 in Figure 36 shows that the differences between sides are less noticeable, except at the bottom of the fin. In general, in thicker or shorter fins (with low aspect ratio) the aligning effect of the vertical walls is weaker than in thinner or taller fins, and thus the orientation/conductivity maps are more asymmetric.

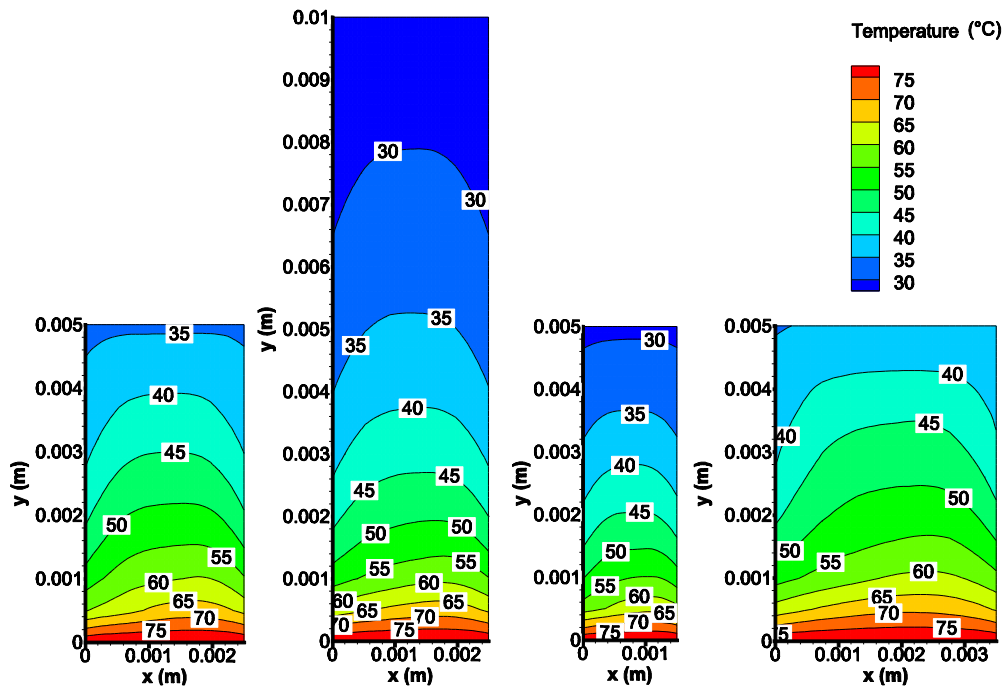


Figure 37 Temperature profiles for anisotropic fins of various geometries high h ($h=1000 \text{ W/m}^2\text{K}$, $\theta_v=55\text{K}$, $t_{\text{amb}}=25^\circ\text{C}$)

At low heat transfer coefficients ($50 \text{ W/m}^2\text{K}$), the fins are more efficient and thus the temperature gradient in the y-direction is lower. This can be seen in Figure 38 where the fins are, on average, much hotter than the fins in Figure 37. As a result, the through-thickness temperature variation is milder (only 1-2 K); although the asymmetric behavior persists, especially in the bottom regions of the fins, where the differences in process-induced properties are more pronounced.

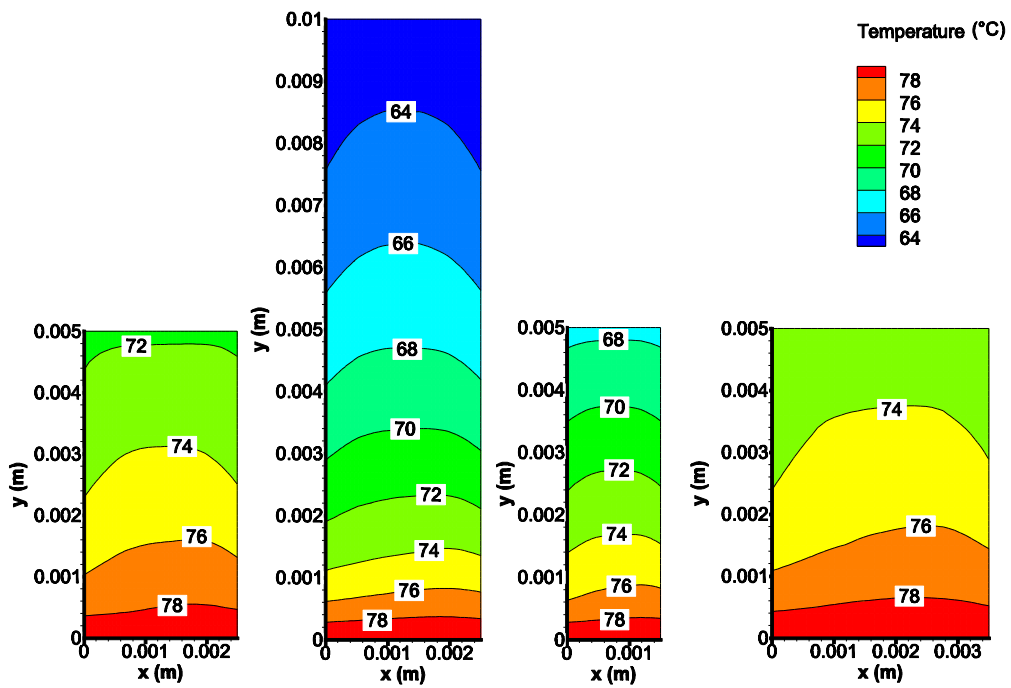


Figure 38 Temperature profiles for anisotropic fins of various geometries low h ($h=50 \text{ W/m}^2\text{K}$, $\theta_b=55\text{K}$, $t_{amb}=25^\circ\text{C}$)

The fin heat transfer rate as a function of heat transfer coefficient is shown in Figure 39 for the first four fin geometries studied here. As the heat transfer coefficient increases, the heat transfer rate through the fin base increases due to a diminishing convective resistance. The rate of increase, or the slope in Figure 39, decreases as the convective resistance vanishes and conduction inside the fin starts to prevail in the overall heat rate. Even though there are differences in the thermal conductivity maps

between fins, examining only the geometrical differences can help to explain the differences in heat transfer rate. Fin #3 gives the lowest heat transfer rate of all four geometries considered, since the fin has very little area and the lowest efficiency of all geometries. If the thickness is doubled, as in fin #1, the efficiency and the heat transfer rate increase. The same effect is repeated if the thickness is increased further, as seen for fin #4. If the fin height is increased, as was done for fin #2, the fin area increases as well; however, the fin efficiency decreases, relative to fin #1. Thus, even though thermal conductivity maps are not equal for different geometries, changes in heat transfer rate as a function of fin thickness and fin height can be predicted qualitatively by standard fin equations. In the next section, quantitative predictions of heat transfer rates, using standard fin equations, are explored.

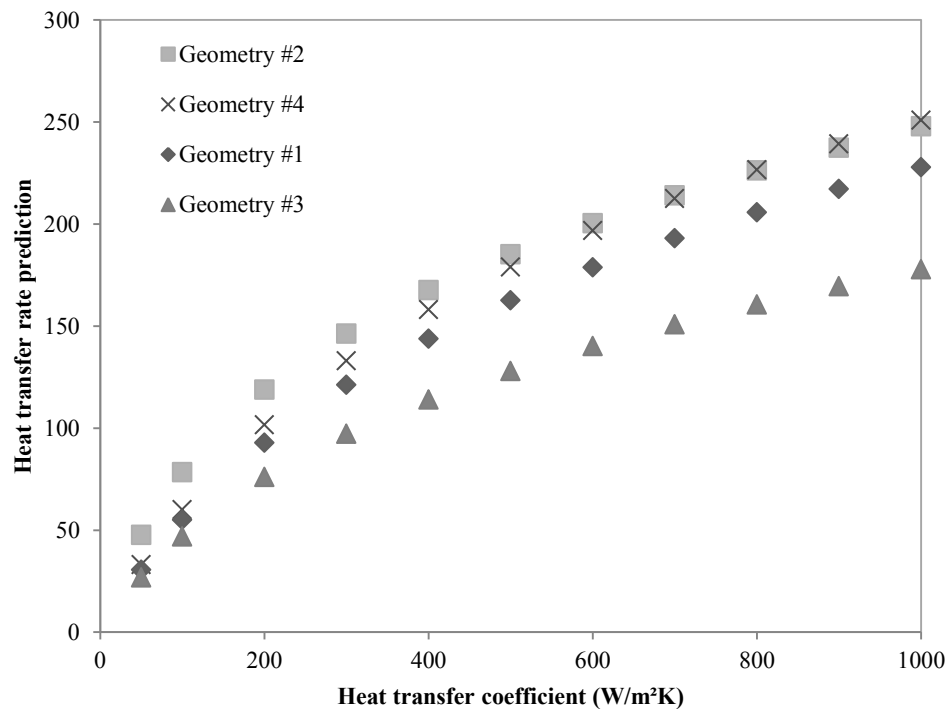


Figure 39 Anisotropic fin heat loss as a function of heat transfer coefficient and fin geometry ($\theta_b=55\text{K}$, $T_{\text{amb}}=25^\circ\text{C}$, for fin geometry see Table 11)

4.5.3 Effective Thermal Conductivity

The availability of an effective thermal conductivity for use in predicting the behavior of anisotropic composite fins, using the standard fin equations, would be of considerable benefit in the design of composite heat exchangers. Bahadur and Bar-Cohen [92] studied the effects of a “globally-orthotropic” thermal conductivity in a composite pin fin. They determined that in systems with low heat transfer coefficients ($<70 \text{ W/m}^2\text{K}$), when the thermal resistance in the fluid dominates the heat dissipation rate, approximating the heat rate using the axial thermal conductivity in a one-dimensional fin equation provides good accuracy. More specifically, for Biot numbers below 0.4, one-dimensional classical solutions for cylindrical pin fins provide heat transfer rates within 5% of the full orthotropic solutions. When the Biot number is higher than 0.4, the discrepancies in heat transfer rate increase significantly.

4.5.3.1 One-dimensional fin

In the case of a locally varying anisotropic fin, approximations of the heat rate using an effective conductivity are more complicated. We may start by treating the anisotropic fin as a one-dimensional fin. The heat transfer rate for a rectangular fin with convection on the tip and sides takes the familiar form:

$$q = M \frac{\sinh mb + (h/mk) \cosh mb}{\cosh mb + (h/mk) \sinh mb} \quad (3.36)$$

where $M \equiv \sqrt{hPkA_c}(T_b - T_\infty)$ and $m^2 \equiv hP/kA_c$.

Using Equation 36 requires that a single effective conductivity be used to represent the maps of x- and y-conductivity of the anisotropic fins. If the fin is assumed to be one-dimensional then the y-conductivities should dominate the heat transfer rate, so

only the y-conductivity map is considered in extracting an effective conductivity.

Note that an average conductivity can be obtained in many different ways, and in this work we have tried several definitions of means: arithmetic, harmonic, and geometric

$$k_{arithmetic} = \frac{1}{n} \sum_{i=1}^n k_i \quad (3.37)$$

$$k_{harmonic} = \frac{n}{\sum_{i=1}^n \frac{1}{k_i}} \quad (3.38)$$

$$k_{geometric} = \sqrt[n]{k_1 k_2 \cdots k_n} \quad (3.39)$$

4.5.3.2 Orthotropic fin

As an alternative to the one-dimension approximation, the anisotropic fin may also be represented as a “globally- orthotropic” fin. Following methodology described by Bahadur and Bar-Cohen [92], the fin heat transfer rate per unit depth of a two-dimensional orthotropic longitudinal fin with constant k_x and k_y can be found to be,

$$q = 4k_y(T_b - T_\infty) \sum_{n=1}^{\infty} \left\{ \frac{\sqrt{k^*} \sin^2 \lambda_n}{\lambda_n + \sin \lambda_n \cos \lambda_n} \right\} \left\{ \frac{Bi_y \cosh \lambda_n \sqrt{k^*} K + \lambda_n \sqrt{k^*} K \sinh \lambda_n \sqrt{k^*} K}{Bi_y \sinh \lambda_n \sqrt{k^*} K + \lambda_n \sqrt{k^*} K \cosh \lambda_n \sqrt{k^*} K} \right\} \quad (3.40)$$

for a fin exposed to convection on the sides and the tip, where

$$Bi_x = \frac{h\delta}{2k_x} \quad (3.41)$$

$$Bi_y = \frac{hb}{k_y} \quad (3.42)$$

$$k^* = \frac{k_x}{k_y} \quad (3.43)$$

$$K = \frac{2b}{\delta} \quad (3.44)$$

The eigenvalues λ_n are defined with:

$$\lambda_n \tan \lambda_n = Bi_x \quad (3.45)$$

Since Equation 3.40 assumes constant k_x and k_y , the entire map of x- and y-thermal conductivities must be represented by effective, directional values.

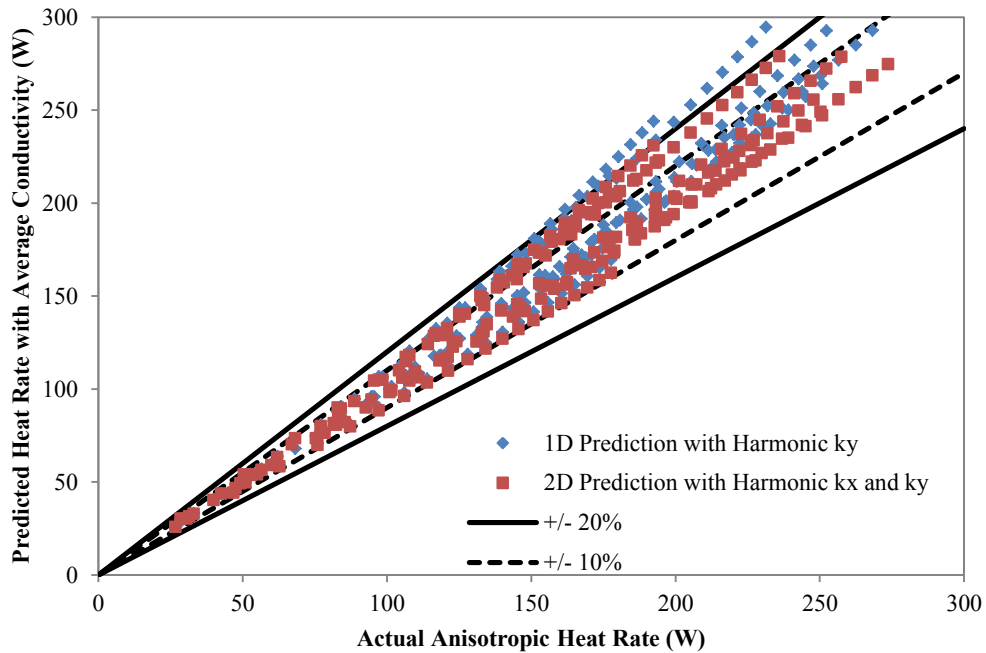


Figure 40 Predicted heat transfer rate using effective thermal conductivities vs. actual anisotropic heat rate

Comparing the different definitions of mean thermal conductivity, the harmonic mean appears to predict the heat transfer rate more accurately than the other means using the equations defined in section 4.5.3.1 and section 4.5.3.2 for a one-dimensional fin and for a globally-orthotropic fin, respectively. Figure 40 above shows the heat transfer rate predicted by the harmonic means for all 11 fin dimensions in Table 11, compared to the actual heat transfer rate of the anisotropic fins. At low heat transfer rates, i.e.

low heat transfer coefficients ($< 300 \text{ W/m}^2\text{K}$), the predictions of both 1D and 2D models give very good results ($< \sim 10\%$ error). As the heat transfer coefficient increases, the relative effect of conduction inside the fin starts dominating the heat transfer rate and so the error of using approximate values increases.

Table 12 Summary of model discrepancy for anisotropic fins

Fin #	Thickness (mm)	Height (mm)	Aspect Ratio	Maximum error 1D	Maximum error 2D
1	2.5	5	4.0	4%	3%
2	2.5	10	8.0	10%	3%
3	1.5	5	6.7	8%	9%
4	3.5	5	2.9	5%	3%
5	3.5	10	5.7	10%	4%
6	1.5	10	13.3	21%	16%
7	2	5	5.0	7%	2%
8	2	10	10.0	27%	20%
9	3	5	3.3	9%	3%
10	3	10	6.7	17%	8%
11	3	12	8.0	28%	18%

Table 12 above summarizes the relative errors of using 1D and 2D models to represent the anisotropic fins studied here. In general, Table 12 shows that using a 2D model reduces the maximum heat transfer rate relative error. Note that for fins with high aspect ratio, the error is usually higher. For example, for fins #6, #8, and #11 both 1D and 2D models over-predict the heat transfer rate. The high relative errors observed for these fins could be explained by the relative effect of the low y -conductivity region observed in section 4.4.4, and shown in Figure 35 and Figure 36. As was said before, this region impedes heat transfer at the base of the fin, and naturally this problem is exacerbated for high aspect ratio fins, in which an effective thermal conductivity does not capture the behavior at the base appropriately.

4.6 Conclusions

The thermal behavior of an injection-molded fin subjected to convective heat transfer was studied. Injection molding simulations of a finned-plate were followed by fiber orientation predictions using the Folgar-Tucker model embedded in Moldflow®, especially suited to the behavior of very thin mold cavities. Based on the predicted orientation tensors, anisotropic thermal conductivity values were calculated using the Nielsen's model. Thermal simulations, using finite-element software, for local anisotropy were then performed to assess the heat transfer rate and temperature distribution of anisotropic Nylon 12 plate fins, with 33% volumetric concentration of carbon fibers.

The results obtained in the numerical simulation of local anisotropy display the effect of the relatively low thermal conductivity of the polymer composite, yielding significant through thickness temperature variations and poorer thermal dissipation due to cooler exposed fin surfaces. Moreover, the lateral temperature distribution of the fin appears to be skewed due to the difference in flow-induced orientation (and conductivity) in the fin. Finally, the use of an effective conductivity to represent the anisotropic fin was explored. It was found that using harmonic means either in one-dimensional or two-dimensional models gives very good predictions of the heat transfer rate. For heat transfer coefficients below $300 \text{ W/m}^2\text{K}$, the relative errors in the heat transfer rate are below 10%. It was also found that using a 2D model reduces the maximum heat transfer rate relative error when compared to a 1D model prediction. Finally, the effect of the process-induced low-k region at the fin base is exacerbated for high-aspect ratio fins. As a result, effective conductivity models fail

to capture this behavior, and tend to over-predict the heat transfer rate of high-aspect ratio fins.

5 A Novel Polymer Heat Exchanger

This chapter presents an in-depth study of the thermal performance of a gas-to-liquid webbed tube heat exchanger (WTHX). The heat exchanger in this study is made with raw polymers, as well as with a thermally enhanced polymer composite which consists of a polymer matrix embedded with carbon fibers. This WTHX is shown to provide an equivalent thermal performance to a plate-fin heat exchanger, while providing significant mass savings. The natural orientation of fibers during the injection molding process is expected to provide higher strength with improved thermal performance. Laboratory-scale prototype heat exchangers were built using injection molding and fused deposition modeling, and were tested in a cross flow air-to-water test facility. The performance is studied using analytical equations and semi-empirical correlations, aided by the use of numerical simulations, and verified through experiments. An effective thermal conductivity was deduced by comparing experimental results to analytical and numerical results.

5.1 Webbed-Tube Heat Exchanger

A webbed-tube heat exchanger consists of a stack of thin rectangular flat plates that are separated from each other in the thickness direction to allow one of the fluids (preferably a gas) to flow between the plates. Embedded in the plates is an array of tubular channels that can span the length of the plate. This tubular array serves as the passage for the second fluid (preferably a liquid). In practice, the diameter of the tubes can be substantially larger than the thickness of the plate itself, effectively creating a “bumpy” plate or a webbed-tube configuration, or WTHX, as shown in

Figure 41. The effects of these bumps will be discussed in later sections of this chapter. While the WTHX design, material, and application are quite novel, the geometry itself is really a variation of a heat exchanger shown in the work of Abdelaziz and Radermacher [93].

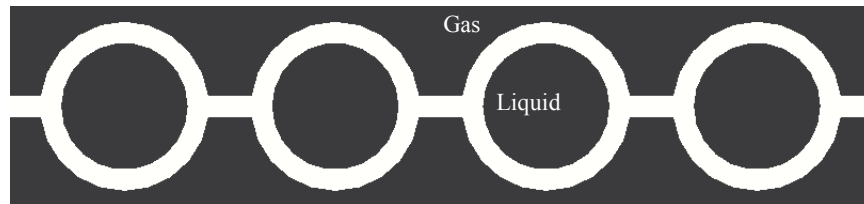


Figure 41 Profile view of Webbed-Tube heat exchanger plate

The gas can flow in a direction parallel or perpendicular to the liquid. When the flows are parallel to each other, the heat exchanger is said to provide a co-current (in the same direction of the liquid) or countercurrent (opposite direction) configuration. When the flows are perpendicular, the heat exchanger is said to offer a cross-flow configuration. Contiguous tube plates can be fully aligned or displaced in the lateral direction, relative to each other, so as to create staggered arrays of tubes (see Figure 42).

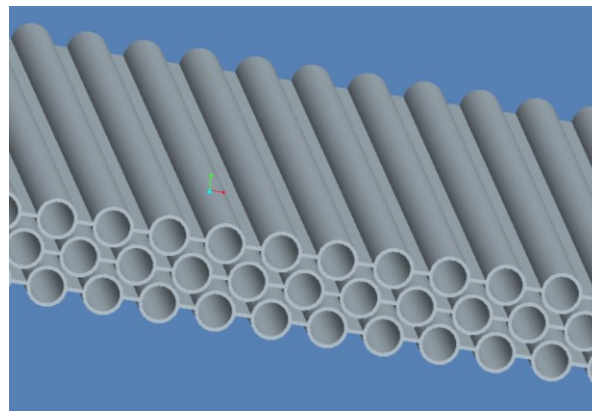


Figure 42 3D rendition of the WTHX geometry

5.2 Webbed-Tube Heat Exchanger Prototypes

Several prototypes of a webbed-tube heat exchanger were built with the purpose of testing its thermal performance in an air-to-water facility.

5.2.1 Injection-molded webbed tube array

The building block of the heat exchanger is a webbed-tube array. The arrays were made by injection molding of PolyOne's NJ-6000 TC, which consists of a pitch-derived carbon fiber filler, with a thermal conductivity of $590 \text{ W/m}\cdot\text{K}$, a density of 2.1 g/cm^3 , and fiber diameter of $10 \text{ }\mu\text{m}$ with an average fiber aspect ratio of 20 [88], dispersed in a Nylon 12 polymer matrix, with a conductivity of $0.25 \text{ W/m}\cdot\text{K}$ and density of 1.14 g/cm^3 [89]. Based on the manufacturer's specification for this commercially available composite, the fiber weight percentage was 51.8% and the fiber volume fraction 0.33 [90].

The dimensions of the molds were designed to fit a small injection machine, Babyplast, which is available at the Advanced Manufacturing Laboratory at the University of Maryland [94]. Using Autodesk Moldflow to simulate the injection molding process [77], and considering the maximum shot size (6.5 cc) and injection pressure (183 MPa) of the injection machine, appropriate wall thickness, size and number of tubes, and tube length were chosen. The resulting mold design is shown below in Figure 43. The mold was made with aluminum, and it was milled using CNC machining. Note that the overall dimensions are limited by the size of the mold piece itself and the real estate available once the through holes for holding screws are drilled. Additionally, the walls must be sufficiently thick to allow for the mold to be filled completely.

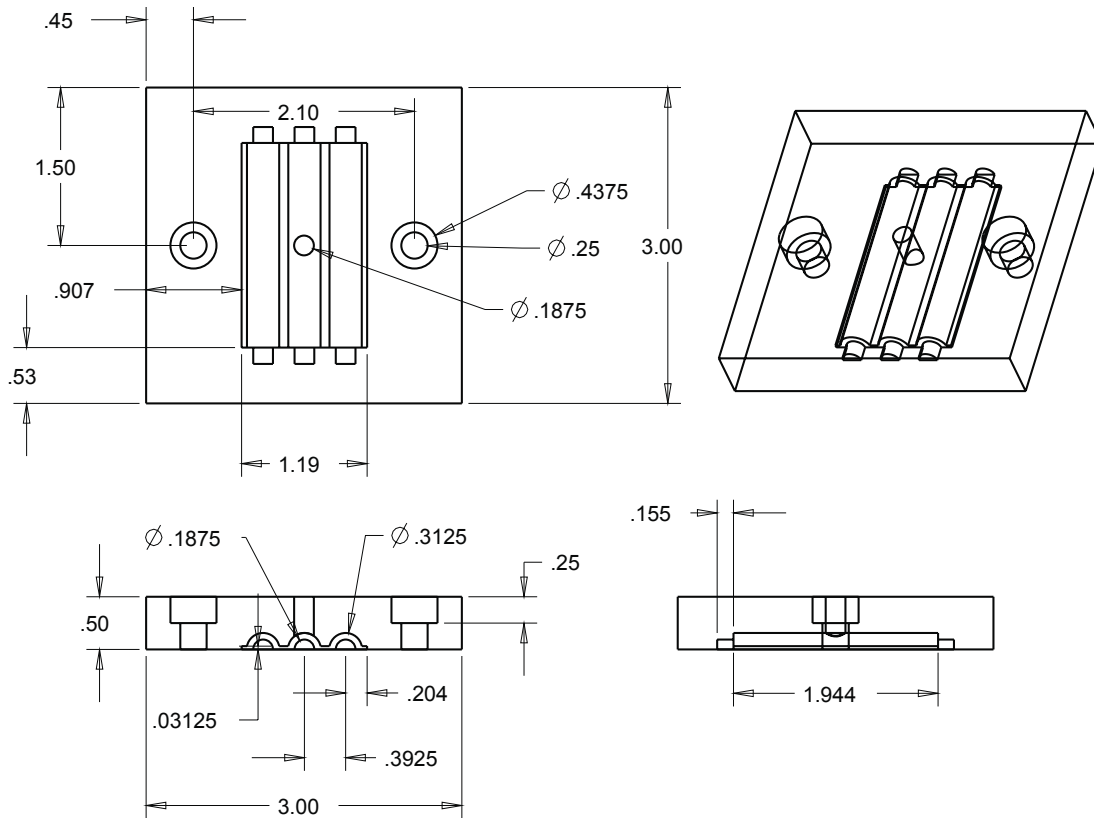


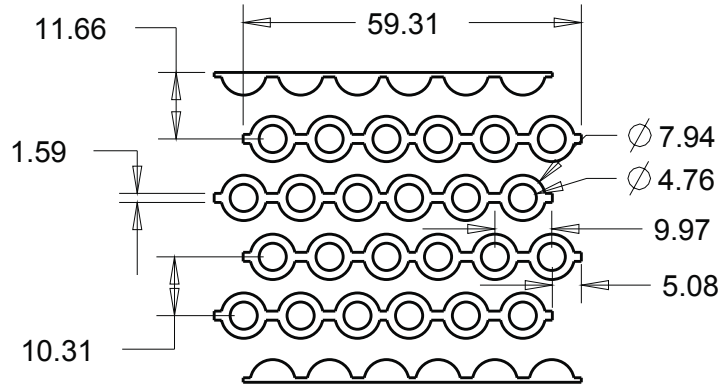
Figure 43 Drawing of aluminum mold cavity for webbed-tube array
(All dimensions in inches)

Once the webbed-tube arrays were molded (Figure 44), they were assembled in a staggered fashion as a cross flow heat exchanger as shown in Figure 45 below. Note that there are inserts on the top and bottom of the webbed-tube array. The purpose of the inserts is to distribute the flow more evenly among the air channels, although we will show later that there is still some bypass flow due to the additional distance from the webbed-tubes to the inserts. In total, there are five “wavy” channels created by the webbed-tube array.

The webbed-tube heat exchanger, assembled with inlet and outlet manifolds is shown below in Figure 46.



Figure 44 Injection-molded webbed-tube array



All units in mm

Figure 45 Webbed tube heat exchanger drawing (tube length = 36.58 mm)

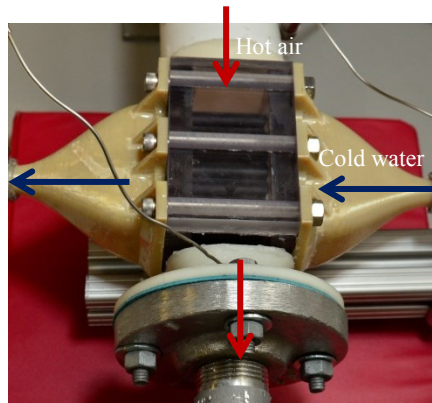


Figure 46 Assembled Injection-Molded WTHX

5.2.2 3D Printed webbed-tube heat exchanger

In collaboration with Stratasys, Inc., we successfully designed, fabricated, and tested a 3D-printed WTHX. To our knowledge, this is the first plastic heat exchanger made by additive manufacturing.

The heat exchanger was fabricated at a Stratasys facility in Eagan, MN, and it constitutes the first time that a plastic heat exchanger has been manufactured through

Stratasys' Fused Deposition Modeling (FDM) technology and used to successfully transfer heat through a polymer structure from a hot gas to a cold liquid.

5.2.3 Overview of FDM

The FDM process consists of seven main steps [95], which are:

1. Loading of material
2. Liquifaction of material
3. Extrusion
4. Solidification
5. Positional control
6. Bonding
7. Support generation

Besides all the design advantages of additive manufacturing, fused-deposition modeling is an attractive, relatively new, growing technology with several attractive features [95]:

- A wide range of polymer materials is available
- The mechanical properties of FDM parts are among the strongest for any polymer-based additive manufacturing process
- FDM machines come in a wide range of sizes
 - Low cost machine: build envelope is 6'' × 8'' × 8''
 - More expensive machine: build envelope is 36'' × 24'' × 36''

However, there are some limitations to the process that are worth mentioning.

- Layer thickness or machine resolution is currently limited to 0.076 mm

- The use of circular nozzles to extrude the material makes it impossible to draw, or print, true sharp corners
- If a high level of precision is required, build times and thus production costs increase significantly
- Due to the nature of the layer bonding, parts are noticeably weaker in the direction in which layers of material are added, and so FDM parts tend to be significant anisotropic

5.2.4 FDM Webbed-Tube Design

Several attempts were made by Stratasys to make a leak-proof WTHX. Initially, significant water leaks occurred at the regions where the tube is joined to the webbing. Figure 47 below shows water droplets leaking through the tube. Later on, it was determined that the porosity at those corners was a function of the tool path used to print the WTHX.

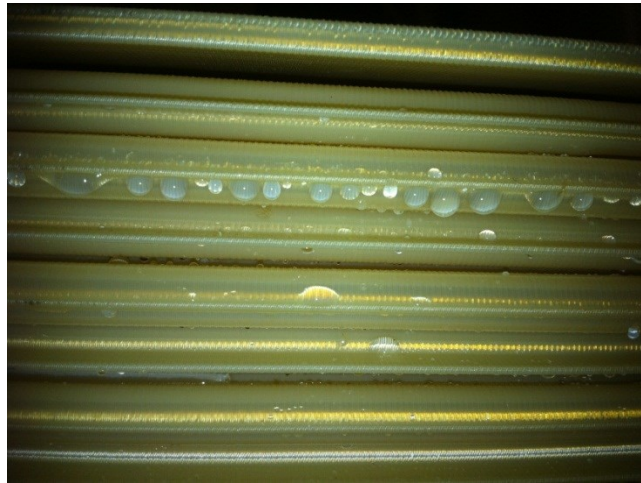


Figure 47 ULTEM HX tested for water leaks

Stratasys' engineers later determined that using two individual tool paths, as is shown in Figure 48a, is conducive to leaks at sharp corners. Thus, a new tool path

was proposed (Figure 48b), which when implemented provided leak proof webbed-tube arrays.

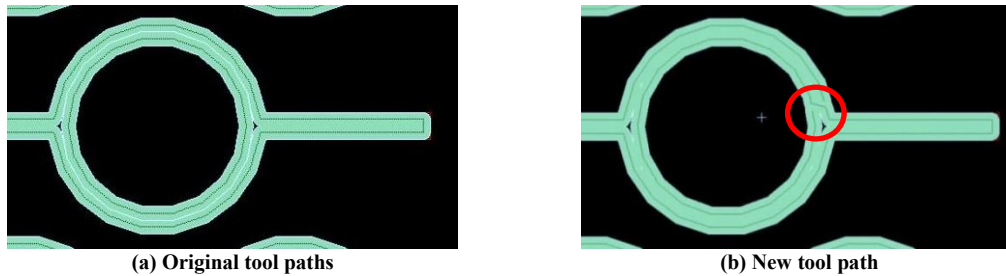


Figure 48 FDM Tool Paths

A 3D-printed polycarbonate WTHX is shown below in Figure 49, along with its dimensions. A filled polycarbonate WTHX was also fabricated and tested. Although the volume fraction of the filler is unknown to us, the experimental thermal performance showed that the thermal conductivity enhancement was not significant.

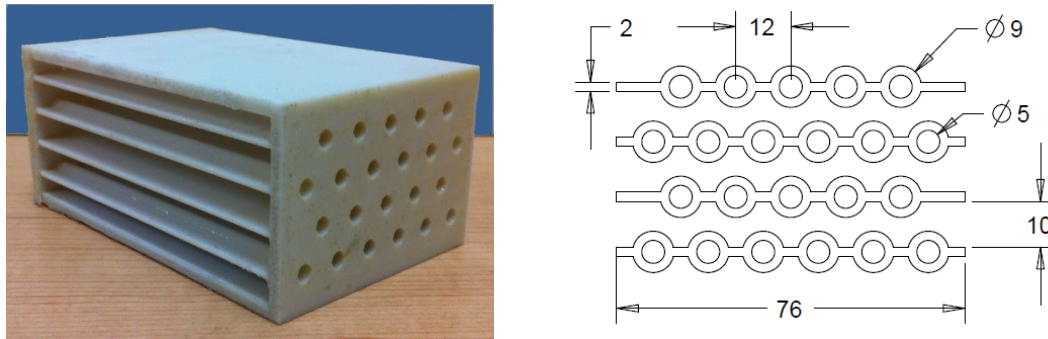


Figure 49 FDM WTHX made with polycarbonate
(All dimensions in mm, tube length = 120 mm)

5.3 Heat Exchanger Test Facility

The heat exchangers were tested in an air-to-water test facility. The setup of the test facility is quite simple. Air is driven by a blower into a 50cm-diameter pipe that is 1.8m long. Along the way, the air is heated by a resistance heater to temperatures up to 120°C. The air then goes through the heat exchanger and through a vortex-shedding flow meter with an accuracy of 1% of the flow meter reading. Afterwards, the air passes through a secondary shell-and-tube heat exchanger to cool it down to

room temperature. Water is also fed to the heat exchanger at the building temperature and pressure. The water flow rate is also measured with a vortex-shedding flow meter. The accuracy of all the measured quantities is summarized in Table 13 below.

Measured Quantity	Accuracy
Water flow rate (10	$\pm 3\%$ of full scale
Air flow rate	$\pm 1\%$ of reading
Temperature	$\pm 0.54^\circ\text{C}$

Besides the two flow rates, air temperature is measured with thermocouples placed at the inlet and outlet of the heat exchangers, and surface temperature is measured at several locations in the heat exchanger. Figure 50 below illustrates the locations where temperature measurements are taken. The red circles mark the thermocouple locations. Ten thermocouples were placed next to the inlet and outlet of each channel. In addition, ten thermocouples were embedded in the surface of a webbed-tube array in both the tubes and the webbings between the tubes.

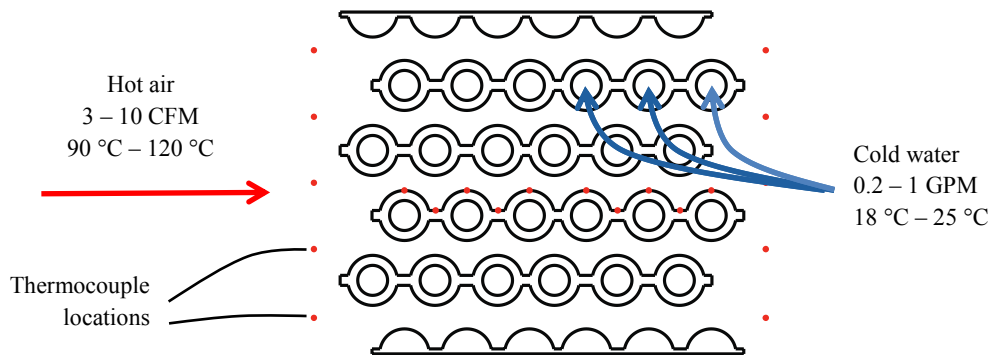


Figure 50 Thermocouple Locations (location marked by red dots)

5.4 Thermal Anisotropy in Webbed-Tube Array

The results from the mold filling simulations in Moldflow also include a prediction of the local fiber orientation tensor. An in-depth study of this process-induced anisotropy [91], shown in chapter 4, showed that the fiber orientation tensor can be

used along with the Nielsen model [41] to calculate the local thermal conductivity tensor.

Figure 51 below shows the calculated components of the thermal conductivity tensor along a radial line with an angle of 70° with respect to the horizontal axis. Using the Nielsen model [41], the lower and upper bounds of thermal conductivity were calculated to be $k_{\perp}=0.5$ W/m-K and $k_{\parallel}=6.43$ W/m-K. Then, using equation (13), the thermal conductivity tensor can be readily calculated. The results in Figure 51 are quite surprising. Generally, the fiber orientation tensor component –and the resulting thermal conductivity- in the thru-wall (radial) direction in an injection-molded component is usually very low. This occurs because the fibers tend to align, mostly, with the streamlines of the melt flow. Therefore, one would expect the radial thermal conductivity to be much lower than in the hoop direction. However, the path around the circular tube appears to favor both directions almost equally, and so the thermal conductivity in the radial direction is remarkably similar to the hoop direction. From this results, we can expect that an “effective” thermal conductivity must be significantly higher than the lower bound thermal conductivity $k_{\perp}=0.5$ W/m-K.

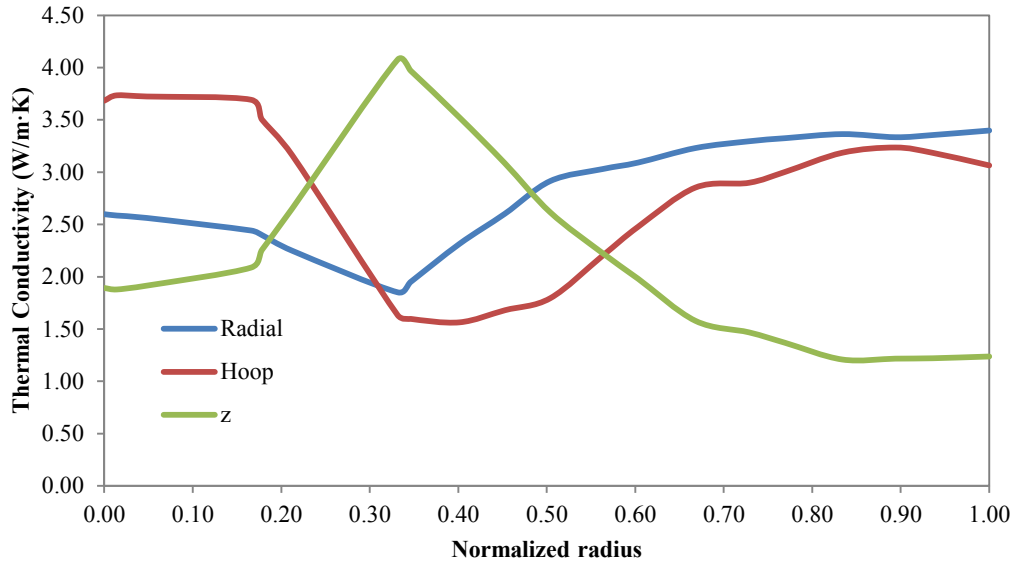


Figure 51 Thermal conductivity tensor components along the radius of the tube ($k_{high}=6.43$ W/mK, $k_{low}=0.5$ W/m-K, angle w.r.t x-axis = 70°)

5.5 Thermo-fluid performance comparison to plate-fin heat exchanger

In order to illustrate the value of this heat exchanger design, its heat transfer performance was benchmarked against the more classical plate-fin design. For the example discussed here, both heat exchangers were assumed to have a counter-flow configuration with hot methane gas at 90°C and 500 kPa being cooled by seawater at 35°C and 400 kPa. In the literature, this application shows great potential for polymer heat exchangers [96]. The volumetric flow rates were equal for both exchangers, with the seawater flow rate kept constant at 0.02 m^3/s , and the gas flow rate varying from 0.02 to 0.1 m^3/s .

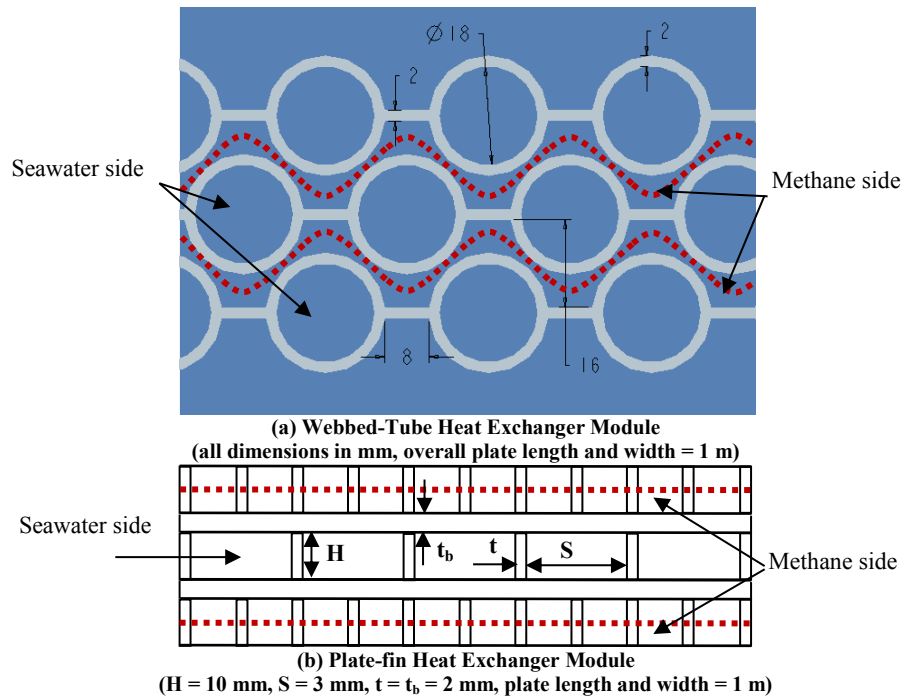


Figure 52 Sketch of both exchangers with appropriate dimensions (red dashed lines indicate the control volume –or building block- for which the heat transfer rate and pumping power are calculated)

Cross-sectional views of both HX designs are shown in Figure 52. Note that for the webbed tube heat exchanger the methane gas flows in between plates, while the seawater flows inside the pipes. The control volumes used to calculate the heat transfer rate and pumping power calculations are outlined with red dashed lines. These constitute building blocks for a larger heat exchanger. In both cases, the control volume consists of a single set of seawater channels, which receives heat from the methane “half channels” above and below, so that the methane channels also transfer heat to the water channels on the opposite side.

It should be noted that in both heat exchanger configurations, the thermal conductivity was assumed to be anisotropic, as is the case for most thermally enhanced polymer matrix composites (PMC) [91]. Assuming that the fibers mostly lie parallel to the plane of the wall, the in-plane conductivity was taken as 10 W/m·K,

and the thru-plane conductivity was set equal to $0.65 \text{ W/m}\cdot\text{K}$. For the plate fin design, the described anisotropy results in the rectangular fins having a conductivity of $10 \text{ W/m}\cdot\text{K}$, while the plate itself will have a conductivity of $0.65 \text{ W/m}\cdot\text{K}$ for 1D conduction in the vertical direction, as in Figure 52b. For the webbed-tube design, radial conduction through the tube is assumed, and since this direction is perpendicular to the planes of the wall (or the axial direction), the conductivity is $0.65 \text{ W/m}\cdot\text{K}$. Since the plate itself is exposed to methane on both its sides, there is no significant conduction in the through-thickness direction. However, heat can be expected to flow from the tubes into the plate and then the methane, requiring that the wall be treated as an extended surface with a conductivity of $10 \text{ W/m}\cdot\text{K}$.

Table 14 below compares important geometrical and performance parameters of the WTHX and finned plate heat exchanger configurations. Fluid velocities, hydraulic diameters, pressure drops, Reynolds numbers, and heat transfer coefficients are very similar for the two heat exchanger designs. As a consequence of these similarities, the pumping power for both exchangers matches very closely, as shown in Figure 53.

However, wetted areas on the seawater and methane sides are dissimilar. The plate-fin exchanger has almost twice the wetted area compared to the webbed-tube on the gas side, but only 70% of the water-side webbed-tube area.

Table 14 Heat Exchanger Parameters
 (Seawater inlet conditions: 0.02 m³/s, 35 °C, 400 kPa. Methane inlet conditions: 0.02 to 0.1 m³/s, 90 °C, 500 kPa. Both exchangers have a counterflow arrangement)

		Webbed-Tube	Plate-fin
Methane-side area	m²	2.76	4.298
Water-side area	m²	2.02	1.446
Methane hydraulic diameter	mm	8.684	6.667
Water hydraulic diameter	mm	18	16
Methane velocity	m/s	3.3 - 16.7	2.8 – 14
Water velocity	m/s	2.2	2.1
Methane pressure drop	Pa	76 – 1300	77 - 1290
Water pressure drop	Pa	4115	4200
Methane Reynolds number	-	6700 - 34000	4300 - 21800
Water Reynolds number	-	54700	46500
Gas heat transfer coefficient	W/m²K	104 – 370	90 – 340
Water heat transfer coefficient	W/m²K	11000	10700

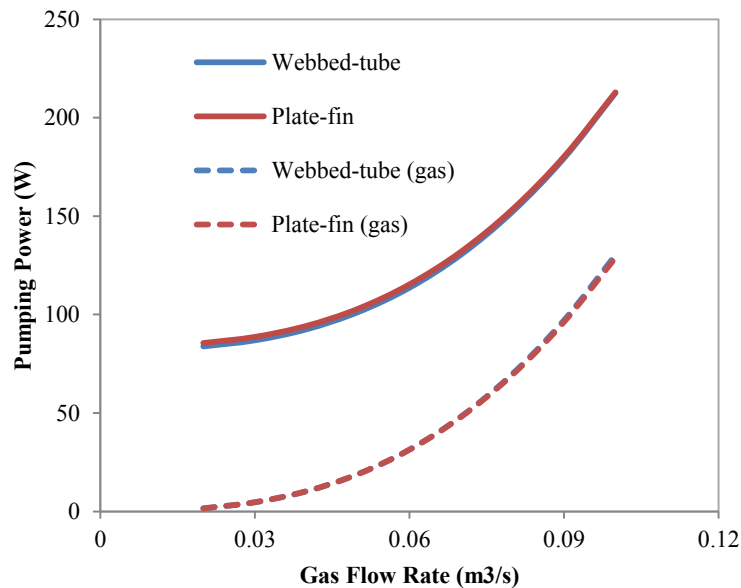


Figure 53 Heat Exchanger Pumping Power
 (Seawater inlet conditions: 0.02 m³/s, 35 °C, 400 kPa. Methane inlet conditions: 90 °C, 500 kPa. Both exchangers have a counterflow arrangement)

Figure 54 below displays the dependence of the heat transfer rate on the gas flow rate for the conditions stated and reveals that the heat transfer rate of both heat exchangers is almost equal. This is surprising since the plate-fin heat exchanger has nearly twice as much wetted area on the gas side, and the gas side requires additional area to

overcome the relatively low heat transfer coefficient. However, most of the area advantage of the plate-fin comes from the fin area, which must be corrected for fin efficiency. On the other hand, most of the wetted area of the plate-coil heat exchanger is the external area of the tubes, or “bumps” on the plate, which does not suffer the reduced performance impact of fin efficiency. In this fashion, the plate-coil exchanger can provide the same heat transfer rate as the plate-fin, with the same pumping power, but much less surface area.

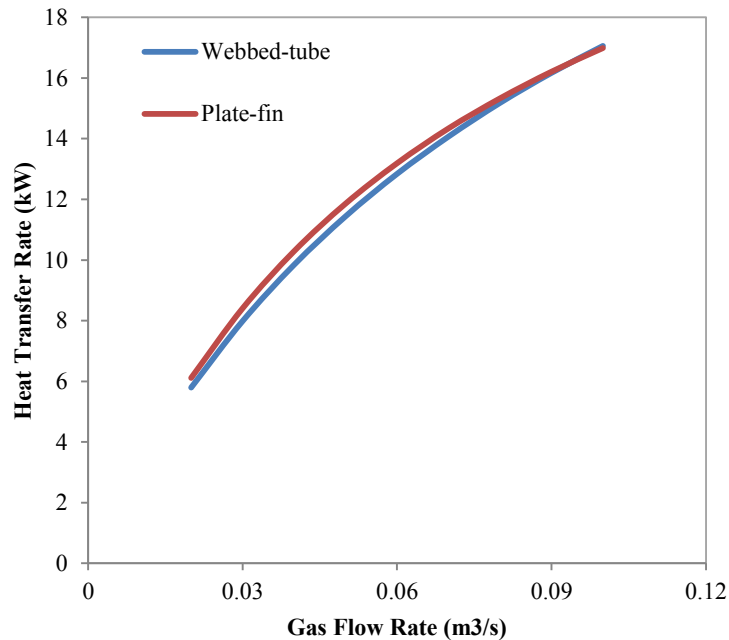


Figure 54 Heat Exchanger Heat transfer Rate
 (Seawater inlet conditions: 0.02 m³/s, 35 °C, 400 kPa. Methane inlet conditions: 90 °C, 500 kPa. Both exchangers have a counterflow arrangement)

As a result of this equality in heat transfer rate, the webbed-tube heat exchanger can provide more heat transfer per unit mass than the plate-fin. The plot in Figure 55 shows that the webbed-tube heat exchanger can transfer up to 50% more heat per unit of mass than the plate-fin exchanger.

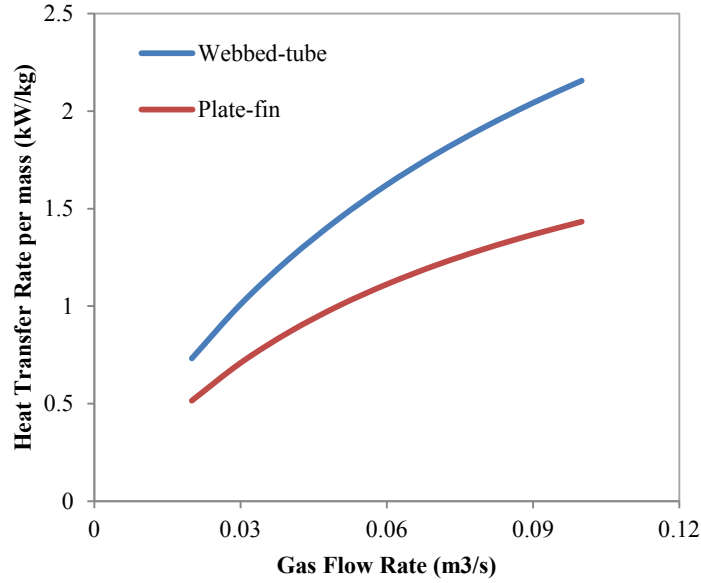


Figure 55 Heat Exchanger Mass-Specific Heat Transfer Rate (Seawater inlet conditions: 0.02 m³/s, 35 °C, 400 kPa. Methane inlet conditions: 90 °C, 500 kPa. Both exchangers have a counterflow arrangement)

5.6 Analytical Modeling of Webbed-Tube Heat Exchanger

The heat transfer for any heat exchanger can be written as

$$q = UA\Delta T_{lm} \quad (5.1)$$

where UA is the overall thermal conductance, and ΔT_{lm} is the log-mean temperature difference. The overall thermal conductance is written as the inverse of the overall thermal resistance as

$$UA = \frac{1}{R_{total}} \quad (5.2)$$

For this heat exchanger, there are three thermal resistances that make up the overall thermal resistance

$$R_{total} = R_{conv,1} + R_{wall} + R_{conv,2} \quad (5.3)$$

where $R_{conv,1}$ and $R_{conv,2}$ are the convective thermal resistance for the air-side and the water side, respectively. R_{wall} is the conductive thermal resistance. For the webbed-tube heat exchanger, $R_{conv,1}$ is written as

$$R_{conv,1} = \frac{1}{\eta_o h A} \quad (5.4)$$

where η_o is the surface efficiency based on the fin efficiency, h is the heat transfer coefficient and A is the surface area. The wall thermal resistance R_{wall} is written as

$$R_{wall} = \frac{\ln(r_2/r_1)}{2\pi k L} \quad (5.5)$$

where r_2 is the tube outer radius, r_1 is the tube inner radius, k is the thermal conductivity, and L is the tube length.

The log-mean temperature difference is defined as

$$\Delta T_{lm} = \frac{\Delta T_1 - \Delta T_2}{\ln(\Delta T_1/\Delta T_2)} \quad (5.6)$$

where for a counterflow heat exchanger ΔT_1 and ΔT_2 are defined as

$$\Delta T_1 = T_{h,i} - T_{c,o} \quad (5.7)$$

$$\Delta T_2 = T_{h,o} - T_{c,i} \quad (5.8)$$

where the subscripts h, c, i, and o stand for hot fluid, cold fluid, inlet, and outlet, respectively.

For a cross flow heat exchanger a correction factor F can be applied to the counterflow ΔT_{lm} . However, when the change in temperature in one of the fluids is negligible, as is the case here, the correction factor is 1.

Finally, an appropriate correlation must be selected for calculating the Nusselt number and the heat transfer coefficient. For the webbed-tube heat exchanger, it was not immediately clear which correlation can be used for the fluid outside of the tubes. In this study, correlations for flow in rectangular ducts were considered using a hydraulic diameter based on the flow cross-sectional area and the wetted perimeter. If the heat exchanger is arranged in a cross flow configuration, the flow outside of the

tubes looks very similar to a tube bundles, except that the webbing connecting the tubes prevents mixing between rows of tubes. Nevertheless, tube bundle correlations were also considered in this study.

5.6.1 Flow in rectangular ducts

5.6.1.1 Fully Developed Flows

For a laminar, hydrodynamically and thermally fully developed flow in a rectangular duct exposed to a uniform heat flux and uniform wall temperature, the friction factor and Nusselt number data was provided by Shah and Bhatti [97] as shown in [98].

The product of the fully developed friction factor and the Reynolds number is a function of the aspect ratio α :

$$f_{fd} = \frac{24}{Re_{D_h}} (1 - 1.3553\alpha + 1.9467\alpha^2 - 1.7012\alpha^3 + 0.9564\alpha^4 - 0.2537\alpha^5) \quad (5.9)$$

The Nusselt number correlation for constant temperature is

$$Nu_{fd,T} = 7.541(1 - 2.610\alpha + 4.970\alpha^2 - 5.119\alpha^3 + 2.702\alpha^4 - 0.548\alpha^5) \quad (5.10)$$

and the correlation for constant heat flux is:

$$Nu_{fd,H} = 8.235(1 - 2.042\alpha + 3.085\alpha^2 - 2.477\alpha^3 + 1.058\alpha^4 - 0.186\alpha^5) \quad (5.11)$$

For turbulent flow, the Petukhov and Popov [99] correlation, shown below, was chosen because it has the best accuracy ($\pm 5\%$) of the correlations presented by Shah and Sekulic [98].

$$\text{Nu} = \frac{(f/2)\text{Re} \cdot \text{Pr}}{C + 12.7(f/2)^{1/2}(\text{Pr}^{2/3} - 1)}$$

$$4000 \leq \text{Re} \leq 5 \times 10^6$$

$$0.5 \leq \text{Pr} \leq 10^6$$

$$C = 1.07 + \frac{900}{\text{Re}} - \frac{0.63}{1 + 10\text{Pr}}$$
(5.12)

The friction factor for turbulent flow in a smooth duct can be obtained with an accuracy of $\pm 2\%$ by using a correlation provided by Bhatti and Shah [100] as presented in [98].

$$f = 0.00128 + 0.1143\text{Re}^{-0.311}$$
(5.13)

5.6.1.2 Hydrodynamically Developing Flows

Friction factors in the entrance region are higher than in the fully developed region. As shown by Shah and Sekulic [98], the hydrodynamic entrance length in a circular tube is given by

$$\frac{L_{hy}}{D_h} = \begin{cases} 0.056 Re & \text{for laminar flow (Re} \leq 2100) \\ 1.359 Re^{1/4} & \text{for turbulent flow (Re} > 10^4) \end{cases}$$
(5.14)

In laminar flow, the apparent friction factor in the entrance region in circular and some noncircular ducts is calculated with the following [101]:

$$f_{app} \cdot \text{Re} = 3.44(x^+)^{-0.5} + \frac{K(\infty)/(4x^+) + f\text{Re} - 3.44(x^+)^{-0.5}}{1 + C'(x^+)^{-0.2}}$$
(5.15)

where

$$x^+ = \frac{x}{D_h \text{Re}}$$
(5.16)

and values for $K(\infty)$ and C' can be obtained from [101].

While the turbulent friction factors in the entrance region are higher than those in the fully developed flow, the entrance length is very short and does not influence the pressure drop significantly, compared to other factors. Therefore, it is generally neglected when evaluating the pressure drop [98].

5.6.1.3 Thermally developing flows

The mean Nusselt number for developed velocity profiles and developing temperature profiles in laminar flow were correlated by Shah and London [101] as

$$\text{Nu}_{m,T} = 0.641(f \cdot \text{Re})^{1/3}(x^*)^{-1/3} \quad (5.17)$$

$$\text{Nu}_{m,H} = 0.775(f \cdot \text{Re})^{1/3}(x^*)^{-1/3} \quad (5.18)$$

where f is the friction factor for fully developed flow and $x^* = x/(D_h \cdot \text{Re} \cdot \text{Pr})$

Bhatti and Shah [100] provided correlations for Nusselt numbers in the thermal entrance region. For $\text{Pr}=0.7$ the following correlation gives Nusselt number values within $\pm 12\%$ of experimental values.

$$\frac{\text{Nu}_m}{\text{Nu}_\infty} = 1 + \frac{C_6}{x/D_h}$$

$$x/D_h > 3, 3500 < \text{Re} < 10^5, \text{ and } 0.7 < \text{Pr} < 75 \quad (5.19)$$

$$C_6 = \frac{(x/D_h)^{0.1}}{\text{Pr}^{1/6}} \left(0.68 + \frac{3000}{\text{Re}^{0.81}} \right)$$

5.6.1.4 Simultaneously Developing Flow

In laminar flow, heat transfer in the thermal entrance region is higher for a developing velocity profile than for a fully developed profile [98]. The values of the Nusselt number for simultaneously developing flow in a rectangular duct with constant wall

temperature and constant heat flux for a $Pr = 0.72$ were provided by Wibulswas [102].

The values were adjusted for other Prandtl numbers as shown by Kakaç et. al. [103].

The following approach was taken from Nellis and Klein [104].

A dimensionless length appropriate for a thermally developing flow is L^* , sometimes referred as the inverse of the Graetz number:

$$L^* = \frac{1}{Gz} = \frac{L}{D_h Re_{D_h} Pr} \quad (5.20)$$

For a constant wall temperature:

$$a_T = 0.0357122 + 0.460756236\alpha - 0.214865737\alpha^2$$

b_T

$$= \begin{cases} 0.940362 + \alpha(0.739606 - 0.940362)/0.167, & \alpha < 0.167 \\ 0.801105912 - 0.419264242\alpha + 0.293641181\alpha^2, & \alpha \geq 0.167 \end{cases} \quad (5.21)$$

$$A = a_T e^{-b_T \ln L^*}$$

$$B = \begin{cases} 0.6847 + 0.3153e^{-1.26544559(\ln Pr - \ln 0.72)}, & Pr > 0.72 \\ 1.68 - 0.68e^{0.32(\ln Pr - \ln 0.72)}, & Pr \leq 0.72 \end{cases}$$

$$\overline{Nu}_T \approx Nu_{fd,T} + A \cdot B$$

For constant heat flux:

$$a_H = 0.113636994 + 0.712134212\alpha - 0.392104717\alpha^2$$

b_T

$$= \begin{cases} 0.940362 + \alpha(0.699466 - 0.940362)/0.25, & \alpha < 0.25 \\ 0.774133656 - 0.350363736\alpha + 0.198543081\alpha^2, & \alpha \geq 0.167 \end{cases} \quad (5.22)$$

$$A = a_H e^{-b_H \ln L^*}$$

$$B = \begin{cases} 0.6847 + 0.3153e^{-1.26544559(\ln Pr - \ln 0.72)}, & Pr > 0.72 \\ 1.68 - 0.68e^{0.32(\ln Pr - \ln 0.72)}, & Pr \leq 0.72 \end{cases}$$

$$\overline{Nu}_H \approx Nu_{fd,H} + A \cdot B$$

5.6.2 Heat transfer in tube bundles

As an alternative to modeling a WTHX as a rectangular duct, the staggered arrays of webbed tubes may be seen as a standard tube bundle, if the webbing joining the tubes is ignored. Therefore, an additional set of Nusselt number correlations for a staggered array of tubes developed by Zukauskas [105], and shown in [106], can be used to estimate the average heat transfer coefficient.

The average Nusselt number for a staggered tube bundle in cross flow is then:

$$\overline{Nu}_b = \begin{cases} 1.04c_n Re_b^{0.4} Pr_b^{0.36} \left(\frac{Pr_b}{Pr_w}\right)^{0.25} & \text{for } Re_b = 1 - 500 \\ 0.71c_n Re_b^{0.5} Pr_b^{0.36} \left(\frac{Pr_b}{Pr_w}\right)^{0.25} & \text{for } Re_b = 500 - 10^3 \\ 0.35c_n Re_b^{0.6} Pr_b^{0.36} \left(\frac{Pr_b}{Pr_w}\right)^{0.25} \left(\frac{X_t}{X_l}\right)^{0.2} & \text{for } Re_b = 10^3 - 2 \times 10^5 \\ 0.35c_n Re_b^{0.8} Pr_b^{0.4} \left(\frac{Pr_b}{Pr_w}\right)^{0.25} \left(\frac{X_t}{X_l}\right)^{0.2} & \text{for } Re_b = 2 \times 10^5 - 2 \times 10^6 \end{cases} \quad (5.23)$$

where X_l is the longitudinal spacing of consecutive rows, and X_t is the transversal spacing of two consecutive tubes, while c_n is a correction factor for the number of tube rows [106]. The Reynolds number is calculated using the maximum average velocity and the tube diameter:

$$Re_b = \frac{\rho u_{\max} D}{\mu} \quad (5.24)$$

The Zukauskas correlation is said to have an uncertainty within $\pm 15\%$.

The Reynolds numbers in the experiments performed for this study were no greater than 2300, so only the laminar flow correlations were needed. Figure 56 below shows the Nusselt number as a function of Reynolds number for both the duct flow

correlations and the staggered tube bundle correlations. In the case of the duct flow correlations, the flow length is short relative to the thermal or hydrodynamic entry length, and so the profiles are simultaneously developing. The staggered tube bundle curve has several jumps, and that is due to the use of different forms of the equation at different Reynolds number regimes. Most of the experimental data occurs at Reynolds numbers between 1000 and 2300, so the curves should be fairly smooth in the range of interest.

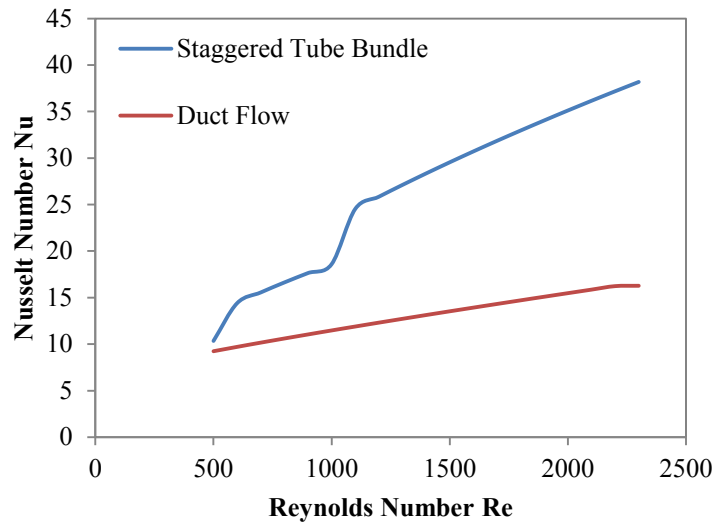


Figure 56 Nusselt Number as a function of Reynolds Number ($Pr=0.71$, $Pr_{wall} = 0.72$ Aspect Ratio = 0.09, $L/D=9$)

While the two Nusselt numbers are close at a Reynolds number of 500, the values quickly depart from each other as the Reynolds number increases. From an analytical perspective, using the two sets of correlations described above only provides an approximate range of Nusselt numbers for the range of air flow rate under study. Therefore, for calculating accurate values of an average heat transfer coefficient, we have relied on numerical simulations of a WTHX using Ansys Icepak.

5.7 Numerical simulation of webbed-tube heat exchanger

Since the analytical results provided a wide range for the air-side Nusselt numbers and heat transfer coefficients, it was necessary to use numerical simulations to obtain more accurate values. Ansys Icepak, which serves as a front-end tool to Ansys Fluent, was used to evaluate the thermo-fluid performance of the webbed-tube prototype heat exchanger. The simulation was setup to mimic similar conditions to the cross flow test facility. Using a refined mesh with more than 600 thousand elements, the numerical results obtained helped to investigate the flow and temperature distribution inside the heat exchanger, as well as to calculate an average heat transfer coefficient for the range of mass flow rate under study. The following parameters were used in the simulations:

Table 15 Ansys Icepak Inputs

Input parameter	Value
Air temperature Inlet	120 °C
Water temperature Inlet	18 °C
Air flow rate	1000 – 5000 cm ³ /s
Water flow rate	12 cm ³ /s
Thermal conductivity	1 W/m·K

Figure 57 shows an illustration of the air velocity streamlines inside the webbed-tube heat exchanger. The plot reveals a wavy shape of the streamlines, which follow the staggered arrangement of the tubes. Although the streamlines have a wavy “character,” the velocity close to the webbings is very low. As a result, the heat transfer coefficient at the webbing surface area is also much lower than around the circumference of the tube. Further study revealed that the webbing heat transfer coefficient could be as much as an order-of-magnitude lower the tube’s, ultimately contributing only a small effective area for heat transfer. The results in Figure 57 also

revealed that despite the inserts on the top and bottom of the heat exchanger, there was still bypass flow on the top and bottom air-channels. As a result, the mean velocities are also higher on the top and bottom flow channels. The flow rate on each channel was recorded for each simulation, and it was determined that, on average, approximately 25% of the total flow rate goes through each of the top and bottom channels, while through the three middle channels only 17% of the flow rate goes through each, as can be seen in Table 17 below. Note that knowledge of this distribution is useful to calculate a more accurate experimental heat transfer rate of the WTHX prototype, presented in section 5.8.

Table 16 Flow distribution in WTHX
(total air flow = 4000 cc/s)

	Flow [m ³ /s]	% Flow
Channel 1 (bottom)	0.00091	23%
Channel 2	0.00069	17%
Channel 3	0.00068	17%
Channel 4	0.00068	17%
Channel 5 (top)	0.00101	26%
Total	0.00396	100.00%

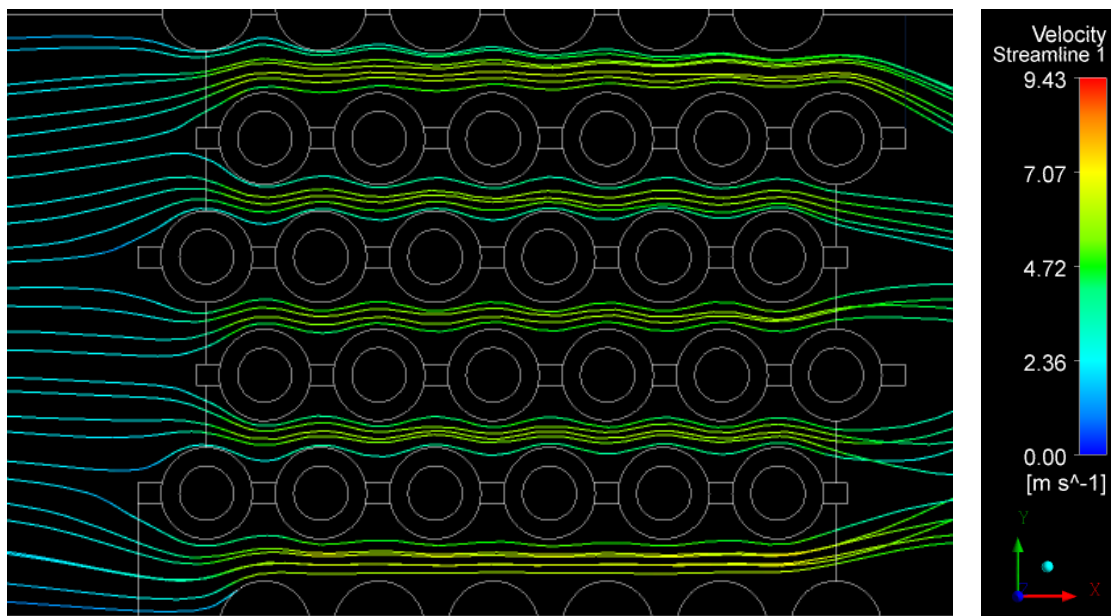


Figure 57 Velocity Streamlines in Webbed-Tube Heat Exchanger (air flow = 4000 cc/s, inlet temperature = 120 °C)

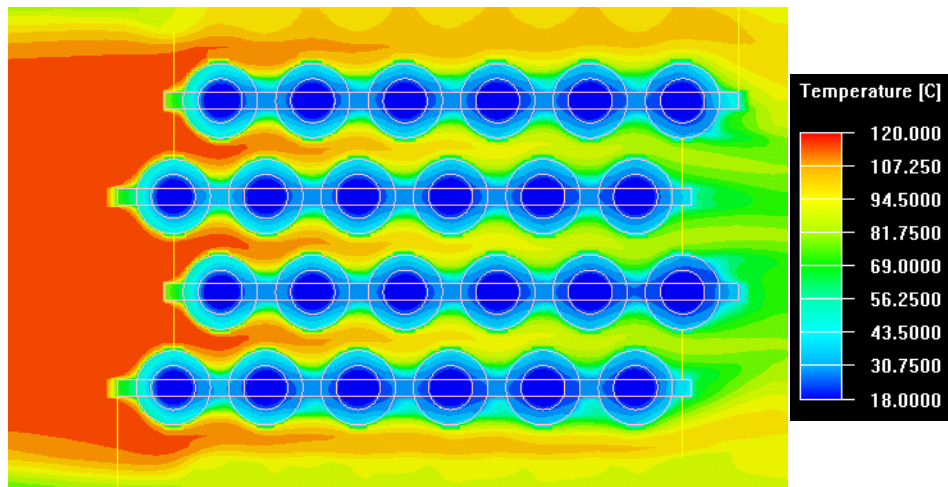


Figure 58 Temperature contours across WTHX (air flow = 4000cc/s, inlet temperature = 120 °C)

Figure 58 shows the temperature contours at a plane located at the center of the WTHX, midway along the tube length. The contours again show the wavy character of the WTHX. The contours also confirm that the fins, or webbings, stay much cooler than the tube surface, thus hindering their contribution to heat transfer.

As a result of the flow distribution shown in Table 16, the air temperature is approximately 18-20°C hotter at the top and bottom channels than in the middle channels. Given these significant differences in flow rate and temperature drop, the following analysis of the numerical results and subsequent comparison to experimental results was focused on the middle portion (3 middle air channels) of the WTHX, where the assumption of equal flow rate and temperature drop appears to be valid in the range of flow parameters under study.

We can now use the heat transfer rate and resulting temperatures calculated in Icepak to calculate average heat transfer coefficients as a function of flow rate using the Equations presented in section 5.6, and those values can be compared to those calculated using the two sets of Nusselt number correlations discussed in section 5.6.1 and 5.6.2.

Figure 59 compares the heat transfer coefficients predicted by the two sets of correlations discussed earlier with the coefficients calculated in Icepak. The plot shows that the Icepak results are nearly contained by the range defined by the two correlation curves, with the exception of the value at a mass flow rate of 0.001 kg/s. Though the correlations appear to give good rough estimates of lower and upper bounds of the heat transfer coefficient, the numerical results are preferred for the analysis done here, since accurate values are needed to compare to the experimental results.

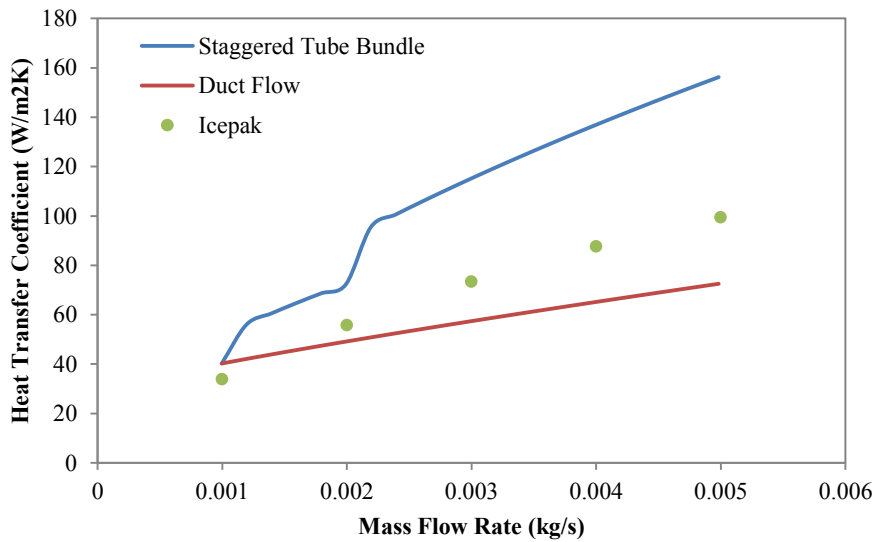


Figure 59 Heat transfer coefficient as a function of mass flow rate

5.8 Analysis of Experimental Results and Conclusions

The tools developed in the previous sections can help in analyzing the experimental results collected from the test facility.

5.8.1 3D-Printed WTHX

Although the 3D-printed WTHX was made from a proof-of-concept perspective, a small amount of thermal performance data was collected. Figure 60 shows the overall

thermal conductance of filled and unfilled polycarbonate WTHXs as a function of air flow rate. On average, both heat exchangers were able to transfer around 65W from hot air at 120°C to water at 27°C. Comparison of the experimental results to an analytical model revealed the effective thermal conductivity of the unfilled polycarbonate exchangers was relatively low at 0.13 W/m·K, while the filled polycarbonate showed little improvement with an average conductivity of 0.16 W/m·K.

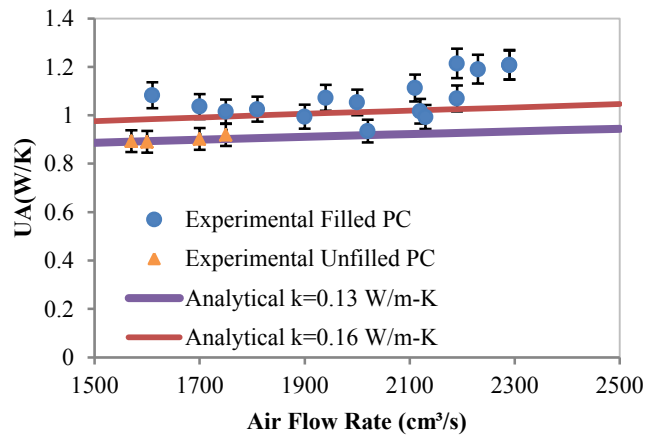


Figure 60 3D Printed WTHX Performance
(Water: 1 GPM, inlet 27 °C, Air inlet: 120 °C, HX: 500 cm³ made with filled and unfilled polycarbonate)

5.8.2 Injection-molded WTHX

Figure 61 shows the experimental heat transfer rate as a function of mass flow rate, the data was collected at different air inlet temperatures as well as different flow rates. The results show that as the mean temperature difference between the air and the water increases so does the heat transfer rate. Also, as the air mass flow rate increases, the air heat transfer coefficient follows the trend shown in Figure 59, and the heat transfer rate increases as well.

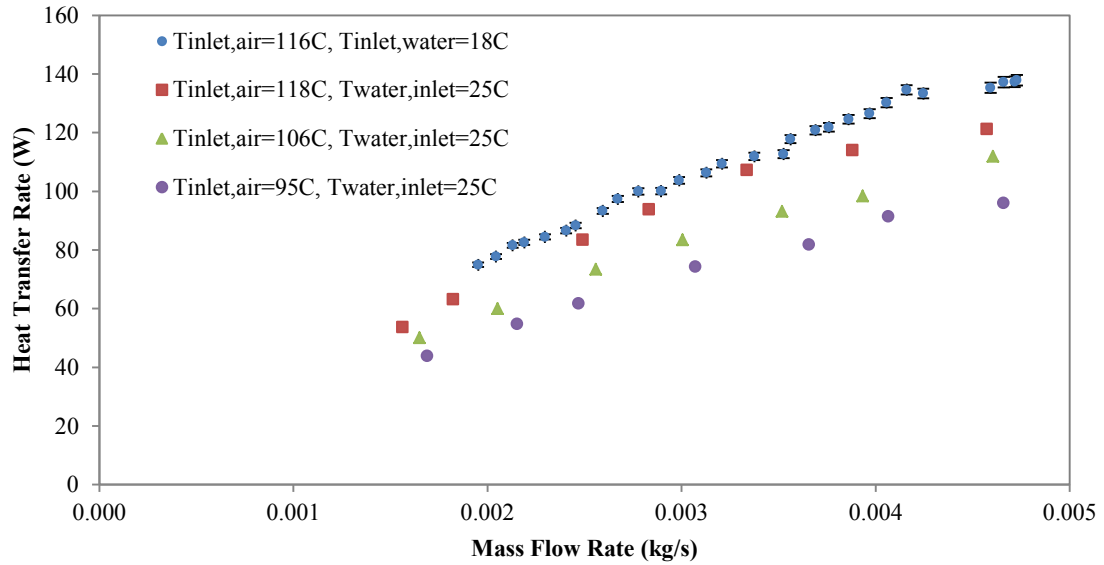


Figure 61 Experimental Heat Transfer Rate as a Function of Mass Flow Rate (Water flow rate $\sim 10\text{cm}^3/\text{s}$)

We can use Equation 5.1 to calculate the overall thermal conductance. In this way we are normalizing the heat transfer rate by the logarithmic mean temperature difference, shown in Equation 5.6. By comparing the analytical model of UA to the experimental results we can find a least squares fit to the experimental data for a given “effective” thermal conductivity.

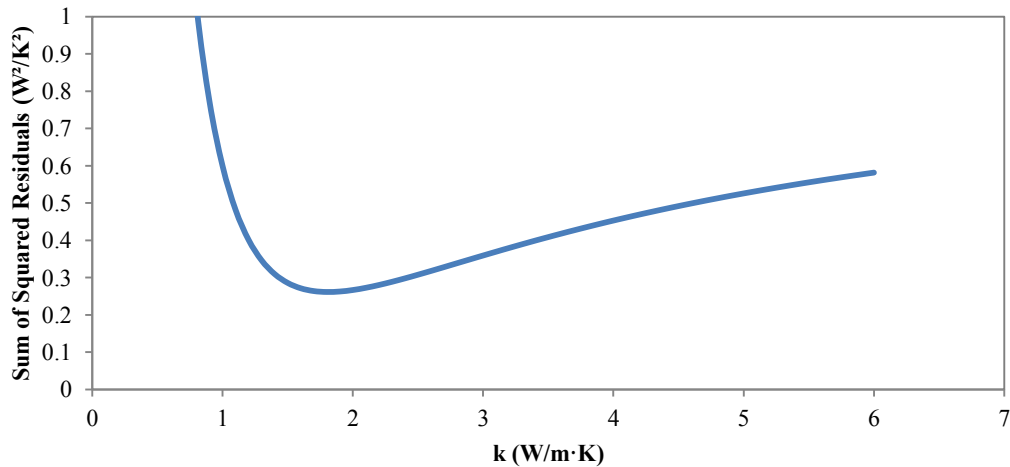


Figure 62 Sum of squared residuals as a function of thermal conductivity

Figure 62 above shows that the best fit is a thermal conductivity of 1.8 W/m·K, i.e., a conductivity of 1.8 W/m·K provides the least amount of error between the analytical/numerical model and the experimental data. Plotting the experimental overall thermal conductance and comparing it to the analytical/numerical predictions shows that the best fit thermal conductivity fits the data nicely in the range of flow rates studied here. Note also that although the experimental results show that the “effective” thermal conductivity is clearly above the lower bound calculated in section 5.4 ($k_{\perp}=0.5$ W/m·K), the sensitivity to thermal conductivity at values above the best fit is reduced significantly as the convective thermal resistance starts to dominate the overall thermal conductance of the WTHX. Thus, increasing the thermal conductivity

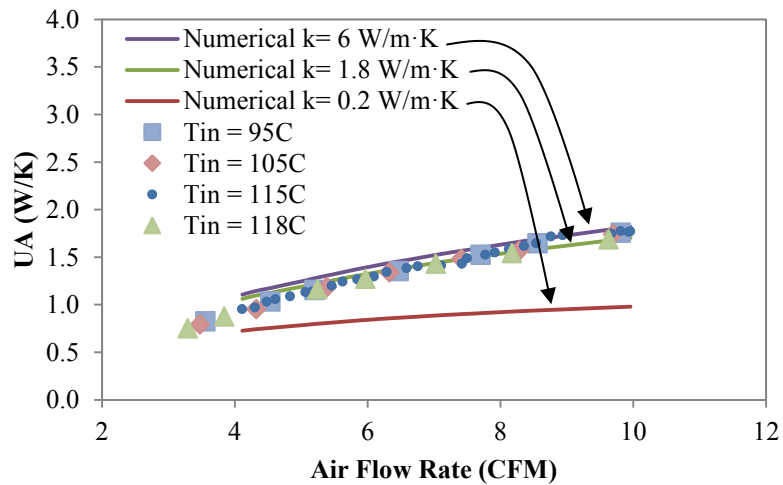


Figure 63 Thermal conductance as a function of mass flow rate

6 Conclusions

6.1 Summary and Contributions

6.1.1 Current State of the Art

In the first chapter of this dissertation, the history of polymer heat exchangers was reviewed as well as current applications. It was noted that corrosive applications are the main user of polymer heat exchangers. Also, the low thermal conductivity is one of the major impediments for the widespread application of polymers.

6.1.2 Benefits of thermally enhanced polymer composites

In Chapter 2, thermally enhanced polymers were introduced. This family of polymers bridges the gap between unfilled polymers and corrosion resistant metals. It was shown that the use of polymers in seawater heat exchangers could potentially bring along significant energy and water savings.

We identified the need for a novel cooling technology that reduces energy use and water demand. It was noted that the implementation of PHXs could offer increased electricity output while alleviating demand for freshwater. A case study of a gas/liquid HX was used to present the potential energy and water savings brought on by the use of polymer heat exchangers for seawater cooling; specifically, heat exchangers made with thermally enhanced polymers. In general, an energy efficient heat exchanger requires a lightweight material with relatively good thermal conductivity and low embodied energy. It was found that the choice of material for each of the applications studied here depends on the relationship between heat transfer rate and thermal conductivity. These results revealed that the use of seawater as a coolant appears to be a viable mechanism to reduce the use of freshwater, as long

as a suitable corrosion-resistant material is used. For a methane cooler, a thermal conductivity over 10 W/m·K brings about diminishing improvements in heat transfer. Therefore, medium-k or high-k composites are needed for the HX to use less energy than the metal HXs. In a liquid to liquid HX, however, it was found that improvements in heat transfer rate can be neglected for thermal conductivities over 5 W/m·K. Considering the relatively higher embodied energy of all metals, and the fact that a high thermal conductivity is not needed, the best suited material was the low-k polymer composite.

6.1.3 Integrated Design Methodology

In Chapter 3 we described the integration of thermo-fluid considerations, moldability issues, and assembly costs into a single design tool for thermally enhanced polymer heat exchangers, constructed from experimentally validated simulations. The moldability analysis metamodel was integrated into our formulation of the overall heat exchanger cost, which is composed of the molding cost and assembly cost (and pumping power cost is life cycle is considered). These cost components are functions of the heat exchanger design variables. The results show that incorporating molding limitations into the molding cost restricts the choice of optimum designs that minimize the cost, and that distinguishing between feasible and infeasible designs directly affects the choice of heat exchanger parameters. Additionally, the optimum heat exchanger geometry is highly dependent on the values of material price and labor costs because they influence which cost components dominate the design space. Currently, the design tool is limited by a single choice of geometry. It would be desirable to have at our disposal a variety of complex heat exchanger geometries,

which would give the designer freedom to explore more than one possible solution. Also, fiber-filled composites usually have anisotropic thermal conductivity, so more detailed thermal models could account for lateral/longitudinal conduction, and hence more precise estimations of thermal performance.

6.1.4 Process-Induced Thermal Anisotropy

The thermal behavior of an injection-molded fin subjected to convective heat transfer was studied. Injection molding simulations of a finned-plate were followed by fiber orientation predictions using the Folgar-Tucker model embedded in Moldflow®, especially suited to the behavior of very thin mold cavities. Based on the predicted orientation tensors, anisotropic thermal conductivity values were calculated using the Nielsen's model. Thermal simulations, using finite-element software, for local anisotropy were then performed to assess the heat transfer rate and temperature distribution of anisotropic Nylon 12 plate fins, with 33% volumetric concentration of carbon fibers.

The results obtained in the numerical simulation of local anisotropy highlight the effect of the relatively low thermal conductivity of the polymer composite, yielding significant through thickness temperature variations and poorer thermal dissipation due to cooler exposed fin surfaces. Moreover, the lateral temperature distribution of the fin appears to be skewed due to the difference in flow-induced orientation (and conductivity) in the fin. Finally, the use of an effective conductivity to represent the anisotropic fin was explored. It was found that using harmonic means either in one-dimensional or two-dimensional models gives very good predictions of the heat transfer rate. For heat transfer coefficients below 300 W/m²K, the relative errors in

the heat transfer rate are below 10%. It was also found that using a 2D model reduces the maximum heat transfer rate relative error when compared to a 1D model prediction. The effect of the process-induced low-k region at the fin base is exacerbated for high-aspect ratio fins. As a result, effective conductivity models fail to capture this behavior, and tend to over-predict the heat transfer rate of high-aspect ratio fins.

6.1.5 Novel polymer composite heat exchanger

Finally, a novel polymer composite heat exchanger, called a webbed-tube heat exchanger was introduced. The design is shown to have similar thermal performance to a plate-fin heat exchanger while using less material volume. The design also takes advantage of the process-induced properties to naturally create a strong, thin-walled tube with good thermal performance. Several prototypes were made using a popular additive manufacturing process called fused deposition model using raw and low-volume fraction composites. These prototypes served both as a proof-of-concept and initial performance verification. For modest water pressures, the prototype proved to be leak proof. An injection-molded webbed tube heat exchanger prototype was also made using a polymer composite. This heat exchanger was used for verifying the expected thermal performance and for extracting an effective heat exchanger thermal conductivity. The effective thermal conductivity was found to be more than three times the predicted lower bound of the thermal conductivity.

7 Appendices

7.1 Thermal conductivity measurement of polymer composite

A disk (12.7 mm diameter) was injection-molded, and the thermal conductivity was measured using the laser flash test. However, Moldflow simulations revealed a flow pattern—extensional flow in the core—that causes the fiber orientation and the conductivity to vary with location. The micro-images, shown in Figure 64, confirm these predictions. More experiments are needed to address this issue.

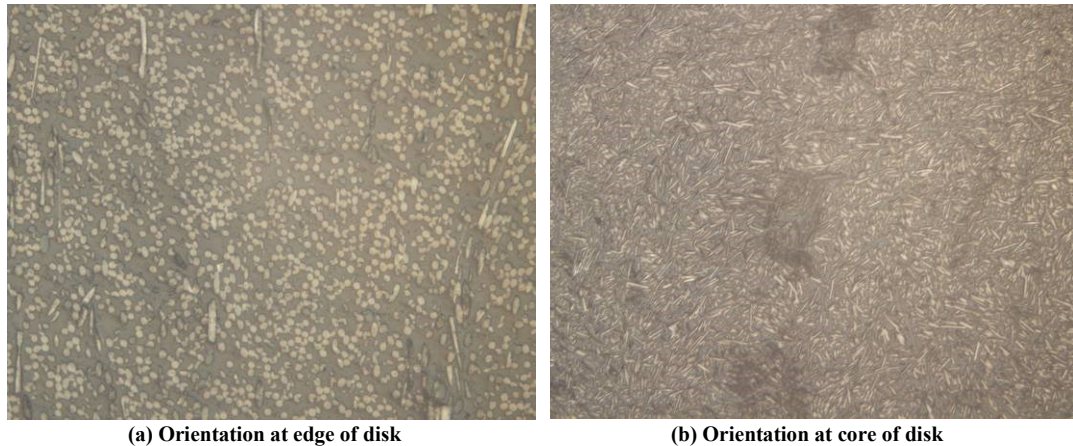


Figure 64 Cross sectional pictures of laser flash test specimen used to measure thermal conductivity.

The resulting conductivity was measured using the laser flash method and the results are shown in Table 17 below:

Table 17 Thermal conductivity measurements using laser flash method for out-of-plane samples

Sample	ρ (g/cm ³)	α (cm ² /s)	C_p (J/Kg.K)	k (W/m.K)
1	1.513	0.02398	1.030	3.737
2	1.500	0.02196	1.100	3.625
3	1.503	0.02404	1.155	4.172

7.2 Experimental validation of Moldflow filling predictions

A spiral aluminum mold was machined using CNC equipment. The cross-section of the spiral is 2.286 mm wide by 1.27 mm tall.

The spiral mold was used to conduct filling experiments using the Babyplast injection machine to create parts with PolyOne's thermally enhanced Nylon 12 (NJ 6000 TC).

The parts were injected at two different pressures: 150 MPa and 180 MPa, with a melt temperature of 270 C. The measured length of the spirals was compared with the length predicted by Moldflow under similar conditions. Figure 9 below shows a plot comparing the experimental results to those predicted by Moldflow. Moldflow predictions are approximately within 20% of the experimental measurements

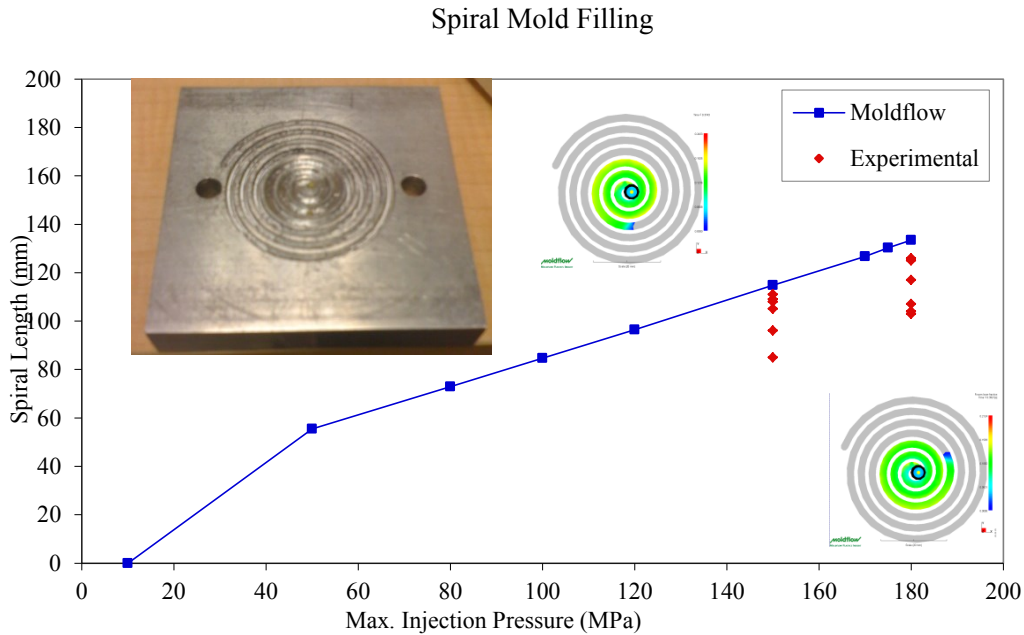


Figure 65 Experimental verification of Moldflow filling predictions

A finned-plate mold was machined (Figure 66a), and full parts were successfully molded with PolyOne's thermally enhanced Nylon 12 (Figure 66b).



(a) Aluminum mold



(b) Molded parts

Figure 66 Fabrication of a molded ABS polymer finned plate.

7.3 Press Release

Contact:
Avram Bar-Cohen
University of Maryland
College Park, Maryland
Phone: 301.405.3173
Fax: 301.314.9477
Email: abc@umd.edu

News Release 3D-Printed Plastic Heat Exchanger

College Park, Nov 23, 2011 – The



Polycarbonate Webbed-Tube Heat Exchanger

University of Maryland, College Park (UMD) and Stratasys, Inc. announce the successful design, fabrication, and test of a Webbed Tube Heat Exchanger (WTHX), the first plastic heat exchanger made by additive manufacturing. Fabricated at the Stratasys facility in Eagan, MN, the 3D-printed WTHX promises to expand the potential applications of polymer heat exchangers to small production volumes and cost constrained systems.

The WTHX represents the first time that a plastic heat exchanger has been manufactured through Stratasys' Fused Deposition Modeling (FDM) technology and used to successfully transfer heat through a polymer structure from a hot gas to a cold liquid. Room air, heated to 120 °C was cooled by building water at 27 °C, transferring nearly 65W of heat in the 500 cm³ heat exchanger.

Juan Cevallos, a PhD candidate and research assistant in the TherPES Laboratory at UMD's Department of Mechanical Engineering, was responsible for testing the WTHX. Under the direction of Professor Avram Bar-Cohen - along with Professors S. K. Gupta, David Bigio, and Hugh Bruck - Cevallos has been working in collaboration with the Petroleum Institute in Abu Dhabi to advance polymer heat exchanger technology for seawater cooling of LNG processes, among other

applications. The relatively high tool and assembly costs of low volume polymer molding production led Bar-Cohen's research team to select an additive manufacturing technology that could build complex geometries in a single step. Stratasys' FDM technology provides that capability while using some of the strongest and most heat-resistant thermoplastics found among additive manufacturing technologies.

The WTHX geometry consists of a stack of rectangular flat plates, each containing an array of tubes that span the length of the plate and are separated by short webs. The tubular array carries the water, while the air flows in the gaps between the rectangular webbed-tube plates. The diameter of the tubes is selected to reduce the power required to pump the liquid while creating a "bumpy" surface on the gas-side that enhances heat transfer between the gas and liquid streams. Moreover, most of the heat transfer occurs directly across the thickness of the WTHX tubes, minimizing the deleterious effect of the low thermal conductivity of the polycarbonate resin.

8 References

- [1] DuPont-News, New Renewably-Sourced Polymer Debuts in Radiator End Tank Program, Jointly Developed with DuPont Engineering Polymers, DENSO
http://www2.dupont.com/Automotive/en_US/news_events/article20090309.html, 9 March 2009, 2009.
- [2] Hewitt, G. F., Shires, G. L., Bott, T. R., *Process heat transfer*, Begell House, Boca Raton, 1994.
- [3] Schweitzer, P. A., *Mechanical and Corrosion-Resistant Properties of Plastics and Elastomers*, Marcel Dekker, New York, 2000.
- [4] Roach, P. D., Holtz, R. E., *Using Plastics in Waste Heat Recovery, Proceedings of the ASME/JSME Thermal Engineering Joint Conference*, Honolulu, Hawaii, vol. 2, pp. 409-412, 1983.
- [5] Yu, T. L., Yu, X. M., Peng, D., Huang, X. G., Liao, J. L., Gong, S. G., Jiang, G. F., Self-Cleaning the Fouling from the Inside Wall of Tubes in a Vertical Water-Cooling Equipment with Plastic Twisted Tapes, *Proceedings of the International Conference on Compact Heat Exchangers and Enhancement Technology for the Process Industries*, Banff, Canada, pp. 503-505, 1999.
- [6] Weitz, F., van der Geld, C. W. M., Ganzevles, F. L. A., Lexmond, A. S., The effect of inserts on heat transfer, drainage and gas cleaning efficiency of plastic exchangers, *Proceedings of the International Conference on Compact Heat Exchangers and Enhancement Technology for the Process Industries*, Banff, Canada, pp. 507-514, 1999.
- [7] Shah, R. K., Sekulic, D. P., *Fundamentals of heat exchanger design*, 1st ed., John Wiley & Sons, Hoboken, NJ, 2003.
- [8] Githens, R. E., Minor, W. R., Tomsic, V. J., Flexible-tube heat exchangers, *Chemical Engineering Progress*, vol. 61, no. 7, pp. 55-62, 1965.
- [9] Pescod, D., Heat Exchanger for Energy Saving in an Air-Conditioning Plant, *ASHRAE Transactions*, vol. 85, no. 2, pp. 238-251, 1979.
- [10] Pescod, D., An Advance in Plate Heat Exchanger Geometry Giving Increased Heat Transfer, in *Compact Heat Exchangers - History, Technological Advancement and Mechanical Design Problems*, eds. R. K. Shah, C. F. McDonald, C. P. Howard, pp. 73-77, American Society of Mechanical Engineers, New York, 1980.
- [11] Pescod, D., Effects of Turbulence Promoters on the Performance of Plate Heat Exchangers, in *Heat Exchangers: Design and Theory Sourcebook*, eds. N. H. Afgan, E. U. Schlünder, pp. 601-615, Scripta Book Company, Washington, D.C., 1974.
- [12] Pescod, D., Unit Air Cooler Using Plastic Heat Exchanger with Evaporative Cooled Plates, *Australian Refrigeration, Air Conditioning and Heating*, vol. 22, no. 9, pp. 22-26, 1968.
- [13] Miller, D., Holtz, R. E., Koopman, R. N., Marciniak, T. J., MacFarlane, D. R., Plastic heat exchangers: a state-of-the-art review, ANL-79-12, 1979.
- [14] Reay, D. A., Use of polymers in heat exchangers, *Heat Recovery Systems and CHP*, vol. 9, no. 3, pp. 206-216, 1989.

- [15] CEA-GRETh, Design of new heat exchanger made of polymer, BES2-3251, 2001.
- [16] Zaheed, L., Jachuck, R. J. J., Review of polymer compact heat exchangers, with special emphasis on a polymer film unit, *Applied Thermal Engineering*, vol. 24, pp. 2323--2358, 2004.
- [17] Liu, W., Davidson, J., Mantell, S., Thermal Analysis of Polymer Heat Exchangers for Solar Water Heating: A Case Study, *Journal of Solar Energy Engineering*, vol. 122, no. 2, pp. 84-91, 2000.
- [18] Raman, R., Mantell, S., Davidson, J., Wu, C., A Review of Polymer Materials for Solar Water Heating Systems, *Journal of Solar Energy Engineering*, vol. 122, no. 2, pp. 92-100, 2000.
- [19] Wu, C., Mantell, S. C., Davidson, J. H., A method for measuring the creep behavior of pressurized polymer tubing, *Experimental Mechanics*, vol. 41, no. 4, pp. 368-374, 2001.
- [20] Li, Z., Davidson, J. H., Mantell, S. C., Heat Transfer Enhancement Using Shaped Polymer Tubes: Fin Analysis, *Journal of Heat Transfer*, vol. 126, no. 2, pp. 211-218, 2004.
- [21] Wu, C., Mantell, S. C., Davidson, J., Polymers for Solar Domestic Hot Water: Long-Term Performance of PB and Nylon 6,6 Tubing in Hot Water, *Journal of Solar Energy Engineering*, vol. 126, no. 1, pp. 581-586, 2004.
- [22] Alizadeh, S., Performance of a solar liquid desiccant air conditioner - An experimental and theoretical approach, *Solar Energy*, vol. 82, no. 6, pp. 563-572, 2008.
- [23] Mannoni, A., Vitali, D., Development of All-Nylon Charge Air Cooler for Automotive Applications, *Vehicle Thermal Management: Heat Exchangers and Climate Control*, Nashville, TN, 2001.
- [24] DuPont-News, Flue gas coolers with AlWaFlon® pressure hoses based on DuPont Teflon® PTFE maximize power plant efficiency, <http://uk.news.dupont.com/site/contenu.asp?idtri=675&idcontenu=57527>, 2009.
- [25] Heat Exchanger Materials - New fluoropolymer technology extends heat exchanger life, *Modern Power Systems*, December 22, 2010.
- [26] Chen, L., Li, Z., Guo, Z.-Y., Experimental investigation of plastic finned-tube heat exchangers, with emphasis on material thermal conductivity, *Experimental Thermal and Fluid Science*, vol. 33, no. 5, pp. 922-928, 2009.
- [27] Renewaire, Energy Recovery Ventilation, <http://www.renewaire.com>, 2010.
- [28] Cevallos, J.G., Bergles, A.E., Bar-Cohen, A., Rodgers, P., Gupta, S.K., Polymer Heat Exchangers - History, Opportunities, and Challenges, *Heat Transfer Engineering*, vol. 33, no. 13, pp. 1075-1093, 2012.
- [29] Cevallos, J.G., Robinson, F., Bar-Cohen, A., Bruck, H., Polymer Heat Exchangers – An Enabling Technology for Water and Energy Savings, *Proceedings of ASME2011 the International Mechanical Engineering Congress & Exposition*, Denver, Colorado, 2011.
- [30] Energy Information Administration, Electric Power Annual 2009, <http://ftp.eia.doe.gov/cneaf/electricity/epa/epa.pdf>, 2011.

- [31] Energy Information Administration, Annual Energy Outlook 2011 with Projections to 2035, [http://www.eia.gov/forecasts/aeo/pdf/0383\(2011\).pdf](http://www.eia.gov/forecasts/aeo/pdf/0383(2011).pdf), 2011
- [32] Fthenakis, V., and Kim H. C., Life-cycle uses of water in U.S. electricity generation, *Renewable and Sustainable Energy Reviews*, vol. 14, pp. 2039-2048, 2010.
- [33] Census Bureau, 2009, Cumulative Estimates of Resident Population Change for the United States, Regions, States, and Puerto Rico and Region and State Rankings: April 1, 2000 to July 1, 2009, <http://www.census.gov/popest/states/tables/NST-EST2009-02.xls>, 2009.
- [34] Kenny, J. F., Barber, N. L., Hutson, S. S., Linsey, K. S., Lovelace, J. K., and Maupin, M. A., Estimated Use of Water in the United States in 2005, *United States Geological Survey*, <http://pubs.usgs.gov/circ/1344/pdf/c1344.pdf>, 2009.
- [35] Department of Energy, Estimating Freshwater Needs to Meet Future Thermoelectric Generation Requirements, http://www.netl.doe.gov/technologies/coalpower/ewr/pubs/2008_Water_Needs_Analysis-Final_10-2-2008.pdf, 2008.
- [36] Department of Energy, Water Requirements for Existing and Emerging Thermoelectric Plant Technologies, <http://www.netl.doe.gov/energy-analyses/pubs/WaterRequirements.pdf>, 2009.
- [37] Carney, B., Feeley, T., and McNemar, A., Department of Energy, National Energy Technology Laboratory, Power Plant-Water R&D Program, <http://www.netl.doe.gov/technologies/coalpower/ewr/water/pdfs/NETL%20Paper%20Unesco%20Conference.pdf>, 2008.
- [38] Tawney, R., Khan, Z., and Zachary, J., Economic and Performance Evaluation of Heat Sink Options in Combined Cycle Applications, *Engineering for Gas Turbines and Power*, vol. 127, pp. 397-403, 2005.
- [39] Najjar, K. F., Shaw, J. J., Adams, E. E., Jirka, G., and Harleman, R. F., An Environmental and Economic Comparison of Cooling System Designs for Steam-Electric Power Plants, Massachusetts Institute of Technology, MIT-EL 79-037, 1979.
- [40] Suzuki, T., and Takahashi, J., Prediction of Energy Intensity of Carbon Fiber Reinforced Plastics for Mass-Produced Passenger Cars, *Ninth Japan International SAMPE Symposium JISSE-9*, Tokyo, Japan, 2005.
- [41] Nielsen, L. E., The Thermal and Electrical Conductivity of Two-Phase Systems, *Industrial & Engineering Chemistry Fundamentals*, vol. 13, no. 1, pp. 17-20, 1974.
- [42] Pugh, S. J., Hewitt, G. F., and Muller-Steinhagen, H., Fouling During the Use of Seawater as Coolant – The Development of a User Guide, *Heat Transfer Engineering*, vol. 26, no. 1, pp. 35-43, 2005.
- [43] Cramer, S. D., and Covino, B. S., eds., ASM Handbook Volume 13b: Corrosion: Materials, Vol. 13, ASM International, Materials Park, OH, 2005.
- [44] Kampe, S. L., Incorporating Green Engineering in Materials Selection and Design, *Proceedings of the 2001 Green Engineering Conference: Sustainable and Environmentally-Conscious Engineering*, Roanoke, VA, 2001.

- [45] Japan Aluminum Association, Summary of Inventory Data, *LCA (Life Cycle Assessment) Committee Report*, 1999.
- [46] Luckow, P., Minimum Energy Design of Seawater Heat Exchangers, Thesis, Digital Repository at the University of Maryland, University of Maryland, College Park, MD, 2009.
- [47] Hall, T., Manufacturability Analysis of Thermally-Enhanced Polymer Composite Heat Exchangers, Thesis, Digital Repository at the University of Maryland, University of Maryland, College Park, MD, 2011.
- [48] Robinson, F., Thermomechanical Behavior of Polymer Composite Heat Exchangers, Thesis, Digital Repository at the University of Maryland, University of Maryland, College Park, MD, 2011.
- [49] T'Joen, C., Park, Y., Wang, Q., Sommers, A., Han, X., Jacobi, A., A review on polymer heat exchangers for HVACR applications, *International Journal of Refrigeration*, vol. 32, no. 5, pp. 763-779, 2009.
- [50] Shah, R., Advances in Science and Technology of Compact Heat Exchangers, *Heat Transfer Engineering*, vol. 27, no. 5, pp. 3-22, 2006.
- [51] Zweben, C., Emerging High-Volume Applications for Advanced Thermally Conductive Materials, *The 49th International SAMPE Symposium and Exhibition Proceedings*, Long Beach, California, 2004.
- [52] Erhard, G., *Designing with plastics*, Hanser Gardner Publications, Cincinnati, 2006.
- [53] Bar-Cohen, A., Rodgers, P., Cevallos, J. G., Application of Thermally Enhanced Thermoplastics to Seawater-Cooled Liquid-Liquid Heat Exchangers, *5th European Thermal-Sciences Conference Proceedings*, Eindhoven, Netherlands, 2008.
- [54] Luckow, P., Bar-Cohen, A., Rodgers, P., Minimum Mass Polymer Seawater Heat Exchanger for LNG Applications, *Journal of Thermal Science and Engineering Applications*, vol. 1, no. 3, 2010.
- [55] Haytoui, N., and Rodgers, P., Survey of Heat Exchanger Usage at ADGAS Das Island LNG Plant, Internal Report for Energy Education and Research Collaboration (EERC) between University of Maryland and The Petroleum Institute, 2008.
- [56] Petukhov, B. S., "Heat Transfer and Friction in Turbulent Pipe Flow with Variable Physical Properties," *Advances in Heat Transfer*, Hartnett, J. P., and Irvine, T. F., (Eds), Vol. 6, Academic Press, New York, 1970.
- [57] Nellis, G. F., and Klein, S. A., *Heat Transfer*, Cambridge University Press, 2009.
- [58] Gnielinski, V., "New Equation for Heat and Mass Transfer in Turbulent Pipe and Channel Flow," *International Journal of Chemical Engineering*, vol. 16, pp. 359-368, 1976.
- [59] Kakac, S., Shah, R. K., and Aung, W., eds., *Handbook of Single-Phase Convection Heat Transfer*, Wiley-Interscience, 1987.
- [60] Cevallos, J.G., Gupta S.K., and Bar-Cohen, A., Incorporating Moldability Considerations during the Design of Polymer Heat Exchangers, *Journal of Mechanical Design*, vol. 133, no.8, 081009 (9 pages), 2011.

- [61] Nihous, G. C., "A Preliminary Assessment of Ocean Thermal Energy Conversion Resources," *Energy Resources Technology*, 129, pp. 10-17, 2007.
- [62] Tester, J. W., Drake, E. M., Driscoll, M. J., Golay, M. W., and Peters, W. A., *Sustainable Energy: Choosing Among Options*, MIT Press, Cambridge, MA, Chap. 14, 2005.
- [63] Energy Information Administration, "International Energy Outlook 2010," <http://www.eia.doe.gov/oiaf/ieo/index.html>, 2010.
- [64] Takahashi, P. and Trenka, A., *Ocean Thermal Energy Conversion*, Wiley, New York, NY, 1996.
- [65] Panchal, C. B., Heat Transfer with Phase Change in Plate-Fin Heat Exchangers, *AIChE Symposium Series*, Vol. 80, No. 236, pp. 90-97, 1984.
- [66] National Renewable Energy Laboratory, "Heat Exchanger for Closed-Cycle Systems," http://www.nrel.gov/otec/electricity_heat_exchangers.html, 2011.
- [67] Osswald, T.A. and J.P. Hernández-Ortiz, *Polymer processing: modeling and simulation*, Munich; Cincinnati: Hanser Publishers. xxvii, 606 p, 2006.
- [68] Boothroyd, G., Dewhurst, P., and Knight, W., *Product Design for Manufacture and Assembly* 2nd ed., M. Dekker, New York, Chap. 8, 2002.
- [69] Bejgerowski, W., Gupta, S. K., and Bruck, H. A., A Systematic Approach for Designing Multifunctional Thermally Conducting Polymer Structures With Embedded Actuators, *ASME Journal of Mechanical Design*, 131(11), p. 111009, 2009.
- [70] Luckow, P., et al., Energy Efficient Polymers for Gas-Liquid Heat Exchangers, *ASME 2nd International Conference on Energy Sustainability*, Jacksonville, FL, USA, 2008.
- [71] Hall, T., Dabbeeru, M. M., and Gupta, S. K., A New Approach for Explicit Construction of Moldability Based Feasibility Boundary for Polymer Heat Exchangers, *Proceedings of ASME 2011 International Design Engineering Technical Conferences & Computers and Information in Engineering Conference*, 2011.
- [72] Rao, N. S., Schumacher, G., *Design Formulas for Plastics Engineers*, Second Edition, Hanser, Cincinnati, 2004.
- [73] Advani, S.G. and C.L.T. III, The Use of Tensors to Describe and Predict Fiber Orientation in Short Fiber Composites, *Journal of Rheology*, vol. 31, no. 8, p. 751-784, 1987.
- [74] Bay, R.S. and C.L. Tucker. Fiber orientation in simple injection moldings. Part 1. Theory and numerical methods, *Polymer Composites*, vol. 13, no. 4, pp. 317-331, 1992.
- [75] Bay, R.S. and C.L. Tucker. Fiber orientation in simple injection moldings. Part 2 - experimental results, *Polymer Composites*, vol. 13, no. 4, pp. 332-341, 1992.
- [76] Folgar, F. and C.L. Tucker III, Orientation Behavior of Fibers in Concentrated Suspensions. *Journal of Reinforced Plastics and Composites*, vol. 3, no. 2, pp. 98-119, 1984.
- [77] Autodesk Moldflow Insight, Available from: <http://usa.autodesk.com/adsk/servlet/index?siteID=123112&id=13195432>, [7 September 2009]

- [78] VerWeyst, B.E., et al., Fiber Orientation in 3-D Injection Molded Features, *International Polymer Processing*, 14, pp. 409-420, 1999.
- [79] Jeffery, G.B., The Motion of Ellipsoidal Particles Immersed in a Viscous Fluid, *Royal Society of London Proceedings Series A*, 102, pp. 161-179, 1922.
- [80] Theoretical Basis for Fiber Orientation Prediction, *Moldflow Help Files*, Moldflow Plastics Insight 6.1.
- [81] Cintra, J.S., Jr. and C.L. Tucker, III, Orthotropic closure approximations for flow-induced fiber orientation, *Journal of Rheology*, vol. 39, no. 6, pp. 1095-1095, 1995.
- [82] X. Lu and G. Xu, Thermally conductive polymer composites for electronic packaging, *Journal of Applied Polymer Science*, vol. 65, no. 13, pp. 2733-2738, 1997.
- [83] C. P. Wong, R.S.B., Thermal conductivity, elastic modulus, and coefficient of thermal expansion of polymer composites filled with ceramic particles for electronic packaging. *Journal of Applied Polymer Science*, vol. 74, no. 14, pp. 3396-3403, 1999.
- [84] Bigg, D.M., Thermally Conductive Polymer Compositions, *Polymer Composites*, vol. 7, no. 3, pp. 125-140, 1986.
- [85] Nielsen, L.E. and R.F. Landel, Mechanical Properties of Polymers and Composites: Second Edition, Revised and Expanded, *Mechanical Engineering*, no. 93, p. 90, 1994.
- [86] Burgers, J.M., *Second Report on Viscosity and Plasticity*, New York, Nordemann, 1938.
- [87] Bar-Cohen, A. and R. Bahadur. Characterization and Modeling of Anisotropic Thermal Conductivity in Polymer Composites, *ASME International Mechanical Engineering Congress and Exposition*, 2006.
- [88] Cytec Thornel® P-100 2K Carbon Fiber Pitch Precursor, *MatWeb Material Property Data*, <http://www.matweb.com/search/DataSheet.aspx?MatGUID=dd21d18e267044a79df3e8d09de9a420>, [20 May 2009].
- [89] Overview of materials for Nylon 12, *MatWeb Material Property Data*, available from: <http://www.matweb.com/search/DataSheet.aspx?MatGUID=0e37a459c4eb452faa9d92659f9a0ccc>, [20 May 2009].
- [90] PolyOne, Therma-Tech NJ-6000 TC Technical Data Sheet, Available from: <http://catalog.ides.com/pdfdatasheet.aspx?I=55275&E=85972>, [22 July 2008].
- [91] Bar-Cohen, A., Luckow, P., Cevallos, J.G., Gupta, S.K., Thermal Anisotropy in Injection Molded Polymer Composite Fins, *Proceedings of the International Heat Transfer Conference*, Washington, DC, 2010.
- [92] Bahadur, R. and A. Bar-Cohen, Orthotropic thermal conductivity effect on cylindrical pin fin heat transfer, *International Journal of Heat and Mass Transfer*, vol. 50, pp. 1155-1162, 2007.
- [93] Abdelaziz, O., Radermacher, R., Modeling heat exchangers under consideration of manufacturing tolerances and uncertain flow distribution, *International Journal of Refrigeration*, vol. 33, pp. 815-828, 2010.

- [94] Advance Manufacturing Lab, *Equipment Gallery*, Available: <http://www.aml.umd.edu/equipment/index.html>, 20 May 2013.
- [95] Gibson, I., Rosen, D. W., Stucker, B., *Additive Manufacturing Technologies*, Springer, New York, 2010.
- [96] Luckow, P., Bar-Cohen, A., Rodgers, P., and Cevallos, J., Energy Efficient Polymers for Gas-Liquid Heat Exchangers, *Journal of Energy Resources Technology*, vol. 132, pp. 1-9, 2010.
- [97] R. K. Shah and M. S. Bhatti, "Laminar convective heat transfer in ducts," in *Handbook of Single-Phase Convective Heat Transfer* S. Kakac, R. K. Shah, and W. Aung, Eds., ed New York: Wiley, 1987.
- [98] R. K. Shah and D. P. Sekulic, *Fundamentals of heat exchanger design*. Hoboken, NJ: John Wiley & Sons, 2003.
- [99] B. S. Petukhov and V. N. Popov, "Theoretical calculation of heat exchange in turbulent flow in tubes of an incompressible fluid with variable physical properties " *High Temp.*, vol. 1, pp. 69-83, 1963.
- [100] M. S. Bhatti and R. K. Shah, "Turbulent and transition convective heat transfer in ducts," in *Handbook of Single-Phase Convective Heat Transfer*, S. Kakac, R. K. Shah, and W. Aung, Eds., ed New York: Wiley, 1987.
- [101] R. K. Shah and A. L. London, "Laminar Flow Forced Convection in Ducts," in *Supplement 1 to Advances in Heat Transfer*, ed New York: Academic Press, 1978.
- [102] P. Wibuswas, *Laminar Flow Heat Transfer in Non-circular Ducts*: University of London, 1966.
- [103] S. Kakaç, R. K. Shah, and W. Aung, *Handbook of single-phase convective heat transfer*: Wiley, 1987.
- [104] G. Nellis and S. Klein, *Heat Transfer*: Cambridge University Press, 2009.
- [105] A. A. Zukauskas, "Convective heat transfer in crossflow," in *Handbook of Single-Phase Convective Heat Transfer*, S. Kakaç, R. K. Shah, and W. Aung, Eds., ed New York: John Wiley & Sons, 1987.
- [106] S. Kakaç and H. Liu, *Heat Exchangers: Selection, Rating, and Thermal Design*: CRC Press, 2002.